A numerical approach for the design of a novel Thermal Management System for the battery packs of Electric Vehicles based on LTO chemistry

Claudio Cilenti

UNIVERSITY OF SALERNO

DEPARTMENT OF INDUSTRIAL ENGINEERING

Ph.D. Course in Industrial Engineering
Curriculum in Mechanical Engineering
XXXVIII Cycle

A numerical approach for the design of a novel Thermal Management System for the battery packs of Electric Vehicles based on LTO chemistry

Supervisors
Prof. Angelo Maiorino
Prof. Ciro Aprea

Ph.D. Candidate
Claudio Cilenti

Scientific Referees
Prof. Carlo Roselli
Prof. Alessandro Mauro

Ph.D. Course Coordinator
Prof. Massimo De Santo

Summary

List of Figures

List of Tables

Abstract

The rapid electrification of the transport sector has highlighted Thermal Management Systems (TMSs) as a critical factor for the safety and performance of Lithium-ion (Li-ion) battery packs. Simple and reliable methods to investigate the thermal behaviours of Li-ion cells are essential for the Electric Vehicles (EVs) industry to predict key issues when designing dedicated cooling systems. Meanwhile, innovative cooling solutions must align with the future directions of major industry players to improve current mature and reliable technologies, bridging the gap between academic research and industrial development. This thesis aims to develop a simplified thermal model to analyse the thermal behaviour of cylindrical Li-ion battery cells, incorporating a dedicated Equivalent Circuit Model (ECM), the Bernardi et al. equation, and empirical correlations for the Nusselt number in natural convection. The model was validated against experimental data, achieving errors within ±5% and RMSE over 95%. The workflow and approach were applied to design an innovative cold plate system composed of horizontal and vertical minichannels for a 40 Ah LTO battery pack used in EVs. Results showed that the proposed technology met the thermal targets for each battery cell, maintaining temperatures between 20 and 30 °C and temperature spans below 5 °C. Additionally, the design kept bulk and volume increases minimal through a compact and lightweight structure, ensuring compatibility with EV applications.

Chapter I
Introduction

One of the greatest challenges of the energy field is the emission of greenhouse gases (GHGs) into the atmosphere. This aspect concerns the electric and thermal energy production for industries and cities, realising a certain sensitivity to the environment in every kind of process and aspect of modern countries. Societies still rely on fossil fuels, such as oil, natural gas, and coal, due to historical dependence, economic growth needs, and energy security. Fossil fuels remain abundant and relatively inexpensive, making them a dominant energy source despite their environmental impacts, such as global warming and air pollution (Martins, Felgueiras and Smitková, 2018; Martins *et al.*, 2019). Another crucial aspect concerns the capability of power plants based on fossil sources of energy to provide dispatchable energy, meaning they can supply power on demand to balance the variability of renewable sources, such as solar and wind (Li and Yang, 2022). Alternatives, such as nuclear-enabled hydrogen, biofuels, and large-scale energy storage, are being explored to provide low-carbon dispatchable energy. However, fossil fuels currently remain dominant due to their established infrastructure and operational flexibility (Forsberg *et al.*, 2021; Forsberg, Dale and Ingersoll, 2024). Thus, the dispatchability of fossil fuels is a key factor in their continued use despite environmental concerns.

Due to the severe impact of fossil fuels on climate change, the implementation of renewable energy sources remains a fundamental target to achieve continuously. In recent years, major economies have displayed significant variation in their fuel mix portfolios. The Paris Agreement shaped these policies by limiting global temperature rise to well below 2°C (preferably to 1.5°C), despite remaining nationally driven and fragmented rather than governed by a single binding treaty at the global level (Kaya and Kaya, 2025). Norway and France rely heavily on renewable and nuclear, resulting in low-carbon grids, while China, India, and the US have substantial shares of coal and natural gas (Tang, Xu and Wang, 2022; D. Sun *et al.*, 2023; Kocsis, T. Kiss and Arpad, 2024). Instead, Brazil's grid is notable for its high share of hydropower, and Spain and Germany have rapidly increased renewables in recent years (Ankathi *et al.*, 2024; Kocsis, T. Kiss and Arpad, 2024).

The fuel mix of countries is used to produce energy across multiple sectors, primarily electricity generation, thermal energy generation, and transport. Electricity production is the largest sector that consumes a diverse fuel mix, including coal, natural gas, renewables (such as wind, solar, and hydro), and nuclear energy, with the mix varying significantly across countries and influencing emissions and health impacts (Cataldi *et al.*, 2024; Pei *et al.*, 2025). Thermal energy production generally depends on natural gas, coal, and increasingly biomass or renewable sources, but its fuel mix is less studied than the electricity's fuel mix (Daroń and Wilk, 2021; Chudy-Laskowska and Pisula, 2022). The transport sector significantly impacts a country's carbon intensity because it primarily relies on petroleum-based fuels. In recent years, significant progress has been made through the integration of biofuels, hydrogen, or synthetic fuels (Colbertaldo, Guandalini and Campanari, 2018), aiming to reduce the emissions of GHGs in the atmosphere. Among these solutions, Electric Vehicles (EVs) represent one of the most promising answers to decarbonise the transport sector. Recent studies comparing EVs and traditional vehicles use Life Cycle Assessment (LCA) to account for GHG emissions related to Lithium-ion (Li-ion) battery packs production. The results show that realising an EV produces higher GHG emissions than a conventional vehicle (Helmers, Dietz and Weiss, 2020). However, this difference is recovered during the lifetime due to the lower emissions related to electricity production compared to traditional fuels (Helmers, Dietz and Weiss, 2020). The emissions break-even point between EVs and conventional vehicles depends on the fuel mix used to produce electric energy. For instance, the break-even point for vehicles charged in Europe lies between a covered distance of 100000 km and 150000 km, while in North America it corresponds between 18000 km and 25000 km (Hawkins *et al.*, 2013; Buberger *et al.*, 2022).

From a commercial standpoint, the EV market is rapidly expanding, becoming a crucial technology of the global energy system to reduce dependence on fossil fuels. The International Energy Agency (IEA) reports in its *Global EV Outlook 2025* (Outlook, 2025) that EVs belong to a mature and developed market, compared to past years when electric mobility represented a niche market. The IEA document highlights the importance of transport electrification, showing interesting studies and forecasts regarding conventional fuel consumption and the market strategies of major countries. According to the results, the global diffusion of electric transport is going to avoid the consumption of 5 million barrels of petrol per day by 2030. Combining these results with the higher efficiency of electric motors and the electric grid compared to Internal Combustion Engines (ICEs), the forecasts predict that the EVs energy demand will be equal to only the 2.5% of the total global energy demand at the end of the decade. From a commercial perspective, sales of EVs show continuous and robust growth. According to the IEA report, 17 million electric cars were sold worldwide, representing a 25% increase over 2023. Among these, 11 million electric cars were produced in China, representing more than half of the sold EVs and reaffirming their role as a major player on the market.

In accordance with recent goals for the transport sector decarbonisation, Europe has set a binding target to ban new ICE vehicle sales by 2035, aiming for full electrification of new passenger cars (European Parliament, 2022). Furthermore, the EU has mandated rapid expansion of charging infrastructure, including the Alternative Fuel Infrastructure Regulation (AFIR), which requires high-speed chargers every 60 km on major transport corridors, aiming to support the expected growth to 10 million charging points (Cui and Zhao, 2024). However, while countries such as Denmark, Luxembourg, and the Netherlands lead the way, many others (including Poland, Greece, and Italy) lag significantly and may struggle to comply by 2035 due to the massive investments (Möring-Martínez, Senzeybek and Jochem, 2024). This is particularly evident in Figure I.1 (Blenkinsop, 2025), representing the percentage of EV sales by country in Europe for the first seven months of 2025.

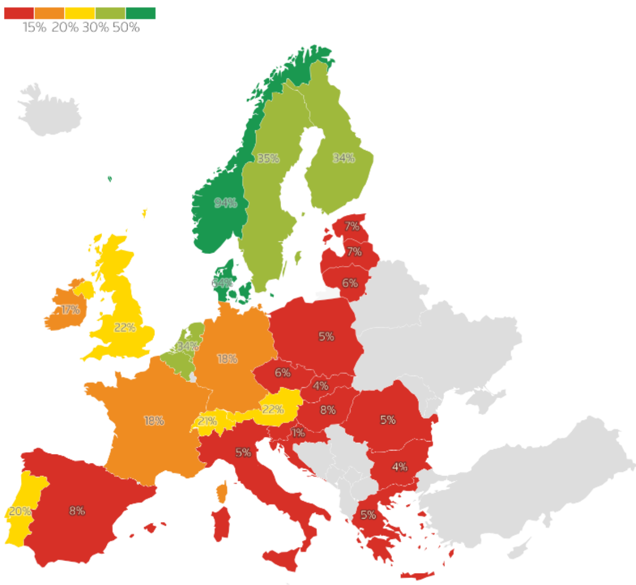

Figure I.1 *Percentage of EV sales by country in Europe for the first seven months of 2025 (Blenkinsop, 2025)*

These choices particularly affected the Western automotive industries, which struggled to compete with Chinese players due to several factors. The crisis has been driven primarily by a global shortage of semiconductor chips, which was exacerbated by the COVID-19 pandemic disrupting supply chains and shifting consumer demand, leading to production halts and long-term supply risks (Shcherbakov, 2022). The Western automotive industry's difficulties are also linked to high production costs, particularly in lithium-ion (Li-ion) battery packs, which are critical for EVs. Despite an 85% reduction in Li-ion battery costs over the past decade, further cost decreases are essential for Electric Vehicles to compete with ICE vehicles, as recent trends show a slowdown and even slight cost increases in 2022 (Orangi *et al.*, 2024). For these reasons, the European Parliament's 2035 target is ambitious, and discussions about potentially relaxing the ban have emerged, partly due to challenges in scaling up EV infrastructure and concerns over the impact of EV battery production (Blenkinsop, 2025).

Investments, research, and development on EVs represent a critical and actual challenge for the automotive industry. This thesis proposes a numerical investigation into the thermal behaviour and management of Li-ion batteries, which represent two of the major issues when designing an EV powertrain. Despite Lithium-ion batteries having become the dominant technology in the electric transport industry due to their great features, such as excellent storage capabilities and memory-free recharge characteristics (Maiorino *et al.*, 2024), their efficiency and safety depend directly on dangerous phenomena that destabilise the inner structure and lead to degradation until total failure (Shahid and Agelin-Chaab, 2022). One of the most hazardous risks concerns abusive conditions such as overcharging, high temperatures, and mechanical force that release flammable gases, causing major explosions and fires (Hu *et al.*, 2024). Degradation of Li-ion batteries, instead, relies on a proper management of the battery pack over the EV's useful life. A limited degradation reduces the risk of more frequent substitution of Li-ion packs, contributing in part to resolving the major issues of Western EV industries in purchasing semiconductors and expensive batteries from other countries.

Affordable, reliable, and simple solutions represent the key to bringing affordable electric vehicles. As the literature has shown in recent years, there is a critical gap between laboratory prototypes and the technologies implemented on commercial EVs by transport industries. Studies proposed on simplified battery packs, expensive techniques, and levels of readiness too low for the market are the principal causes of this disparity. The results of his thesis aim to contribute to the EV research and development by proposing simple approaches based on reliable experimental correlations coupled with Finite Element Modelling (FEM). The scope of the thesis has not been to propose radical changes that would inevitably increase that gap, but to integrate innovative techniques and ideas into the consolidated industry knowledge that engineers and technicians can easily implement in their future projects. The research relies on two innovative approaches concerning the thermal behaviour of Li-ion batteries in natural convection and the development of an innovative cooling system for a commercial battery pack typically used in EVs.

The investigation of Li-ion batteries' thermal behaviour represents an initial and necessary step to understand the causes of the internal generation and why a Thermal Management System (TMS) is required. As shown by articles published in the literature, thermal analysis of Li-ion batteries predicts the average temperature increment over time, the temperature field distribution within a single cell volume, depending on operating conditions and internal features. There are three main methods for studying the thermal behaviour of a Li-ion battery (Madani, Ziebert and Marzband, 2023; Jie Liu *et al.*, 2024):

1. *Experimental method*: The procedure uses precise experimental setups, such as battery calorimeters, to accurately determine heat generation and thermocouples or RTD sensors to measure the surface temperature of a cell. The FEM thermo-fluid dynamic simulations implement the heat generation measurements as inputs for an in-depth analysis.
2. *Equivalent Circuit Models (ECMs)*: This approach evaluates the electrical behaviour of battery cells using an equivalent electric circuit formed by resistors and capacitors. This result is generally coupled with the Bernardi et al. equation (Bernardi, Pawlikowski and Newman, 1985) for estimating the total internal heat generation rate. Electric parameters are obtained through an experimental characterisation called Hybrid Pulse Power Characterisation (HPPC) (Zhang *et al.*, 2018).
3. *Physics-based electrochemical-thermal modelling*: these models provide the thermal behaviour of Li-ion battery cells by implementing the characteristic laws of electrochemical processes and transport phenomena during charge and discharge. The most interesting feature about these models is their independence from experimental characterisations and a pure numerical approach (He *et al.*, 2021).

Despite the experimental method being the simplest procedure from a mathematical standpoint, it poses significant practical challenges. It requires meticulous cell mapping and precise measurement of the heat generated under charging and discharging conditions. Its characterisation is specific to a single battery and lacks general applicability to other devices. The electrochemical model is the most complex and complete one. By applying the equations of electrochemistry, it is possible to estimate the voltage drops caused by ohmic and polarisation losses using the laws of electric potential at the electrodes (Li, Zhou and Wu, 2019), ion transport phenomena (Jie Liu *et al.*, 2024), and polarisation losses (P. Luo *et al.*, 2022). These voltage drops are implemented in the heat generation equation, which is more detailed than the Bernardi et al. equation (Bernardi, Pawlikowski and

Newman, 1985). Although the electrochemical laws are extremely detailed, their complexity does not allow for easy application. Indeed, there are no examples in the literature of industry applications for prototypes. In some cases, the level of detail proposed may even be superfluous. Among these studies, the model presented by Li et al. (Li, Zhou and Wu, 2019) considers the electrical potential distribution on the electrodes of a pouch Li-ion cell. However, the results show that this quantity exhibits a maximum variation of a few tenths of a volt between individual points. The semi-empirical model relies on an equivalent circuit of batteries formed by several devices (such as resistors, capacitors, and generators) (Jie Liu *et al.*, 2024). It is a semi-empirical model because there are no pure numerical techniques for estimating the circuit parameters, especially considering that they strongly depend on the State of Charge (SOC) (Zhang *et al.*, 2018). These pulsating tests must be done in a controlled temperature chamber at different environmental conditions for different SOCs. This thesis demonstrates the effectiveness of ECMs when coupled with simple empirical correlations to study the average temperature trend and the internal temperature field through an experimental validation conducted on a 18650 LTO cell during two typical discharging current profiles at 1C in natural convection. The results were experimentally validated, achieving percentage errors between numerical results and temperature measurements between ±5%. The accurate choice of representative physical parameters of LTO cells (such as thermal conductivity, heat capacity, and density) demonstrates that this model can be used as a tool for industries to characterise their Li-ion battery cells before implementing them into an EV powertrain.

The direct consequence of the previous numerical model relies on the development of an innovative cold plate for a commercial battery pack already employed in EVs. The solution was obtained through a progressive evolution of a commercially available cold plate for liquid-based cooling systems, featuring vertical heat sinks and minichannel architecture. Tailored for integration into commercial battery systems within the automotive and railway sectors, the design prioritises a synergistic balance between superior thermal performance and volumetric efficiency. The research methodology follows two primary pillars:

1. *Iterative design evolution*: Starting from conventional commercial benchmarks, the cold plate underwent a progressive refinement process. Each iteration targeted specific thermal bottlenecks to minimise temperature gradients across the cells and ensure the optimal average temperature of the battery pack.
2. *Analytical sizing and numerical validation*: Each design phase employed a dual-stage approach. Initial channel sizing was derived from empirical correlations and simplified analytical models to meet target specifications. Subsequently, these preliminary results were

validated by employing FEM simulations, refining underlying assumptions, and calibrating the final geometry in case of discrepancies.

The following chapters are organized as follows. Chapter II reports a comprehensive and detailed overview of Li-ion battery technologies, describing their principal features (such as typical geometries and chemistries). This section initially presents all the parameters and information about Li-ion batteries that will be used in the modelling and design sections. In the second paragraph, the dissertation discusses the key features of Thermal Management Systems (TMSs) for battery packs, defining their classification into active and passive systems and distinguishing them based on the coolant used, such as air, liquid, or refrigerants. Although the thesis emphasises cooling, the State of the Art also addresses major issues related to temperature management of battery packs in hot and cold climates, highlighting innovative solutions for both cooling and heating, including internal heating strategies. The final paragraph reviews the current state of TMSs, referencing the latest technological developments in the industrial automotive and railway sectors. The concluding part of the State of the Art aims to identify the gap between academic research and industry leaders in EVs, demonstrating how bridging solutions are crucial for the commercial advancement of these systems. Lastly, future projections are included to illustrate potential directions that industries may pursue.

Chapter III proposed a detailed description of the proposed simplified thermal model for industry. The scope of the chapter is to report the main features and understand how the physical parameters of Li-ion battery cells affect their thermal behaviour. After a brief description of the 18650 LTO cylindrical cell, a further illustration of the model steps and features is presented to investigate possible simplifications and hypotheses applicable in EV case studies. The research comprehensively analyses three different empirical correlations concerning the convective heat transfer coefficient in natural convection for a horizontal cylinder, illustrating how the results change depending on their choice. An experimental validation was performed for all empirical correlations using a thermal camera (accuracy ±1.5 °C). According to the results, the percentage errors between numerical outcomes and measurements achieved values between ±5%. A successive CFD analysis demonstrated which correlation suits best according to the input charge and discharge current profile. The scope was to define a traced path for further investigation of LTO cylindrical cells, widely applied to EV battery packs.

Chapter IV presents the direct applications of the simplified thermal model by designing the innovative cold plate system for the commercially available Toshiba Type3-20 battery pack. The characterisation of the thermal load (corresponding to the nominal cooling capacity of the TMS) was performed, including all the inward heat flux caused by combined mechanisms of heat transfer, such as conduction, convection, and radiation. The inward contributions were applied to the boundary conditions by investigating the working conditions of the high-power battery packs employed in EVs. External conditions, such as the safety enclosure temperature, were applied according to international standards (IEC 62660-1:2010) regarding Li-ion battery tests in a critical hot environment under ordinary working conditions. The inward contributions were estimated based on the effective battery pack temperature field by applying simple and reliable thermal models founded on empirical correlations and mature studies well known in the literature. The design process highlights the criticalities of each technology step by step, proposing progressive solutions to the problems, until the final optimised cold plate system is reached. The innovation relies on the implementation of embedded minichannels, which have been properly sized to guarantee correct thermal management of the entire battery pack in vertical and horizontal directions. The sizing process found a trade-off among bulk and volume occupation, thermal efficiency, and optimal coolant velocity, avoiding stagnation of air bubbles in the circuit. The proposed cold plate system demonstrates optimal thermal management for commercially available battery packs suitable for most electric transport due to its efficiency and limited impact on overall weight and bulk.

Chapter II
State of the Art

II.1 Fundamentals of battery packs for Electric Vehicles

II.1.1 Applications for Electric Vehicles and fundamental parameters

Li-ion batteries are devices capable of converting chemical energy stored in their active materials into electric energy directly through oxidation and reduction reactions (Ogura and Kolhe, 2017). The architectural design of modern batteries follows a hierarchical structure to ensure scalability and safety. Three elements define this structure (Linden and Reddy, 2002; Ogura and Kolhe, 2017):

1. *Cell*: The cell is the basic electrochemical unit providing a source of electrical energy by direct conversion of chemical energy. It consists of an assembly of electrodes, separators, electrolytes, a container, and terminals.
2. *Module*: A module consists of several cells connected in either series or parallel.
3. *Pack*: A battery pack is a set of modules connected in series or parallel to each other.

Batteries are generally classified into two main categories, depending on whether they can be recharged multiple times or are disposable. *Primary batteries* are devices that store electrochemical energy for immediate use but are not rechargeable after the first application. Their life ends when all the stored energy is converted into electricity and wasted heat. Instead, *secondary batteries* (or *rechargeable batteries*) can be reused as electric energy storage by connecting to a power source or the grid. The electric energy is transformed into chemical energy that can be successively converted into electricity available for any electric load.

Rechargeable batteries are used in EVs to store and draw energy from the grid, mainly converting it into kinetic energy via an electric motor while throttling. During this process, the cell anodes undergo oxidation and become positively charged. The electrons released by the chemical reaction are attracted to the cathode, but they cannot pass through the electrolyte, which only allows ions to move between electrodes. Therefore, the electrons are directed through the circuit, powering the electric load. This flow creates a current for energy conversion. When the electrons reach the cathode, reduction occurs, and the electrode becomes negatively charged. This cycle continues until all the chemical energy stored in the battery is converted to electrical energy, with some energy lost as heat due to electrochemical and electrical inefficiencies.

During braking, the electric motor switches to generator mode, reversing torque and converting the EV's kinetic energy into electric energy via electromagnetic induction (Naseem and Seok, 2025; Szumska, 2025). Power electronics and the Battery Management System (BMS) regulate this current and store it in the Li-ion battery pack (Erhan and Özdemir, 2021). This process is called *regenerative braking* and is controlled by the Kinetic Energy Recovery System (KERS). During regenerative braking, the electrons stored in the cathodes return to the other electrode. This happens because the generator induces oxidation reactions within the cathode, which switches function and becomes an anode. Meanwhile, the other electrode accepts electrons through a reduction reaction and becomes the cathode. The battery pack charging stops when the braking phase ends. If the EV is connected to the grid, charging ends when the chemical energy stored in the cells reaches its maximum limit, defined by the battery pack capacity. Figure II.1 schematises the electron and ion flow of a single battery cell during the throttle and regenerative braking phases.

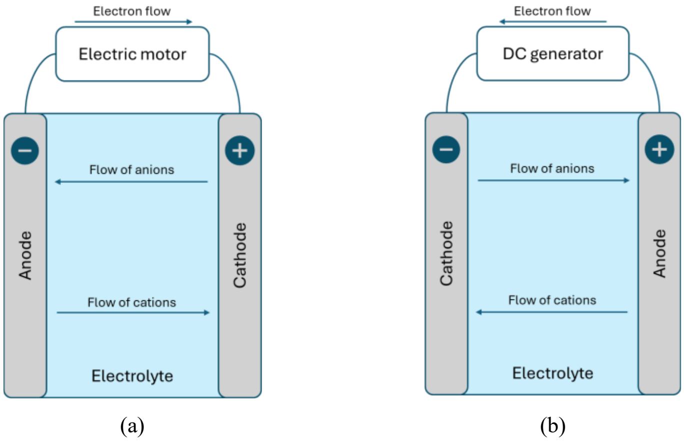

Figure II.1 *Electron and ion flow during throttle (a) and regenerative breaking (b) within the battery cell of an EV*

Therefore, battery packs in Electric Vehicles (EVs) undergo continuous charge and discharge cycles, dictated by the vehicle's power demands and the recovery of energy. Their electrical behaviour is characterised by several key parameters that define energy storage capacity, voltage dynamics, and charging and discharging rates. According to the battery pack datasheet (Ogura and Kolhe, 2017), the following nominal parameters are typically reported:

1. *Nominal Capacity (C_{nom})*: This represents the maximum charge (in Ampere-hours) the battery pack can store under nominal conditions. This value is subject to reduction over time due to degradation phenomena, including calendar aging (Torregrosa *et al.*, 2024), cycling aging (Nájera *et al.*, 2023), and thermal or mechanical abuse (Ouyang *et al.*, 2022).
2. *Nominal Voltage (V_{nom})*: The reference voltage between the battery pack terminals under standard operating conditions.
3. *Cut-off Voltage ($V_{cut\text{-}off}$)*: The minimum allowable voltage level, defining the empty state of the battery and serving as a safety threshold to prevent over-discharge.

While nominal parameters are intrinsic characteristics, the following variables fluctuate dynamically based on the operating conditions (Ogura and Kolhe, 2017):

1. *Terminal Voltage (V)*: The potential difference measured across the terminals during operation. Unlike the nominal voltage, the terminal voltage varies significantly in dynamic conditions due to internal resistance and polarization effects.
2. *State of Charge (SOC)*: A dimensionless ratio between the residual capacity and the nominal capacity. It quantifies the remaining energy available before the battery is fully discharged, typically ranging from 0 (empty) to 1 (fully charged).
3. *C-rate* (C_{rate}): Defined as the ratio of the current intensity to the nominal capacity. It represents the inverse of the time required to charge or discharge the battery pack. For instance, a 1C rate indicates a full discharge in one hour (Linden and Reddy, 2002).

The single cell's open circuit voltage E_{oc} differs from the terminal voltage V due to irreversible phenomena, which manifest as voltage drops. These phenomena are called *polarisation losses* and are divided as follows:

1. *Activation loss*: Concerning the activation energy necessary to drive the electrochemical reaction to the electrode's surface (Linden and Reddy, 2002).
2. *Concentration loss*: Related to the speed of the electrochemical reaction at the electrodes. When the current intensity increases, the redox reactions become faster, reducing the concentration of available reagents.
3. *Ohmic loss*: Caused by the electric resistance of electrodes and terminals. The corresponding voltage drop is calculated through the first Ohm's law, multiplying the current intensity by the equivalent ohmic resistance of the cell R_0.

The terminal voltage expression depends on the open circuit voltage and is represented as Formula II.1 (Linden and Reddy, 2002).

$$V = E_{oc} - (\eta_{act} + \eta_{con} + |I|R_0) \tag{II.1}$$

The terms η_{act} and η_{con} indicate the voltage drops caused by the activation and the concentration losses, respectively. Formula II.1 strictly depends on the current intensity. The difference between the open circuit voltage and the terminal voltage increases proportionally to the current, as shown in Figure II.2.

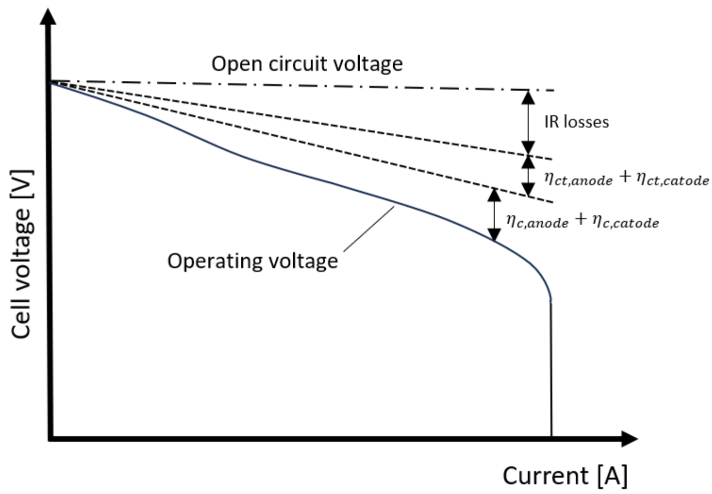

Figure II.2 *Difference between the cell's open circuit voltage and terminal voltage caused by polarisation losses (Linden and Reddy, 2002)*

This curve is called the *polarization curve*. It describes how the terminal voltage of a cell depends on the charge or discharge current.

II.1.2 Battery cell geometries and chemistries

Various geometries and chemistries characterise Li-ion battery cells, and their choice depends on which typology best suits the application of interest. Regarding the geometry, there are three principal typologies:

1. *Cylindrical cells*: They feature a rolled design, which can lead to uneven stress and heat distribution (Baazouzi *et al.*, 2023).
2. *Prismatic cells*: The prismatic cells have a rectangular shape that allows efficient space utilisation and moderate mechanical stability (Awan *et al.*, 2025).
3. *Pouch cells*: They use flexible foil packaging, resulting in lighter weight, better electrochemical performance, and superior vibration resistance. However, they may require careful mechanical support due to their flexible structure (Trinuruk *et al.*, 2023).

Manufacturing costs and recycling processes vary by geometry, with pouch cells generally requiring less energy for crushing during the recycling process. Cylindrical and prismatic cells differ in casing materials and mechanical processing needs (Soldan Cattani *et al.*, 2024). Overall, pouch cells often offer advantages in electrochemical performance and mechanical resilience, cylindrical cells are popular for their robust design and manufacturing maturity, and prismatic cells balance space efficiency and performance (Kim, Choi and Lee, 2019). Figure II.3 schematically represents a cylindrical, a prismatic, and a pouch cell.

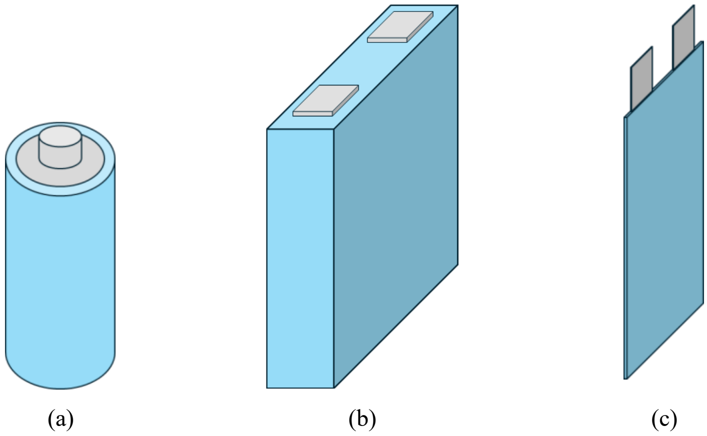

Figure II.3 *Schematic representation of a cylindrical (a), prismatic (b), and pouch (c) cell*

The materials of the electrodes and electrolyte also distinguish several groups of Li-ion batteries. Indeed, the term "Li-ion" indicates a set of several different chemistries that offer various combinations of cost, durability, performance, and safety (Ogura and Kolhe, 2017). There are six typologies of Li-ion batteries:

1. *Lithium Cobalt Oxide (LCO)*: It is the most common type of chemistry for Li-ion batteries in small consumer electronics. An LCO cell consists of a cobalt oxide cathode and a graphite anode. Despite being chosen for its high specific energy, drawbacks include a short life, low thermal stability, and limited load capabilities.
2. *Lithium Manganese Oxide (LMO)*: This type of Li-ion cell is formed by a three-dimensional spinel structure of the cathode made in $LiMn_2O_4$. This feature provides low internal resistance, high thermal stability, and enhanced safety. However, it has limited cycles and calendar life but still holds 50% more energy than a nickel-based chemistry at the same age.
3. *Lithium Nickel Manganese Cobalt Oxide (NMC)*: This chemistry represents the most modern manganese-based Li-ion cell with a cathode combination of nickel, manganese, and cobalt ($LiNiMnCoO_2$). The unique blend provides higher specific energy, prolongs the useful life, and lowers raw material costs, reducing cobalt content. NMC cells are the preferred candidates for electric powertrains.
4. *Lithium Iron Phosphate (LFP)*: LFP cells offer acceptable electrochemical performance with low internal resistance. When a high terminal voltage is guaranteed for a prolonged period, the cathode material ($LiFePO_4$) produces Li-ion batteries capable of full

charge conditions and less working stress than other chemistries. However, LFP cells also have moderate specific energy and lower nominal voltages, despite having excellent safety and a long life.

5. *Lithium Nickel Cobalt Aluminium Oxide (NCA)*: This battery cell shares similar behaviours with NMCs, concerning high specific energy and reasonable specific power. The $LiNiCoAlO_2$ cathode provides a long useful life, making this chemistry an ideal candidate for EVs. However, the principal disadvantage lies in high costs and marginal safety.
6. *Lithium Titanate Oxide (LTO)*: The lithium titanate oxide ($Li_4Ti_5O_{12}$) replaces the graphite in the above-mentioned Li-ion batteries. This chemistry is considered a promising anode material for applications that require high current rates and long useful life. Due to the low nominal cell voltage, they can be fast-charged and deliver a high discharge current. LTO cathodes improve performance and safety in cold climates compared to graphite-based batteries. However, low energy density and high costs are the main drawbacks.

As illustrated by Ogura et al. (Ogura and Kolhe, 2017), main advantages and issues concerning the Li-ion battery chemistries are reported in Figure II.4

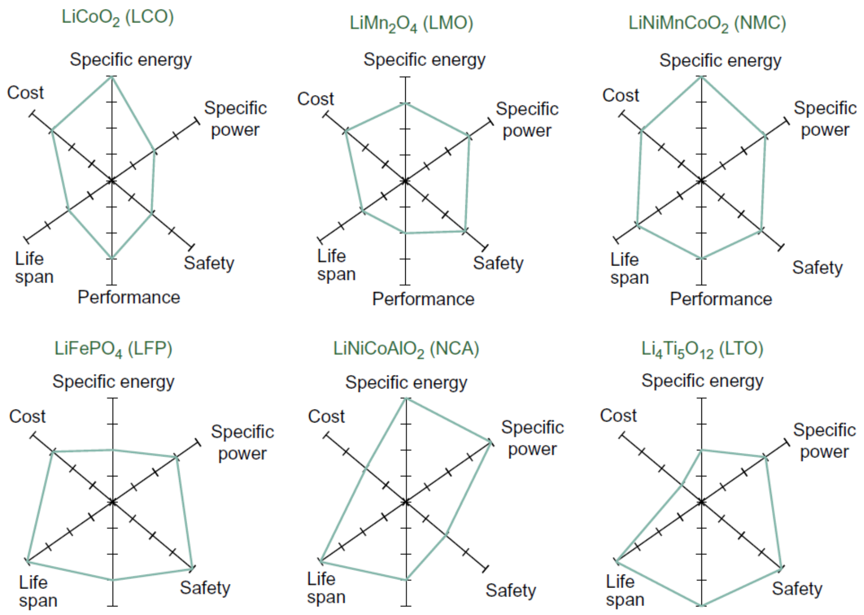

Figure II.4 *Principal advantages and issues of Li-ion battery cells chemistries as reported by Ogura et al. (Ogura and Kolhe, 2017)*

II.1.3 Typical discharging and charging methods of Li-ion batteries

The safety, durability, and performance of batteries are also highly dependent on how they are discharged or charged. As reported in the literature, there are three typical discharging modes of battery packs (Linden and Reddy, 2002):

1. *Constant resistance*: The battery is connected to an electric load characterised by constant resistance over time. As described by the polarisation curve, the terminal voltage and the corresponding discharge current decrease until the battery pack is out of power.
2. *Constant current*: Instead of the previous case, the load's electric resistance varies and changes the terminal voltage. The discharge current remains constant due to the inverse proportionality of electric resistance and voltage.
3. *Constant power*: The power required by the electric load remains constant while the discharging current and terminal voltage change inversely proportionally.

Terminal voltage changes over time for every discharging mode. This characteristic is caused by the voltage drops caused by polarisation losses that depend on the current intensity *I* and the *SOC*. The discharge curve for a constant current discharge is reported in Figure II.5 (Linden and Reddy, 2002). It represents how the terminal voltage changes over time during a constant current discharge.

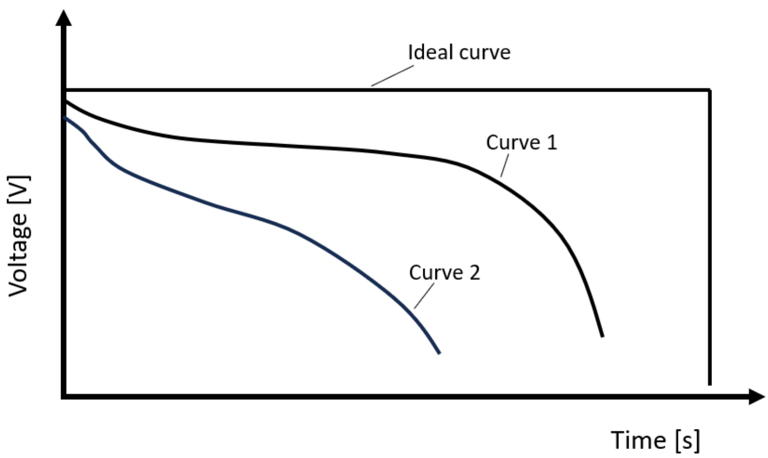

Figure II.5 *Typical discharge curve of a Li-ion battery pack*

While *Curve 1* and *Curve 2* follow a decreasing trend, the ideal curve represents a constant terminal voltage discharge, which drops to 0 when the discharge is over. The terminal voltage in ideal conditions corresponds to the open circuit voltage E_{oc} (Linden and Reddy, 2002). Instead, *Curve 1* and *Curve 2* differ due to the different electric load. In the first case, the load requires more electric power than in the second case. This behaviour is demonstrated by the time of discharge, which is certainly related to a higher constant C_{rate} compared to the first discharge.

Similar to the discharging conditions, Li-ion batteries are generally charged following two typical methods (Ogura and Kolhe, 2017):

1. *Constant voltage*: This method represents the simplest charging procedure. It consists of continuously decreasing the current intensity over time as the electric charge within the Li-ion battery progressively fills. However, it requires high power in the early stage of charging.
2. *Constant current*: The terminal voltage varies according to a control unit, keeping a constant current over time. Generally, the control unit regulates the voltage by estimating how the voltage rises over time in accordance with the polarisation curve.

Figure II.6 is a typical charging of a Li-ion battery pack cell of an electric vehicle. The continuous line indicates the battery pack terminal voltage, while the dashed line reports the discharge current trend over time.

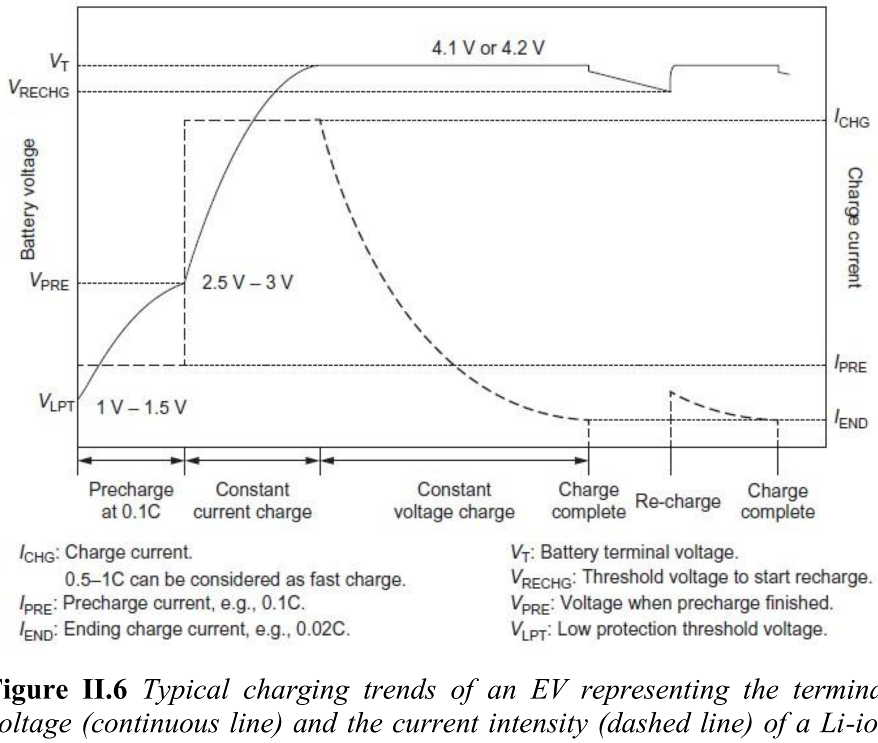

Figure II.6 *Typical charging trends of an EV representing the terminal voltage (continuous line) and the current intensity (dashed line) of a Li-ion cell of an EV (Ogura and Kolhe, 2017)*

The first line represents a pre-charge at 0.1C. When a pack is first connected to power electronics or a load, the Li-ion cells of a battery pack are generally pre-charged at low current, because large capacitors and low impedance can cause a huge inrush current. A pre-charge circuit briefly connects the pack through a resistor so voltage rises gradually, limiting current spikes that can damage cells, inverters, and control circuits, and triggering failures or fires (Ria and Dini, 2024). Successively, the battery cell is charged through the constant current method, generally at 0.5C or 1C (Ogura and Kolhe, 2017). When the terminal voltage reaches a specific upper limit (in this case, 4.1 V), the charge continues using the constant voltage method. Coherently with the typical trend of the polarisation curve, the charging current decreases over time. The process ends when the battery cell is full. Figure II.6 also represents a recharging section, corresponding to regenerative braking (Ogura and Kolhe, 2017). The terminal voltage first decreases due to the release of electricity from the battery pack directed to the electric motor, rapidly restoring to the upper limit through the KERS. These processes define the discharge and charge curve of EVs during ordinary working conditions over time.

II.2 Thermal management of Li-ion batteries: classification and latest technologies

From an energetic standpoint, polarization and other irreversible processes convert part of the chemical energy stored in the battery pack into wasted heat, reducing usable electrical energy and accelerating degradation (J. Guo *et al.*, 2023). Then, the heat generation inside the Li-ion battery pack increases the average temperature during ordinary working conditions. For this reason, Thermal Management Systems (TMSs) of Li-ion battery packs have a key role in preventing several conditions that can affect the safety, performance, and degradation over time. Ordinary and unordinary circumstances uncontrollably raise the average temperature of the battery pack, causing abnormal chemical changes, such as electrolyte decomposition or reactions between the electrodes and the electrolyte. As reported by Ogura and Kolhe (Ogura and Kolhe, 2017), a 20 Ah Li-ion battery subjected to several discharging and charging phases can increase its average temperature to 55 °C under ordinary conditions. Figure II.7 presents the temperature trend over time when the battery pack is discharged at 1C, 2C, and 3C rates, respectively. These values correspond to discharge currents of 20 A, 40 A, and 60 A, and discharging times of 1 hour, 30 minutes, and 20 minutes.

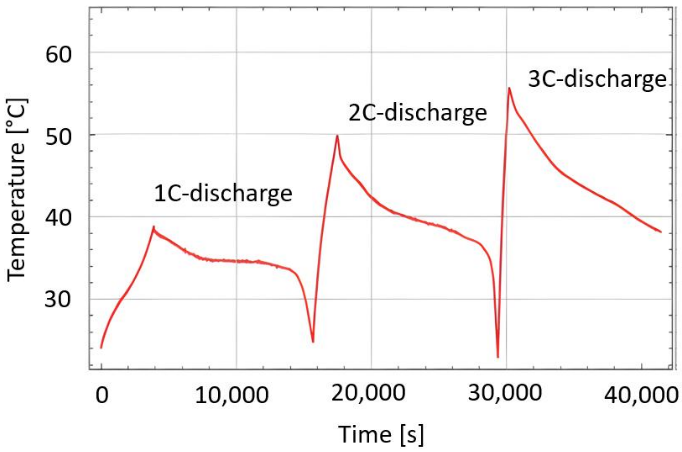

Figure II.7 *Average temperature trend of a 20 Ah Li-ion battery pack subjected to successively 1C, 2C, and 3C discharges over time (Ogura and Kolhe, 2017)*

Instead, an uncontrolled temperature rise can be triggered during abnormal working conditions by a phenomenon called *thermal runaway*. Thermal runaway occurs when exothermic chain reactions inside the battery cause the internal structure to destabilize and degrade, ultimately leading to the complete failure of the device (Shahid and Agelin-Chaab, 2022). This phenomenon occurs due to several forms of mechanical, electrical, or thermal abuse, which causes a short circuit between the electrodes of the battery cell because of electrolyte failure. The heat generated impacts nearby cells, which are also affected. This chain reaction not only raises the battery pack's temperature but also releases many flammable gases, increasing the internal pressure of the pack and potentially causing explosions and fires in the EV powertrain (Shahid and Agelin-Chaab, 2022). According to Peiyi Sun et al. (Sun *et al.*, 2020), more than fifteen fire incidents involving various electric cars occurred in 2018 due to thermal runaway, making it a critical safety concern for EVs. The causes of these explosions happen under different situations, such as driving, charging, or parking. In some cases, the fire was triggered after a collision, which compromised the mechanical integrity of the battery pack and led to the explosion of the powertrain. Thermal runaway can also pose a danger during natural disasters, such as floods, making EVs unusable for safety reasons. A recent example is the flood that struck the Italian region of Emilia Romagna in May 2023. The flooded streets led Ravenna to impose a lockdown on EVs for fifteen days to prevent major fires and blasts caused by safety hazards (Regione Emilia-Romagna, 2023).

While an uncontrolled rise in the battery pack's average temperature affects performance, a rapid temperature decrease reduces electrolyte conductivity and lithium diffusion, increasing the electric and electrochemical losses. This is a critical challenge for those Countries in which the ambient temperature in winter often decreases below 0°C (such as China, Europe, and the United States). These difficulties are aggravated below −20°C, in which the power sourcing capabilities are null (Hu *et al.*, 2020a). The heating phase of a TMS is more demanding compared to cooling because there could be environmental conditions in which the battery pack cannot release electric energy to activate the warming-up system (Zhao *et al.*, 2023). However, this phase is essential to prevent phenomena responsible for performance decay, such as *lithium plating*. Lithium plating is the deposition of metallic lithium on the anode surface made by the graphite surface under fast charging or low-temperature conditions. It reduces the battery life and the capability to store and release energy during the charging and discharging cycle. Nowadays, the mechanism of formation is not fully detected (X. Lin *et al.*, 2021).

In recent years, several optimal temperature ranges have been proposed to achieve the highest efficiency of Li-ion battery packs, preventing thermal runaway and decay of performance over time. While the acceptable temperature region of Li-ion batteries is defined between −20 °C and 60 °C (Ji, Zhang and Wang, 2013), Pesaran et al. (Pesaran, Santhanagopalan and Kim, 2013) reported that Li-ion batteries achieve the peak of efficiency between 15 °C and 35 °C, limiting degradation and formation of dangerous hot spots (L. Xu *et al.*, 2024; Pilali *et al.*, 2025). In some research, a broader high-performance window defined within 20 °C and 40 °C is often cited (K. Li *et al.*, 2024). Regarding the temperature field uniformity, the maximum allowable temperature difference must not exceed 5 °C to avoid undesired internal heat exchanges (L. He *et al.*, 2023).

Several affirmed technologies have been proposed as TMS, classifying them by the external power source and the working fluid choice (Maiorino *et al.*, 2024; Gómez Díaz *et al.*, 2025; Wen *et al.*, 2025). The first classification has been made as follows:

1. *Active TMSs*: They use external power (from the EV battery pack or the grid) to drive compressors, fans, or pumps, and forcibly remove or supply heat to the cells. The compressor is used in a refrigeration unit that cools a working fluid. Fans or pumps deliver the working fluid mass flow inside the hydraulic circuit from the refrigeration unit to the battery pack.
2. *Passive TMSs*: They rely on natural convection or latent heat, without requiring an external power source for proper functioning, and are highly suitable for moderate loads and as buffers during fast transients. No compressors, fans, or pumps are required.

A combination of these two technologies defines the *hybrid TMSs*. They can handle heat under more severe, continuous, or fast-charge conditions than passive systems can manage alone and consistently outperform single-mode systems in both peak temperature and temperature uniformity (Jay R. Patel and Rathod, 2020; Mohamed, Bal and Sahoo, 2025).

The secondary working fluid subdivides these categories into several TMSs, depending on the substance used as coolant (Murugan *et al.*, 2022; L. He *et al.*, 2023; Maiorino *et al.*, 2024). The active TMSs are subdivided into *air-based*, *liquid-based*, and *refrigerant-based* technologies when air, liquids (such as water), and refrigerants interact with the battery pack, respectively. The battery pack can be cooled or heated through direct contact with the coolant when the working fluid is air or liquid dielectric fluids. When water is used as a secondary working fluid, or the refrigerant of the refrigeration unit evaporator is directly employed, a heat exchanger is required. Instead, the passive TMSs generally implement *Phase Change Materials (PCMs)* (Liu *et al.*, 2020a) or *Heat Pipes (HPs)* (Weragoda *et al.*, 2023) without any secondary fluid flow.

The heating phase can be realised through external heat sources that recover or generate thermal energy outside the battery pack (Hu *et al.*, 2020b). PTC Heaters, electric motors, or hardware components, such as capacitors or inverters (Hu *et al.*, 2020a), produce thermal energy directed to the battery pack through the secondary working fluid or passive devices (PCMs and HPs) (R. Guo *et al.*, 2023; He *et al.*, 2024). Other technical solutions implement the refrigeration unit as a heat pump, warming up the battery pack using the condenser as a heat source (Lee *et al.*, 2023). The energy source of these devices can be the battery pack itself or the electric grid if the battery pack cannot supply electric energy due to extremely low ambient temperatures below −20 °C (Wu *et al.*, 2020a; Huang, Chen and Zhou, 2022). In recent years, several researchers have focused attention on *internal heating strategies*. These systems raise the battery pack temperature through the internal heat generation caused by the Joule effect and polarization losses (Wu *et al.*, 2020b). Shorter warm-up times, improved efficiency, and a more uniform temperature field are the leading advantages of this technique compared to the previous technologies (Hu *et al.*, 2020b). However, the procedure must be carefully controlled to avoid lithium plating and accelerated aging (B. Sun *et al.*, 2023). Categories and subdivisions of internal heating strategies are still evolving, and no mature or standardised classifications can be evidenced. One of the latest subdivisions was proposed by Wang et al. (Y. Wang *et al.*, 2025), who made a clear distinction between internal heating strategies, including *Alternating-Current heating*, *Direct-Current heating*, *pulse heating*, and *Self-Heating Lithium-ion Battery (SHLB)*. Recently, *compound self-heating* strategies have been published in the literature. They are defined as hybrid technologies that couple pure self-heating techniques and traditional external heating systems. These techniques are proposed as optimal heating techniques to achieve speed, efficiency, and temperature uniformity while limiting accelerated degradation and lithium plating (Ruan *et al.*, 2021).

The following paragraphs describe recent numerical and experimental studies of these TMSs, reporting their features and results. The classification is structured by dividing active and passive TMSs, while hybrid TMSs and the internal heating strategies are briefly discussed as separate technologies.

II.2.1 Active Thermal Management Systems

II.2.1.1 Air-based TMS

Air-based TMSs utilise forced convection of air to maintain the battery pack's temperature within the optimal working range. In past years, battery packs were cooled through natural convection. However, as reported by Akinlabi et al. (Akinlabi and Solyali, 2020a), it is almost impossible for natural air cooling alone to provide adequate conditions for the modern EVs' battery packs. Forced convection systems are widely used in EVs due to their simple structure, high reliability, low cost, and simple maintenance (Hamed *et al.*, 2022). Reviews agree that air cooling is structurally simple, low-cost, light, and reliable, with no leakage risk and easy integration with vehicle HVAC (Shahjalal, Shams, M. E. Islam, *et al.*, 2021; Maiorino *et al.*, 2024). Air is easily recoverable in nature, is not toxic or inflammable (Zhang, Liu and Tian, 2011), and has no impact on the environment. For this reason, air-based TMSs achieve safety standards regarding the secondary fluid flammability and limit atmospheric pollution (J. Lin *et al.*, 2021a). Finally, air is a dielectric fluid and cannot cause short circuits caused by potential leaks (Roe *et al.*, 2022a).

Air-based TMSs are classified by how air is cooled or heated and how the mass flow is delivered through the pipe network. Several articles in the literature (Jaguemont and Van Mierlo, 2020; Zhao *et al.*, 2021; Maiorino *et al.*, 2024) distinguish air treatment techniques into two categories:

1. *Active treatment*: Part of the exhausted air is brought to the system's inlet and mixed with air aspirated from the environment. A heat exchanger regulates the air temperature directed to the battery pack. The treatment concerns both cooling and heating modes, using the evaporator of the refrigeration unit or external heaters (PTC heater or heat pump).
2. *Passive treatment*: The inlet air flow from the environment is directly treated by a heat exchanger and does not mix with the outlet flow. Some configurations can provide exhausted air injection after the heat exchanger dedicated to the treatment.

Active and passive treatment layouts are schematised in Figure II.8.

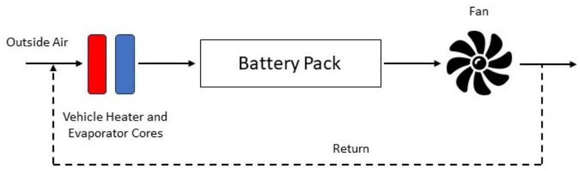

(a)

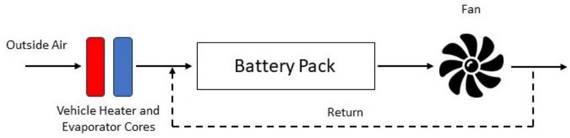

(b)

Figure II.8 *Active (a) and passive (b) air treatment (Maiorino et al., 2024)*

Weaknesses of air-based TMSs concern the lower efficiency of the heat transfer between air and the battery pack due to the lower thermal conductivity and heat capacity compared to liquids or two-phase refrigerants. According to several articles in the literature (Kim, Oh and Lee, 2019; Chen *et al.*, 2022; Hwang *et al.*, 2024), for high-capacity battery packs, fast charging, hot climates, and heavy-duty EVs, other systems are increasingly preferred due to higher heat flux capability and better control of temperature uniformity and runaway propagation. The low air density compared to other fluids (such as liquids) represents another typical issue. The improvement of air-side heat transfer is usually obtained by higher velocity or added structures (such as heat sinks or fins) than liquid-based or refrigerant-based systems, raising pressure drop and the fans' required electric power (Akinlabi and Solyali, 2020b; Sahin, Gocmen and Cetkin, 2022). Finally, the inlet air flow from the outside may bring dust and other pollutants inside the pipe network, worsening the heat exchange between the air and the battery pack (Shahjalal, Shams, M. E. Islam, *et al.*, 2021).

In recent years, several studies have been published in the literature concerning air-based TMSs. The Authors aimed to overcome the well-known vulnerabilities of this technology, proposing novel air duct shapes that enhance air-side heat transfer and reduce pressure drops. As reported by He et al. (L. He *et al.*, 2023), the first distinction is generally made between *serial ducts* and *parallel ducts*. In the serial ducts, the airflow direction is characterised by a perpendicular orientation to the major surfaces of the battery cells. In the parallel ducts, the flow direction follows a parallel path to the major surfaces of the battery cells. Figure II.9 shows the schematic representation of these two arrangements.

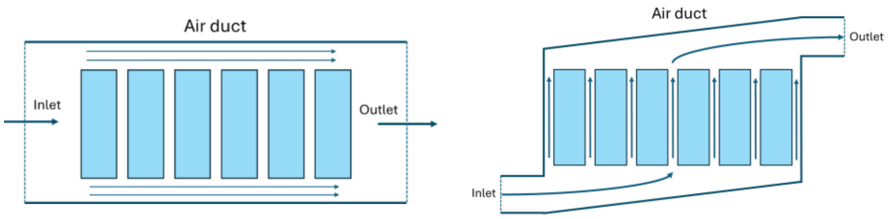

(a) (b)

Figure II.9 *Serial (a) and parallel (b) ducts*

Both configurations assume a more complex shape by arranging inlets and outlets in various positions. As reported by Jaguemont et al. (Jaguemont and Van Mierlo, 2020), Figure II.10 indicates possible shapes of the ducts and airflow directions that interact with the battery pack.

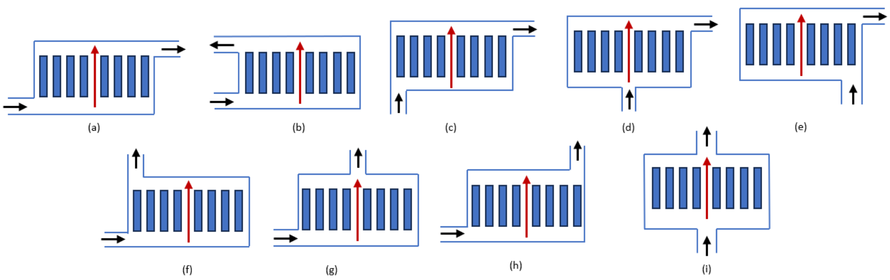

Figure II.10 *Several arrangements of serial and parallel ducts for air-based TMSs (Jaguemont and Van Mierlo, 2020)*

Among these, Shen et al. (Shen *et al.*, 2023) developed a modified novel Z-shaped duct formed by inclined battery pack cells. As represented in Figure II.11, a specific inclination angle characterises the cells because the direction of the major surfaces is not perpendicular to the duct's horizontal edges on the reference plane.

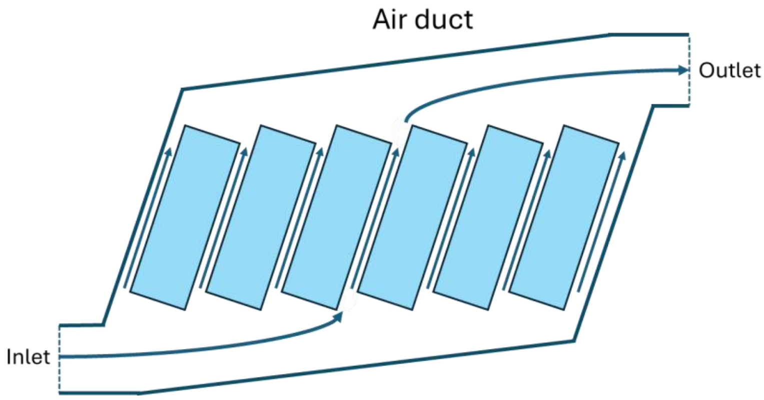

Figure II.11 *Modified Z-shape duct proposed by Shen et al. (Shen et al., 2023)*

Several inclinations were numerically analysed to find the best configuration. According to the results, the maximum temperature and the maximum internal span were 36.9 °C and 2.4 °C, corresponding to −3.4% and −5.8% of a conventional parallel arrangement, as Figure II.9 (b). Xu et al. (Xu *et al.*, 2022) proposed a numerical and experimental parametric analysis of a U-shaped duct for an air-based TMS. The study found the best arrangement of the duct inlet to decrease the peak temperature of the battery pack. The results showed that the inlet position of 30 mm achieved a reduction of 4.2 °C of the maximum battery pack temperature compared to the initial guess of 20 mm. Instead, an increment of the inlet airflow velocity from 2 $m \cdot s^{-1}$ to 5 $m \cdot s^{-1}$ achieved a higher peak temperature decrease from the 8.5 °C of the initial guess to 18.5 °C. Zhang et al. (Zhang *et al.*, 2021) developed a numerical analysis of a novel T-shaped duct. This solution can be interpreted as a union of the Z-shaped and the U-typed solutions. According to the results, this technology reduced the battery pack's maximum temperature and the maximum temperature span by 2.2% and 90.8%, respectively. Figure II.12 shows the proposed T-shaped duct schematically.

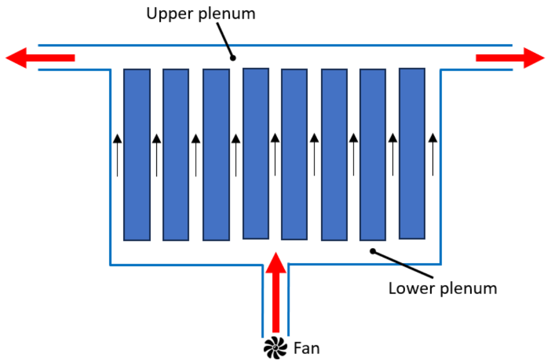

Figure II.12 *T-shaped duct developed by Zhang et al. (Zhang et al., 2021)*

Other studies focused attention on the overall performance of the air-based TMS, both in heating and cooling modes. Xu et al. (Xu *et al.*, 2023) implemented an air-based thermal management system with two heaters composed of polyamide films and nickel sheets. These layers are attached to the upper and bottom surfaces of a sleeved heat spreader plate. This plate is a sleeved structure with a large heat exchange conductive area used to pre-heat and cool the battery cells. The experimental setup was realised by a 12.5 Ah battery pack formed by an orthogonal arrangement of 20 Li-ion cells connected in a 5P4S configuration. For an ambient temperature of 25 °C, a 3C constant discharge rate, and an inlet air velocity of 1 $m \cdot s^{-1}$, the temperature increment and span were respectively 12.9 °C and 2.8 °C in cooling mode. Considering an ambient temperature of −20 °C and heating mode operation, the system achieved a heating rate of 7.0 $°C \cdot min^{-1}$.

II.2.1.2 Liquid-based TMS

Liquid-based TMSs are the dominant solution for high-power EV battery packs. Liquids are employed as a secondary working fluid and are more efficient than air due to the higher heat capacity and thermal conductivity (J. Liu *et al.*, 2023). According to several studies in the literature (Jithin and Rajesh, 2022; Roe *et al.*, 2022b; Anisha and Kumar, 2023a). Properly designed liquid-based systems can be thousands of times more effective than air-based TMSs in terms of heat transfer. The typical layout of a liquid-based TMS is formed by a closed secondary loop characterised by a pump, a heat exchanger, and a heater (Maiorino *et al.*, 2024). The heat exchanger is required in cooling mode to decrease the liquid temperature directed to the battery pack. The battery pack cooling is realised through a dedicated refrigerator unit, which generally corresponds to the HVAC system of the EV (Cen, Li and Jiang, 2018). The heating mode can be achieved by employing the HVAC system as a heat pump or implementing a separate PTC heater (Lv *et al.*, 2022). Part of the electric motor's wasted heat can be reused for heating the battery pack (Xiao Ang Liu, Zhang, *et al.*, 2024). The typical liquid-based TMS layout is represented in FigureII.13.

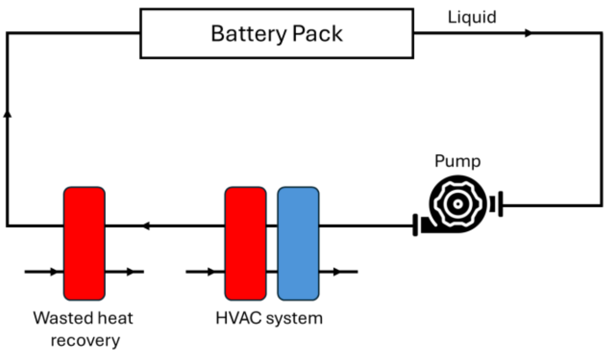

Figure II.13 *A typical Liquid-based TMS layout for EVs*

The liquid-based TMSs are subdivided depending on how the liquid interacts with the battery pack surfaces. There are three different typologies (Maiorino *et al.*, 2024):

1. *Immersive cooling*: The battery pack is completely immersed in a dielectric fluid. Dielectric oils with high specific heat and good stability are generally preferred (Sundin and Sponholtz, 2020). This solution achieves the highest cooling capacity and temperature uniformity among liquid-based TMSs (Zhao *et al.*, 2023).
2. *Direct cooling*: The battery pack surface is in direct contact with the liquid, but the single conductive parts are not involved. The coolant is generally guided in channels or jackets, and dielectric fluids should be employed (Anisha and Kumar, 2023b). Water and glycol mixture can be used as a secondary fluid, but the battery cells must be insulated for safety reasons using thin polymer layers (Zhou *et al.*, 2025).
3. *Indirect cooling*: The generated heat is removed through a solid and thick interface between the battery pack surface and the liquid. This interface can be a cold plate, distinct piping, or jackets. Despite the additional conductive resistance between the battery pack and the coolant (Han *et al.*, 2022), this solution can potentially use any existing liquid without risks of a short circuit (Dardiri *et al.*, 2024). These liquid-based TMSs generally use water and glycol mixtures to reduce the coolant costs compared to dielectric fluids (Roe *et al.*, 2022b).

Despite liquid-based TMSs achieving higher efficiency than air-based systems, there are issues related to plant complexity and risks of leaks. When dielectric oils are employed as a coolant, the pumping losses increase due to their higher viscosity compared to water (Roe *et al.*, 2022b). Although immersion cooling achieves the highest thermal efficiency among the liquid-based TMSs, the arrangement complexity arises, and the system becomes more expensive due to large fluid volumes, sealings, and sensors (Roe *et al.*, 2022b; C. Song *et al.*, 2024). While direct cooling achieves a higher effective contact area between the coolant and the battery pack, dielectric fluids cause rapid corrosion of materials and require specific compatibility with jackets and battery cell coatings (Han *et al.*, 2022). Leakages can compromise the system's safety due to direct contact between electrodes and coolant, especially when water and glycol mixtures are used as a working fluid (Zhou *et al.*, 2025). Indirect cooling is the cheapest liquid-based TMS, but it achieves the lowest thermal efficiency among them. Extra thermal resistance limits the heat dissipation from the battery pack, despite the leakages remaining outside the electrical domain (Han *et al.*, 2022). Despite the higher number of components compared to air-based TMSs, indirect water and glycol cooling is the most mature and efficient technology for EVs (Maiorino *et al.*, 2024).

Various studies have been proposed in the literature in recent years, most focusing on the thermal and hydraulic optimisation of the liquid channels through FEM analysis. Larrañaga et al. (Larrañaga-Ezeiza *et al.*, 2022) proposed a numerical and experimental research concerning a novel direct cooling strategy for EVs based on dielectric fluids. The idea was to embed U-shaped channels within the battery pack shell to maximise contact and heat extraction. The study focused on thermal and hydraulic efficiency, estimating the battery pack temperature field and the pressure drops. The NMC battery pack achieved a maximum temperature of almost 30 °C when the coolant's volumetric flow rate was 0.43 $l \cdot min^{-1}$. Instead, the maximum temperature span within the battery pack was equal to 0.4 °C. According to the Authors, an indirect cooling system could not have achieved the thermal efficiency. Numerical analysis showed that, at the same volumetric flow rate, the maximum temperature would have been 38.9 °C, while the maximum internal span would have reached 5.7 °C. These values disagree with the optimal temperature range and the maximum span limit of 5 °C. He et al. (P. He *et al.*, 2023) proposed an innovative cold plate formed by I-shaped channels, employed for a 40 Ah Li-ion battery pack. The numerical results demonstrated how the system managed the battery pack temperature, decreasing the peak value from 33.9 °C to 30.8 °C. Fractal structures inspired the double-layered I-shaped channel arrangement formed by inlets positioned on the lateral surface. The liquid coolant interacts with battery cells through a halfway slab. The opposite lateral surface manages the cold plate outlet. According to the Authors, multichannel cold plates increase the overall thermal conductivity and the heat exchange efficiency, reducing the battery pack cooling rate. Zuo et al. (Zuo *et al.*, 2023) proposed a numerical analysis of two U-minichannel cold plates clamped to the front and back surfaces of a prismatic Li-ion battery cell, reducing the maximum temperature reached by the cells. The cold plate controlled the maximum cell temperature to 38.7 °C for an inlet coolant velocity of 0.01 $m \cdot s^{-1}$ at 1C constant discharge rate. Zhang et al. (Y. Zhang *et al.*, 2022) numerically investigated the effects of an inclined channel cold plate compared to a straight channel cold plate for different coolants. They evaluated the *j/f factor*, defined as the ratio between the non-dimensional surface heat transfer and the surface friction factor. According to the results, the cold plate performance is influenced by several factors, including the choice of coolant, mass flow rate, number of channels, and the inclination angle. The overall system efficiency increased when the inclination angle was maximised. The *j/f factor* improved by 79.6% for a 0.6 $g \cdot s^{-1}$ water mass flow, 5 channels, and an inclination angle of 15°. Zuo et al. (Zuo *et al.*, 2022) proposed a numerical comparison between a single S-channel and double S-channel cold plate for thermal management of a prismatic 20 Ah Li-ion battery pack. The Authors studied indirect cooling employing a mixture of water and glycol at three different discharge rates (3C, 4C, and 5C). The results showed that the double S-channel cold plate limited the maximum temperature spans compared to the single-S cold plate. The battery pack's peak temperatures were almost similar. Regarding the pressure drops, the double S-channel improved the hydraulic efficiency of the system by reducing the pumping power to 73.9% compared to the baseline.

While most research focused on channel optimisation, Li et al. (D. Li *et al.*, 2023) investigated the effect of pulsating and steady flows on heat exchange efficiency and energy consumption. They proposed a numerical study of a multi-channel cold plate and ran distinct simulations by changing the mass flow frequency. The frequency and amplitude of the mass flow rate influence heat dissipation and pressure drops. According to the results, at the same thermal load, a frequency and amplitude of 3 Hz and 30% of the steady state velocity, the pump energy consumption decreased by 5.2%.

II.2.1.3 Refrigerant-based TMS

While the air-based and the liquid-based TMSs employ a secondary working fluid, such as air or water, the refrigerant-based technology manages the battery pack temperature directly through the refrigerant of the refrigeration unit. Many concepts share the vapor-compression loop with the cabin by using electronic expansion valves and branch circuits (Wang, Huang and He, 2022; Maiorino *et al.*, 2024). The HVAC system controls cabin and battery pack temperatures independently in mixed cooling and heating modes. In hot climates, a dedicated evaporator dissipates the generated heat through cold plates formed by minichannels where a refrigerant (such as R290, R1234yf, and R32) evaporates (Maiorino *et al.*, 2024). In cold climates, the HVAC system operates as a heat pump, directing hot refrigerant from the compressor outlet to the battery pack heat exchanger. According to the benchmarks, preheating from subzero ambient temperatures can be achieved in 9 to 15 minutes, reaching battery pack temperatures above 0 °C. As a result, the refrigerant-based system is generally 30.6 % faster in heating mode compared to an indirect liquid-based system and reduces energy demand by 57 % (Guo and Jiang, 2021a; Lian *et al.*, 2023). The research conducted by Guo et al. (Guo and Jiang, 2021b) clearly explain how the battery pack cold plate can be implemented in the HVAC of EVs. Figure II.14 shows the refrigerant-based TMS layout, the cooling mode, heating mode, and combined cabin heating and battery pack cooling flow circuit diagrams.

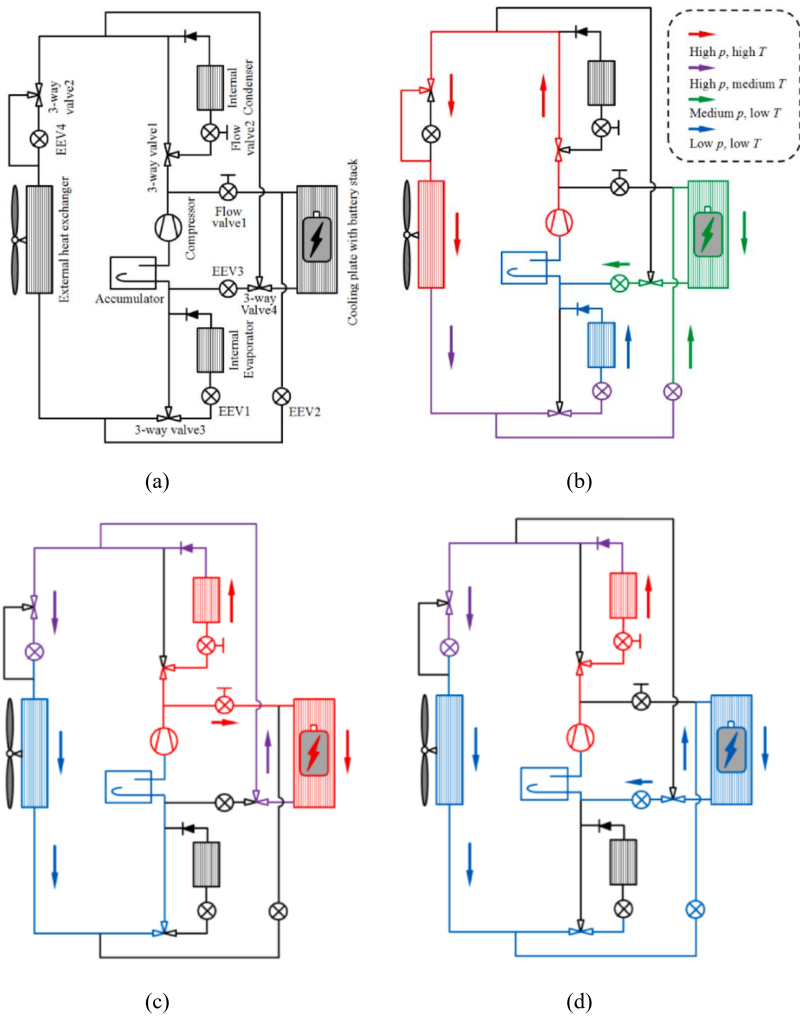

Figure II.14 *Layout of the refrigerant-based TMS proposed by Guo et al. (Guo and Jiang, 2021b) (a) representing the cooling mode (b), heating mode (c), combined cabin heating and battery pack cooling (d)*

Fig II.14 (b) represents the cooling mode. The refrigerant at high pressure and high temperature is directed to the external condenser and to the expansion valves from the compressor. The refrigerant expands and is conducted to the battery pack cold plate and the cabin heat exchanger. Figure II.14 (c) shows the heating mode. The outlet refrigerant flow goes to the cabin heat exchanger and to the battery pack cold plate. Then, the refrigerant condenses and is directed to the expansion valves. The external heat exchanger works as an evaporator. The last mode in Figure II. 14 (d) explains the system as a heater for the cabin and a cooler for the battery pack. The hot outlet refrigerant flow from the compressor condenses inside the cabin heat exchanger, reducing its temperature. Then, it is directed to an expansion valve to reduce its temperature. After the expansion, the refrigerant evaporates into the outdoor evaporator. Successively, the refrigerant is subjected to a further expansion before the battery pack cold plate. Finally, the working fluid returns to the compressor.

A strong standpoint of refrigerant-based TMSs relies on the two-phase heat exchange, which achieves the highest heat transfer coefficients compared to air and liquids (Hong *et al.*, 2020). Particularly for pure substances and azeotropic mixtures, the constant temperature during evaporation and condensation results in an improved uniformity of the battery pack temperature field compared to single-phase fluids. Instead, air-based and liquid-based TMSs suffer from inevitable temperature change between the inlet and the outlet, which is generally diminished by oversizing the mass flow rate.

However, refrigerant-based TMSs have drawbacks concerning the system complexity, refrigerant safety regulations, and control requirements. The layout requires compressors, expansion valves, seals, and careful routing, which increase costs and potential leak points (Lin *et al.*, 2024). As suggested by Figure II.14, the battery pack cold plate implemented in the HVAC system requires more parallel branches than air-based and liquid-based systems. The system complexity also regards trade-offs between the cabin air conditioning and the battery pack thermal management. Although the integration of the refrigerant-based TMS into the HVAC system significantly reduces bulk and weight, the control strategy must ensure the cabin comfort needs while controlling the battery pack temperatures (Jamsawang *et al.*, 2024). In some cases, the overall efficiency of the HVAC can be penalised under harsh drive conditions (Zhou *et al.*, 2024). A major extension of the refrigerant circuit and the addition of junctions and connections increase the risk of leaks, which are regulated by safety standards due to the possible flammability of several refrigerants (such as the R1234yf belonging to the A2L category) (Kang *et al.*, 2024). High operating pressures related to the compression vapour cycle introduce another issue. The pipeline must be mechanically robust and lightweight to sustain the radial stress applied by the refrigerant and reduce mass increment to the vehicle (Lin, Cen and Jiang, 2021).

Recent research focused on the main weaknesses of refrigerant-based TMSs, and several articles can be found in the literature. Wu et al. (Wu, Zhou and Wang, 2020) investigated the influence of the refrigerant choice on the HVAC system COP when EV battery pack thermal management is implemented. The COP was estimated in cooling and heating mode, assuming a cabin temperature of 24 °C and six ambient temperatures. According to the results, the COP estimation was similar for all the substitute refrigerants, except for CO_2 (or R744). R290 and R152a achieved the best performances in every environmental condition. Figure II.15 shows the complete results.

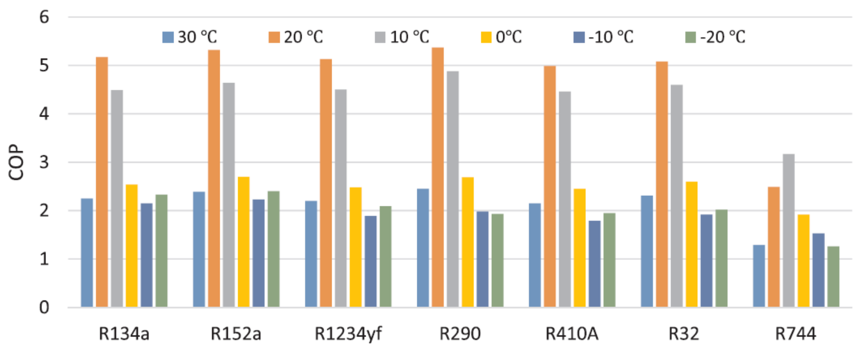

Figure II.15 *COP estimations for different environment temperatures and a cabin set-point of 24 °C according to the Wu et al. (Wu, Zhou and Wang, 2020) analysis*

Song et al. (P. Song *et al.*, 2024) investigated the development and optimisation of a TMS for EVs based on CO_2 employed as a natural refrigerant. The system was designed to manage the cabin air conditioning, the battery pack, and the electric motor thermal management simultaneously. The study defined 16 different modes, including cabin heating and cooling, battery pack preheating and cooling, and wasted heat recovery from the electric motor. The target was to manage the battery pack temperature below 40 °C when emulating the standard WLTC in dynamic conditions. According to the results, several optimal values of the gas cooler pressure were found. This parameter assumed values between 98.51 bar and 109.28 bar, corresponding to the cabin-only mode and the cabin and electric motor management mode. In these conditions, the TMS reached COP of 2.75 and 2.25, respectively. The lowest COP was 1.62, and it was found for the cabin and battery pack management mode. The study highlights that the proposed TMS cannot maintain the battery pack temperature below 40 °C when the internal generation rate is 0.8 kW, demonstrating that CO_2-based TMSs are not yet a completely mature technology. Xu et al. (N. Xu *et al.*, 2024) proposed an innovative control strategy based on fuzzy logic to overcome the combined functioning of the cabin air conditioning and the battery pack thermal management. The temperature target of the battery pack was set to 25 °C, while the internal generation assumed values within 2 kW and 3 kW. A compressor, a condenser, two expansion valves, and two parallel evaporators formed the system layout for contemporary cooling in hot climates. The control system managed the mass flow rate and the expansion valve openings, balancing the refrigerant flow on both branches. According to the results, the control board limited the battery pack temperature fluctuations within ±0.5 °C over time. The thermal performance improved when comparing the baseline liquid-based system at the same conditions, increasing the COP by 10% - 15%.

II.2.2 Passive Thermal Management Systems

II.2.2.1 Phase Change Materials-based TMS

Phase Change Materials (PCMs) are substances with a high heat of fusion that can absorb or release a large amount of heat when there is a phase change. PCM-based TMS for Li-ion batteries is based on the melting and solidification of materials near the battery pack operating temperature, generally through the solid-to-liquid transition (Selvnes *et al.*, 2021). A vast array of substances can be used for this purpose, including paraffin, fatty acids, and hydrated salts (J. Luo *et al.*, 2022). Desirable properties for engineering applications include a suitable melting point, high latent heat, good thermal and chemical stability, absence of supercooling, low toxicity, and a reasonable cost (Yang, King and Miljkovic, 2021). Li-ion batteries generate heat that is primarily absorbed as latent heat during PCM melting. When the melting occurs at a constant temperature, such as in pure substances and eutectic mixtures, the battery pack interacts with a substance characterized by a uniform temperature field (J. Luo *et al.*, 2022). This feature enhances the temperature uniformity of the battery pack over time, providing a more effective option than air-based and liquid-based TMSs. As reported previously, PCM-based TMSs are passive systems and do not require external power sources (Maiorino *et al.*, 2024).

However, there are several key limitations of this technology. Low thermal conductivity represents the first weakness. Paraffin has thermal conductivities between 0.1 $W \cdot m^{-1}K^{-1}$ and 0.3 $W \cdot m^{-1}K^{-1}$ (Jaguemont and Van Mierlo, 2020), while for fatty acids and hydrated salts this parameter lies between 0.15 – 0.3 $W \cdot m^{-1}K^{-1}$ (Al-Ahmed *et al.*, 2020) and 0.5 – 1 $W \cdot m^{-1}K^{-1}$ (Yizhe Liu, Li, *et al.*, 2024), respectively. This feature causes local heat accumulation and a slow response under high C_{rate} or hot ambient conditions (Nasiri and Hadim, 2025). This issue is generally overcome by implementing high-conductivity foams, fins, heat sinks, and nano-additives, but costs, bulk, and weight increase (Alipanah and Li, 2016). Another issue concerns leaks and deformation of enclosures, which may have poor mechanical strength and vibration resistance. This issue is particularly critical when mechanical abuse of Li-ion battery packs occurs, as it increases the risk of thermal runaway (Liu *et al.*, 2020b). Regarding flammability, many organic PCMs are flammable, increasing the risk of fires and explosions. Flame-retardant additives, inorganic and salt-hydrate PCMs are preferred, but their employment may reduce the available latent heat for storage or cause corrosion (Weng *et al.*, 2022). For these reasons, many design works are based on single-cell applications or short-duration tests. Commercial applications for the EV sector remain challenging due to the high capacity of battery packs and the aggressive drive cycles characterized by high currents and hot climates (Jiang *et al.*, 2020). Furthermore, the absence of standard design methodologies and validation protocols under abusive and lifetime conditions penalises the technology dissemination on the market (Airò Farulla *et al.*, 2023).

Several studies have been proposed in the literature in recent years. Youssef et al. (Youssef *et al.*, 2022) proposed an experimental study of a paraffin/graphite PCM contained in plexiglass cases that surround the battery pack cell. The maximum temperature reduction and the temperature difference between the cells were measured in three distinct cases: no cooling, PCM cooling, and PCM plus jute fibres. The immersed jute fibre decreases the maximum battery pack temperature by operating as a heat sink. According to the results, the PCM plus jute fibre configuration achieved a maximum temperature reduction from 46 °C to 35 °C. Instead, the maximum temperature span reached 3.1 °C. Verma et al. (Verma and Rakshit, 2022) proposed a numerical analysis of a novel cooling system formed by PCM plates positioned between the battery pack pouch cells in a sandwich configuration. Regarding the PCM choice, the Authors indicated fatty acids as a better substance due to their wide range of favourable properties compared to paraffin. A battery module formed by four pouch cells was simulated. The results showed a decrease in the maximum battery temperature, achieving 16 °C, 22 °C, and 26 °C by choosing three distinct PCM plate thicknesses (7 mm, 9 mm, and 12 mm). Longitudinal fins were employed to promote heat dissipation through the environment. Their thickness was 30 mm. The TMS expertly managed the internal temperature field, obtaining a maximum temperature span under 5 °C. Huo et al. (Huo *et al.*, 2023) numerically investigated a novel *composite PCM* formed by glass fibres and paraffin. Composite PCMs are defined as ordinary PCMs that have been combined with supporting structures or fillers to overcome the previously reported weaknesses (Q. Huang *et al.*, 2021). A first numerical analysis compared a single battery module formed by 9 Li-ion cells arranged in a 3P3S configuration. The numerical simulations showed 60% is the best percentage of glass fibres, while vertical orientation guarantees heat insulation and protection from mechanical abuse. Findings reveal that the composite phase change module with a glass fibre mass fraction of 60%, operating at a discharge rate of 3C, maintained a temperature 0.76 °C lower than the baseline air-cooled module. The maximum temperature difference between the modules decreased from 7.3 °C to 5.0 °C, while the maximum temperature ratio decreased from 16.9% to 11.6%. Other studies focused on how the PCM's low thermal conductivity can be used as a thermal insulation feature during abnormal working conditions, such as thermal runaway. As specified by Shi et al (Shi *et al.*, 2023), low thermal conductivity PCMs or composites act as an insulating layer, which slows or prevents cell-to-cell thermal runaway propagation, because heat from a failing cell cannot easily spread through the material. However, the key challenge lies in optimal trade-offs between cooling performance and fire propagation inhibition, due to performance loss in normal operation (Ling *et al.*, 2018).

II.2.2.2 Heat Pipes-based TMS

Heat Pipes are widely investigated for Li-ion battery TMSs because they offer high thermal conductivity, passive operation, compact form factors, and long lifecycles (Weragoda *et al.*, 2023). An HP is defined as a closed-tube casing that embeds a saturated fluid (Maiorino *et al.*, 2024). The two-phase heat exchange dissipates heat to the environment through evaporation and condensation of the working fluid. The proposed technology is defined as a passive technique because HPs do not require compressors, fans, or pumps. The working principle is based on three components (Maiorino *et al.*, 2024):

1. *Evaporator*: The evaporator is the HP component directly in contact with the battery pack. The saturated fluid evaporates due to the battery pack's internal generation, dissipating heat.
2. *Condenser*: The hot vapour interacts with the colder environment through the condenser, where the fluid condenses and returns as liquid.
3. *Adiabatic section*: This part connects the evaporator and the condenser and permits an adiabatic flow between the two chambers. Vapour and liquid flows are achieved inside the component through natural convection or capillarity (Smith *et al.*, 2018).

HPs achieve an optimal temperature control of the battery pack (average temperatures below 40 °C even at high C_{rate}) (Jouhara *et al.*, 2021), excellent uniformity of the temperature field by obtaining the optimal target under 5 °C spans, and integration flexibility (Smith *et al.*, 2018). These devices are easy to implement in well-tailored shapes (such as flat, loop, micro, oscillating, and flexible pipes) to prismatic, pouch, and cylindrical cells. Contrary to direct liquid cooling, there is no requirement for electrical isolation of the cells because the fluid is confined within the closed-tube casing (Wu *et al.*, 2024). Several studies (Gan *et al.*, 2020; Jouhara *et al.*, 2021; Wu *et al.*, 2024) explicitly describe HPs as a safer technology than liquid-based TMSs because any coolant loop can be kept physically remote from cells. Many battery-oriented HPs use water, alcohol, or acetone as a working fluid, but dielectric fluids can be deliberately selected (Gan *et al.*, 2020). Indeed, dielectric fluids are chosen for systems where the fluid can be in direct contact with cells (L. Xu *et al.*, 2024).

There are principally three typologies of HPs used for the Li-ion battery pack TMSs (Maiorino *et al.*, 2024):

1. *Sintered-wick Heat Pipe*: It is formed by a sealed tube partially filled with working fluid. A sintered wick made of metal powder (copper or stainless steel) on the inner wall provides the capillary effect (Chang *et al.*, 2021). The fine and interconnected pores provide strong capillary pumping to return condensate to the evaporator against gravity.
2. *Pulsating Heat Pipe*: A long capillary tube bent into many meanders is partially filled with working fluid, forming liquid slugs and vapor plugs. The heating process inside the evaporator produces pressure differences that drive the self-excited oscillations of slugs and plugs along the closed circuit, transporting the dissipated heat to the condenser through latent and sensible heat.
3. *Loop Heat Pipe*: It consists of a closed loop with a separate evaporator and wick, a vapor line, a condenser, and a liquid return line. The working fluid follows a loop from the evaporator to the condenser through capillary pressure at the wick-liquid-vapor interface. This feature enables the dissipation of heat over long distances through the circulation of the working fluid (Zhao, Wei and Dan, 2024).

Like the previous technologies, there are many drawbacks and challenges to overcome. Despite being compact devices, the capillary mechanism behind HPs is more complex than other TMSs (Y. Huang *et al.*, 2021). Performance strongly depends on layout, contact area, working fluid, and orientation. The incorrect placement or sizing of HPs causes stagnation of the working fluid and dry-out phenomena due to the difficulty in realizing capillarity effects (Jouhara *et al.*, 2021). Other issues concern durability. Heat Pipes can suffer from working-fluid leaks, permeation of non-condensable gases, and uncertain long-term performance, especially for the flexible and oscillating HPs (Weragoda *et al.*, 2023). For this reason, their adoption for large-scale EV is still limited due to the incomplete maturity of the technology, especially under rapid load fluctuation and varying ambient conditions (Y. Huang *et al.*, 2021). Particularly concerning the thermal loads, Heat Pipes alone can often be insufficient for large battery packs of EVs, and they must be combined with other TMSs (forming a hybrid TMS). Various articles in the literature report typical heat rates that the HPs can dissipate. As reported by Behi et al. (Behi *et al.*, 2021), a single sintered-wick HP used for LTO battery packs can dissipate 100 W of internal generation rate, which can increase to several hundred Watts when multiple pipes are employed. Zamanifard et al. (Zamanifard *et al.*, 2023) report pulsating HPs can dissipate a wide range of heat load rates, defined between 100 W and 800 W when arranged in modules. Finally, loop HPs reach the maximum heat dissipation rate among the Heat Pipes. As described by Singh et al. (Singh and Nguyen, 2022) and Wu et al. (Wu *et al.*, 2015), loop HPs for thermal management of EVs' battery packs can dissipate up to 500 W and reach a maximum of 600 W.

Although HPs are generally coupled with other TMSs, there are few studies in the literature where Heat Pipes are proposed as stand-alone TMSs for Li-ion. Behi et al. (Behi *et al.*, 2020a) described a novel thermal management technique using HPs during high current discharging of a Li-ion battery used in EV packs. The research focused on the HPs implementation as a stand-alone solution for single cells and coupling them with liquid-cooling for modules. The Authors experimentally demonstrate that a single flat HP can be partially efficient for an 8C discharge because it dissipates 29.1% of the thermal load in cooling mode. A numerical analysis indicated which zones may benefit from the HPs implementation due to local critical hot spots. However, the proposed cooling system for a typical EV battery pack of 15 cells required a liquid-based TMS, demonstrating that these devices have weaknesses in stand-alone applications. Zhang et al. (Zhang and Wei, 2020) experimentally and numerically analysed a novel HP-based TMS formed by flat Heat Pipes inserted between the battery cells. This is a completely passive TMS, whose efficiency was increased through the implementation of cooling fins. While the evaporator was arranged in direct contact with the battery cells, the condenser dissipated heat to the environment through aluminium fins. According to the results, the maximum temperature rise was reduced by 81.0% and 44.3% when the heat pipe was used in natural convection and coupled with the aluminium plate. The maximum temperature differences for natural convection and the aluminium plate were 8.6 and 2.3 °C. When the HP was employed, the battery pack temperature was 73.7% lower than the former and 50.1% lower than the latter. As the discharge rate increased, the maximum temperature rose, and the maximum temperature difference also increased. Thus, the thermal management requirements became increasingly severe. At the end of the 2C discharge, only the aluminium plate and heat pipe cooling could satisfy the maximum temperature difference requirement. For an 8C discharge rate, the maximum temperature difference did not meet the requirement for every configuration.

II.2.3 Hybrid Thermal Management Systems

Hybrid TMSs are defined as a combination of at least two of the previous technologies to improve performance (Jaguemont and Van Mierlo, 2020).

Generally, active and passive systems are coupled to achieve the high capacity and uniformity of the passive elements while relying on active cooling when needed. PCMs and HPs are integrated with air-based, liquid-based, and refrigerant-based systems, employing smaller pumps, fans, or compressors than the conventional technologies. This standpoint is achieved by passive devices that work as buffers, reducing the effective working hours of active systems. Instead, the high capacity and uniformity of passive elements, while relying on active cooling only when needed, reduce parasitic power and improve safety and lifetime (Jay R Patel and Rathod, 2020). As reported by several studies (Awasthi, Nirmalkar and Tiwari, 2025; Parveen, 2025), hybrid TMSs achieve higher thermal efficiency by reducing the peak temperature and temperature gradients of battery packs, even in extremely hot environments. In recent years, PCMs and liquid-based systems have been the most extensively studied combination, often implementing fins or metal foams to increase thermal conductivity (Awasthi, Nirmalkar and Tiwari, 2025). PCM offers thermal inertia and uniformity, while liquid thermal management relies on efficient and mature technology to remove the stored heat within PCMs (Hyun, Kim and Shin, 2025).

Despite being more effective than conventional TMSs, hybrid systems are characterised by several weaknesses that reduce their applicability to real EV battery packs. For this reason, literature lacks long-term field data, and more studies should be conducted. The first issue relies on the system complexity. The number of involved devices increases over conventional technologies, while advanced control strategies are required to coordinate passive and active elements, avoiding over-cooling or inefficient operation. The components and interfaces increment makes hybrid TMSs more expensive than conventional technologies, reducing the effective economic benefits on the market. Instead, coupling so different techniques causes reliability and maintainability issues due to the increasing risk of leakage, fouling, or failure. Other weaknesses concern weight and space because passive devices occupy volume and increase mass compared to minimal active systems, especially air-based TMSs.

Lots of studies have been published due to the tremendous development possibilities. Yang et al. (Yang *et al.*, 2023) proposed a numerical simulation of a hybrid TMS by coupling PCM and indirect liquid cooling. The Authors developed an innovative cold plate formed by Z-shaped channels coupled with RT35 paraffin and aluminium foam. The main characteristic was the implementation of PCM within the aluminium cold plate to achieve a weight and volume reduction of the overall system. The aluminium foam was implemented to resolve the low thermal conductivity issue typical of PCM-based TMSs. A baseline case without paraffin and another eight cases featuring different numbers of channels were compared, estimating the battery pack temperature field and the energy demand at 1C, 2C, and 3C discharge rates. According to the results, the optimal hybrid design was 53%

lighter than the baseline system due to the lower weight of paraffin and aluminium foam. Regarding energy demand, the hybrid system achieved 50% lower consumption compared to the traditional liquid-based TMS. The required energy was reduced because PCM increased thermal inertia, which managed the battery pack temperature over a longer period due to its capacity to store and release heat gradually. As a result, the battery pack's average temperature reached values below 40 °C. PCM integration and the choice of the coolant channel typology improved the thermal efficiency because Z-shaped liquid distribution is more uniform compared to other shapes, such as U-shaped or J-shaped ducts, even at high C_{rate}. Liu et al. (Z. Liu *et al.*, 2023) numerically investigated a hybrid TMS by combining PCM and liquid-based cooling for a Li-ion battery pack formed by 16 cylindrical cells (18650 type). The system employed water as a coolant with an inlet velocity of 0.01 $m \cdot s^{-1}$ distributed among nine inlet sections. The system managed the battery pack temperature in extreme conditions featuring a 5C constant discharge and a 40 °C ambient temperature. The peak temperature of the battery pack was maintained below 46.2 °C, while the maximum internal temperature span reached values lower than 4.2 °C. The Authors achieved a significant improvement by coupling the liquid-based system with PCM due to the baseline peak temperature of 69.2 °C, which corresponds to 9.2 °C more than the maximum allowable threshold. A successive improvement consisted of implementing expanded graphite within the paraffin to create a composite PCM-based TMS. The thermal conductivity rose, and the peak battery pack temperature dropped by 7.66 °C compared to the previous hybrid system. The optimal graphite mass fraction was defined between 12% and 16%. The numerical results showed that higher percentages may reduce the available PCM latent heat, affecting the overall efficiency. The research continued by implementing cooling fins between the PCM and the water channels. This solution was preferred because the maximum internal span was reduced to 3.51 °C, improving the temperature uniformity of the battery pack. Kermani et al. (Mehrabi-Kermani, Houshfar and Ashjaee, 2019) presented an innovative hybrid TMS design by coupling paraffin PCM and active air-cooling technology. The experimental study aimed to enhance the safety and the efficiency of a Li-ion pouch battery under high-stress conditions. The system employed a high-porosity copper foam that embedded the paraffin used as PCM, while the forced-air cooling system used a pin-fin heat sink to dissipate the thermal load over time. The metallic foam was necessary to improve the paraffin thermal conductivity and distribute the heat load uniformly. According to the results, the system mitigated the risk of thermal runaway at an airspeed of 3.2 $km \cdot h^{-1}$ due to the PCM latent heat and the copper foam. Indeed, the effective thermal conductivity of paraffin and metallic foam increased to 11.98 $W \cdot m^{-1}K^{-1}$, corresponding to almost 10 times higher than stand-alone paraffin PCM-based TMSs (Maiorino *et al.*, 2024). Experimental results demonstrated that the hybrid TMS maintains the battery average temperature below 55 °C, even at low air speed. The copper foam outperformed conventional passive and active cooling methods in thermal stability over time and energy efficiency. As stated by the Authors, the average battery pack temperature exceeded 60 °C after 2400 s by coupling the PCM and the air-cooling system, while the overall temperature was 53.5 °C after 6500 s after implementing metal foam. Behi et al. (Behi *et al.*, 2020b) studied the performance of a hybrid TMS of a single LTO cell by implementing a flat HP. According to the workflow, a preliminary experimental investigation was necessary to understand the cell temperature during critical conditions, corresponding to 8C discharge. A thermal camera was employed to identify the heat distribution on the cell surfaces, discovering the hot spots. Successively, several tests were performed to compare a hybrid TMS formed by coupling the flat HP and a forced air-cooling system. The first comparison demonstrated how forced air-cooling improves the overall efficiency of the hybrid system compared to the stand-alone HP-based TMS by reducing the average cell temperature from 56.9 °C to 49.4 °C. The next step was CFD analysis to investigate the efficiency increment of substituting the active air-based TMS with a liquid-based system. The simulations considered a battery pack module arranged with 15 pouch cells identical to the tested one. According to the results, a standard liquid-based system produced a 29.9% decrement in the average module temperature compared to the natural convection case. The application of the flat HP brought a significant improvement to the system, reducing the module temperature by 32.6% to the natural convection baseline. The numerical analysis demonstrated the superiority of liquid-based TMSs compared to air-based solutions, even in hybrid technologies.

II.2.4 Internal heating strategies

II.2.4.1 Alternating-Current heating

Alternating-Current (AC) heating is a method that uses AC through the battery pack cells to generate heat, enabling fast and uniform warm-up of Li-ion batteries in cold climates (X. Huang *et al.*, 2024). Due to the bidirectional current shape, the net charge in a charging and discharging cycle is zero, like the chemical energy stored within the battery, excluding the wasted heat. Major control variables are (Zhu *et al.*, 2016):

1. *Frequency*: Lower frequency generally increases heat generation per Ampere but raises lithium plating risk.
2. *Amplitude*: A larger current increases the heating rate but accelerates degradation when plating on electrodes or overvoltage occurs.
3. *Waveform*: Sinusoidal, rectangular, and pulsed AC produce different heating efficiency and degradation behaviours.

Modern AC heating can provide fast and uniform preheating with modest energy cost due to the continuous charge and discharge cycles. This feature is realised especially when frequency, amplitude, and waveform are optimised by following the constraints made to avoid lithium plating (J. Li *et al.*, 2019). Regarding hardware, AC internal heaters use bidirectional buck-boost converters, resonant switched-capacitor circuits, and wireless charging coils to avoid bulky low-frequency inverters, resulting in a more compact design and higher efficiency than traditional external TMSs (Shang *et al.*, 2020). As Huang et al. (X. Huang *et al.*, 2024) report, the employment of buck-boost converters and wireless charging coils produces temperature increments of the battery pack from –20 °C to 0 – 5 °C in a few minutes. At the same time, the compactness achieves low costs and reduced weight of the battery pack compared to heat pumps and PTC heater solutions (Hu *et al.*, 2022).

However, uncontrolled AC heating represents the principal weakness of this technique. The lithium plating risk represents the main issue, which manifests in critical cold environments, high amplitudes, and low frequencies. Improper parameter choice can generate a degradation boundary line in the current-frequency plane, beyond which aging accelerates (Zhu *et al.*, 2016). Even applying safety parameters cannot be considered reliable because specific domain cell chemistry is often derived from limited test matrices or models (W. Li *et al.*, 2023). Some frameworks explicitly show a temperature limit below which target heating cannot be achieved without violating plating or voltage constraints (R. Huang *et al.*, 2024).

To overcome these problems, Zhang et al. (Zhang *et al.*, 2020) experimentally investigated a novel multistage AC heating strategy for minimising the warm-up time without incurring the lithium plating. The first analysis discussed a trade-off between the battery aging and warm-up time depending on the chosen frequency. According to the results, the temperature growth manifested an evident rise and gradual stabilisation due to the balance between heat generation and dissipation. Higher frequencies increase the temperature ratio, realising the battery pack heating procedure faster. According to the Authors, the optimal frequency was 100 Hz. Once the optimal frequency was found, the second analysis investigated the influence of amplitude by choosing values of 3 A, 6 A, and 15 A. After 1000 s, the temperature of the battery pack reached −15 °C, −10 °C, and 15 °C, starting from an initial temperature of about –20 °C. According to the results, the most efficient and rapid amplitude was 15 A despite the formation of plating on the electrodes. This outcome demonstrates that high amplitudes produce faster warm-up but promote lithium plating.

II.2.4.2 Direct-Current heating

Direct-Current (DC) heating strategy relies on controlled battery pack discharge current to generate heat through the Joule effect and polarisation losses, exploiting the high internal resistance of Li-ion cells at low temperatures. The DC is drawn from the cell and brought to other cells or to an external load, while ohmic and electrochemical phenomena convert part of the electric energy into wasted heat (Y. Wang *et al.*, 2025). Compared to AC heating, the DC method is structurally simple, easy to control, and less prone to lithium plating on the anode when the terminal voltage is kept within safety limits (S. Han *et al.*, 2025). Indeed, while AC heating needs adding circuits formed by converters, inductors, and coils, this technique exclusively uses the battery cell electrodes and a control board (Cai *et al.*, 2022).

The drawbacks lie in SOC consumption and range impact. Discharge-only techniques inevitably draw part of the stored energy within the battery pack, producing issues related to energy management during the procedure (S. Han *et al.*, 2025). Instead, aggressive low-voltage discharge (finalised to limit lithium plating) produces high discharge rates in accordance with the typical polarisation curve of battery cells. This approach sharply accelerates capacity fade and aging phenomena, reducing the battery pack's useful life (L. Xu *et al.*, 2024).

Recent studies in the literature investigated the optimal trade-off between heating efficiency and speed, energy consumption, and limited risk of thermal runaway. Among these, Ruan et al. (Ruan *et al.*, 2019) experimentally investigated the optimisation of DC discharge heating strategy, considering both heating time and lifetime reduction of an 8 Ah Li-ion pouch cell subjected to a 2C discharge. According to the results, the DC discharge heated the pouch cell from –30 °C to 2.1 °C in 103 s, losing only 1.4% of the total capacity after 500 heating cycles. According to the Authors, no significant lifetime deterioration was found. Regarding the thermal voltage, a lower discharge voltage shortened the heating time but significantly increased the capacity fade. An unheated pouch cell and a DC-heated cell were compared to understand the effective advantage in lifetime at the same environmental conditions. The discharge and charge powers of the heated pouch cell were 8.7 and 32.7 times higher than those of the unheated, while the drawn energy at constant discharge was 62.46 times higher. Han et al. (S. Han *et al.*, 2025) proposed a PSO-based dynamic DC discharge strategy by optimising current over time to jointly minimise heating time and capacity loss across different ambient temperatures. According to the Authors, this approach effectively overcomes the limitation of traditional constant current discharge methods, which struggle to adjust current intensity based on real operating conditions. The results showed heating ratios capable of increasing the Li-ion battery temperature from –30 °C to 0 °C faster than conventional DC strategies, reducing the procedure time by 48.71 s. In contrast to other preheating methods, the capacity degradation was just 0.10 Ah after 1000 heating cycles.

II.2.4.3 Pulse heating

Pulse heating has emerged as the leading strategy for battery heating, particularly to address degradation issues at low temperatures. It consists of applying controlled current pulses to generate heat rapidly and uniformly within the cells. Pulse heating methods include DC pulse, AC pulse, and bidirectional pulse current waveforms. Among these, AC pulse heating and bidirectional pulse approaches often provide higher heating efficiency and best temperature uniformity, significantly higher than the previous techniques (such as DC heating) (Huang *et al.*, 2023). Typical heating rates are generally included between 2.9 $°C \cdot min^{-1}$ and 11 $°C \cdot min^{-1}$, depending on the waveform and parameters (C. Wang *et al.*, 2025). Instead, the higher uniformity of the internal temperature field reduces the risk of hot spots that provoke localised degradation (Vu and Shin, 2020), reducing aging and the risk of lithium plating. Regarding energy demand, lower consumption is a principal feature of pulse heating, especially when compared with DC and AC heating methods (Cai *et al.*, 2024). This edge was strengthened by implementing optimisation algorithms that improve energy efficiency and reduce heating time, or by a fuzzy logic-controlled variable pulse amplitude strategy (Huang *et al.*, 2020; Fan *et al.*, 2024). These findings indicate that carefully designed pulsating current waveforms, especially those that adapt to battery SOC and temperature, can significantly lower energy demand while maintaining rapid and uniform heating. According to various studies published in the literature (Ji and Wang, 2013; Zhu *et al.*, 2016; Huang *et al.*, 2023), pulse heating offers significant advantages that make this technology highly attractive for EVs and energy storage systems operating in cold climates.

The drawbacks of pulse heating lie in the complexity of control algorithms, parameters, and costs. Despite having many advantages compared to other strategies, the choice of parameters (such as amplitude, duty cycle, and frequency) can reduce the usefulness of this technique. Improper parameters can accelerate degradation due to the formation of lithium plating (Qin *et al.*, 2020), especially when pulse amplitude exceeds a certain threshold. Self-adaptive pulse amplitude or pulse-width modulations are vital for thermal and energetic efficiencies, but the system complexity and cost increase compared to other simpler internal heating methods (W. Li *et al.*, 2023). When DC heating does not require any additional components and AC heating relies on hardware, pulse heating requires a specific algorithm and sensors that may not be reliable in certain cases.

For this reason, studies on pulse heating have focused principally on the parameter choice to guarantee efficiency in dynamic conditions. Han et al. (Han *et al.*, 2024) presented an experimentally validated numerical analysis of a 17.7 kWh high-power Li-ion battery pack of 96 prismatic NMC cells subdivided into 8 modules. The application concerned the automotive sector, and the battery pack was designed to power a 100 kW electric motor. The study aimed to reduce the heating ratio in cold climates by defining the optimal current thresholds to avoid lithium plating. According to the results, the pulse parameters achieved a heating rate of 6.8 °C·min^{-1} at an initial temperature of 0 °C. The internal heating strategy also reduced the total charging time by 31% compared to the baseline without preheating, and in critical conditions of 5% initial SOC. The numerical simulations achieved excellent internal temperature uniformity with maximum temperature spans of 0.2 °C in the cell cores and 0.7 °C in the battery pack enclosures. The optimal pulse was a bidirectional waveform with a frequency of 2 Hz and a maximum amplitude of 100 A. The Authors recommended activating the heating procedure below an ambient temperature of 15 °C because preheating is unnecessary in temperate and hot climates. Li et al. (Li *et al.*, 2025) investigated the lithium plating formation during bidirectional pulse heating at low temperatures using a refined physics-based electrochemical-thermal model. The research highlighted that while bidirectional pulse heating is effective for rapid temperature recovery, it poses significant degradation risks, particularly at high SOC and current rates. Due to internal temperature gradients, lithium plating was more severe in the outer cells of a battery module. The Authors identified specific lithium precipitation temperature thresholds, such as –6.9 °C at 0.5 SOC and 2C rate, beyond which plating ceased. Due to the higher internal equivalent resistance of the battery pack, heating efficiency reached its peak at lower SOCs. To mitigate these risks, the study proposed an innovative stepped rate pulse strategy that dynamically adjusts the pulse current based on the found temperature boundaries, successfully achieving plating-free heating that balances thermal performance with battery health and safety.

II.2.4.4 Self-Heating Lithium-ion Battery (SHLB)

Wang et al. (C. Y. Wang *et al.*, 2016) invented a particular device called the Self-Heating Lithium-ion Battery (SHLB), consisting of a Li-ion prismatic battery characterised by a nickel foil embedded between the cells. The functioning principle is based on a switch that connects the negative electrode and an activation terminal. The activation terminal is linked to the nickel foil that heats up through the Joule effect within the battery. A control board monitors the battery pack temperature at a specific representative point to control the switch's opening and closing. When the temperature signal drops below the lower threshold, the switch opens. The current then flows through the nickel foil, powering the thermal load because the foil's resistance and the electric load are in series. When the battery reaches the optimal temperature range, the switch closes. This prevents the current from passing through the nickel foil again because closing the switch creates a short circuit between the negative electrode and the activation terminal, stopping electron flow in the metallic lamina. The functioning is clarified in

Figure II.16, which represents the SHLB architecture and the equivalent circuit.

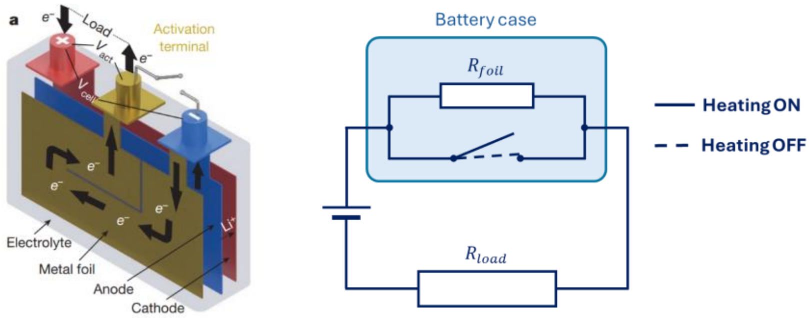

(a) (b)

Figure II.16 *SHLB architecture developed by Wang et al. (C. Y. Wang et al., 2016) and its equivalent circuit*

The Authors numerically investigated the thermal performances of a 7.5 Ah SHLB at two different ambient conditions. According to the results, the battery achieved 0 °C in 19.5 and 29.6 seconds for initial temperatures of –20 °C and –30 °C. Both simulations concluded that the warm-up required only 3.8% and 5.5% of the battery capacity, demonstrating also sustainability in terms of energy consumption. Wang et al. (C.-Y. Wang *et al.*, 2016) continued the research on SHBL, realising a prototype. The experimental analysis consisted of a 3C fast charge test starting from an initial temperature of –30 °C to emulate critical cold climates. In 14 minutes, the nickel foil increased the battery temperature to 10 °C, corresponding to a temperature rate of 2.9 $°C \cdot min^{-1}$. According to the Authors, the SHLB achieved a heating period 11.4 times faster than conventional heating systems in cold climates.

Further research on SHLBs found several weaknesses. The ohmic heat generation of the nickel foil produces large internal temperature gradients within the battery, caused by non-uniform current distribution that may affect heating time and energy efficiency (Yang, Zhang and Wang, 2016). The risk of thermal runaway is a significant safety issue, especially when battery aging occurs. According to several studies (He *et al.*, 2020; Mao *et al.*, 2020; Gao *et al.*, 2025), the self-heating potentially triggers ignition at lower temperatures and under certain SOC. Instead, accelerated degradation mechanisms caused by lithium plating may decrease the critical temperature for self-ignition, increasing fire hazards. For these reasons, despite being a compact heating solution for Li-ion batteries, further improvements are needed to transform SHLB into a mature technology for EVs.

II.2.5 Compound self-heating

The compound self-heating strategy integrates multiple heating mechanisms to rapidly and efficiently preheat batteries, ensuring performance and safety in cold climates. The integrated systems rely on both internal and external heating techniques reported in the previous paragraphs. Compound self-heating may utilise pulse-width modulation, parallel oscillation topologies, or embedded heating elements to achieve efficiency and uniform heating, without relying on external power sources (Ruan *et al.*, 2021). At the same time, PTC heaters, heat pumps, and electromagnetic induction can rapidly raise the battery pack temperature from subzero to optimal operating conditions without risks of lithium plating, thermal runaway, and accelerated degradation (Zhang, Jin and Li, 2017; J. Han *et al.*, 2025). The scope lies in fast heating rates, energy efficiency, minimal battery degradation, and maximum design flexibility for various battery pack arrangements and chemistry (Ruan *et al.*, 2023). According to several studies published in the literature (Yang, Zhang and Wang, 2016; Yang, Liu and Wang, 2017; Ruan *et al.*, 2022), compound self-heating can preheat batteries from –20 °C to 0 °C in under 100 seconds, significantly faster than traditional methods. Regarding energy demand, these hybrid techniques typically consume only 2 – 8 % of the battery pack capacity, preserving the stored energy for operation. As several articles report (Zhu *et al.*, 2020; Ruan *et al.*, 2021; Tao *et al.*, 2024), advanced design and control strategies reduce temperature gradients within the battery pack. This feature minimises risks of localised degradation or safety hazards, reducing capacity loss to less than 3 – 8% after hundreds of heating cycles (Jiang *et al.*, 2018).

Like the other techniques, compound self-heating is characterised by drawbacks to overcome. The integration of multiple heating mechanisms and control algorithms increases the complexity of design and manufacturing. Generally, a multi-objective optimisation is required to balance heating speed, energy efficiency, and battery health, because aggressive or poorly controlled heating may still cause lithium plating and faster aging (Wang and Yan, 2025). Trade-offs between heating speed, energy efficiency, and long-term battery health are often required to guarantee the principal features typical of this technology (Yin *et al.*, 2021). Regarding the temperature field, there are internal heating strategies characterised by issues of uniformity within the battery cells. For instance, the SHLB can be affected by hot spots caused by the non-uniformity of the current distribution inside the nickel foil. These temperature gradients can potentially lead to uneven aging or safety issues (Zhu *et al.*, 2020).

Several studies have been published in the literature to overcome the typical drawbacks of the compound self-heating strategy. Among these, Ruan et al. (Ruan *et al.*, 2022) experimentally optimised the heating system of a single 8 Ah pouch cell, with adaptive and precise swarm optimisation, enhancing discharge power and energy while maintaining good adaptability across SOCs and temperatures. The system lies on a DC internal self-heating strategy coupled with an external heater formed by two aluminium foils arranged on the pouch cell's external surfaces. According to the results, the proposed system achieved a heating rate of 32.5 $°C·min^{-1}$. Compared to a non-heated 8 Ah pouch cell, the tested device achieved 7.4 times higher discharge power, 19.0 times higher charge power, and 109.9% greater discharge energy. Results showed that the hybrid strategy improved the heating system by increasing the available discharging energy to 70.4% above the baseline. According to the Authors, aluminium foil guaranteed a low-cost, lightweight, and easy-to-adapt system that can be considered mature and ready for industrial applications. Luo et al. (Luo *et al.*, 2023) experimentally investigated a hybrid heating technology formed by a PCM-based TMS and DC self-heating strategy. The research was conducted on a commercially available battery pack (Panasonic NCR18650BP) consisting of ten 18650 cylindrical Li-ion cells arranged in a 5S2P configuration. The battery pack was embedded in a composite PCM formed by paraffin and expanded graphite, imposing a reciprocal spacing of 25 mm between the cells. A DC-DC converter was implemented to manage the DC battery terminal voltage and precisely control the current during preheating. The experimental tests were performed at environmental temperatures of –10 °C and –20 °C by measuring the cells' average temperature using type K thermocouples in representative points. According to the results, the proposed system achieved a heating rate of 17.1 $°C·min^{-1}$ by employing a DC of 9.6 A. A maximum temperature difference of 3.6 °C between the cells demonstrates that the composite PCM achieved overall thermal uniformity within the battery pack, avoiding extended gradients. The control strategy's influence on the energy consumption was investigated through an energy conversion model implemented in Simulink. The model was developed to help the TMS in following the optimal preheating strategy and obtaining the maximum discharge energy.

II.3 Current status, challenges, and future perspectives

II.3.1 Status of TMSs in the automotive sector

In the past years (specifically in the 2000s), most of the EVs employed air-based TMSs for their battery packs, and *Honda Insight* (Zolot *et al.*, 2001) and *Nissan Leaf* (Yang *et al.*, 2019) were leaders in their field. Over the years, the development of more efficient liquid-based TMSs changed the thermal management paradigm of EVs, gradually substituting the obsolete air-based systems. Among these, Nissan radically changed its design approach to an indirect cooling system based on a liquid mixture of water and glycol, proposing the *Nissan Arya* (Driving electric, 2022). In recent years, other automotive brands have launched their EVs (such as Audi, BMW, Mercedes, Porsche, Toyota, and Volkswagen), all characterised by indirect cooling TMSs despite the typologies significantly varying (sports cars, sedan cars, and SUVs) (Maiorino *et al.*, 2024). The *McLaren Speedtail* represents an exception because it employs an immersion-cooling system based on dielectric oil (TeamSpeed, 2020). It represents one of the first commercially available sports cars by adopting immersive cooling for the Li-ion battery pack (Roe *et al.*, 2022b). BMW attempted a different approach, launching the *BMW i3* in 2017 (Maiorino *et al.*, 2024). The HVAC system was employed in the TMS, realizing one of the first commercial refrigerant-based technologies. However, this technique was abandoned when the *BMW i4 eDrive40* proposed an indirect liquid thermal management technique for its Li-ion battery pack (Maiorino *et al.*, 2024).

One of the most complex and innovative liquid-based TMS for EVs was developed by Tesla. The Tesla TMS is a liquid-based technology that uses the vehicle's HVAC system as a refrigeration unit or heat pump, depending on the external climate conditions. The *octovalve* represents the pioneering device that makes the Tesla TMS so unique. A detailed scheme is shown in Fig II. 17.

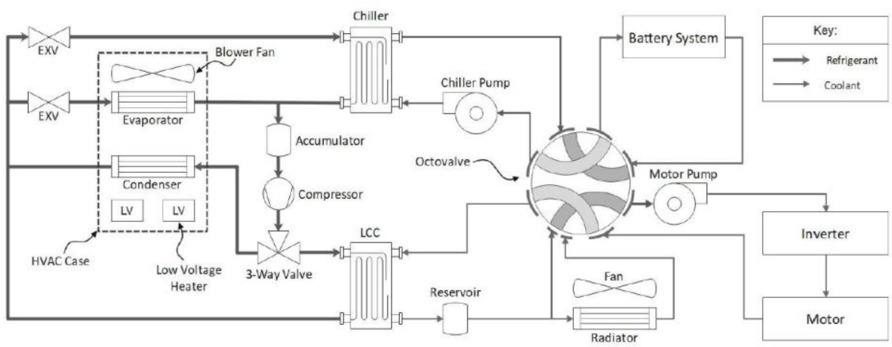

Figure II.17 *Detailed scheme of the TMS patented by Tesla (Mancini et al., 2019)*

It is a rotation valve formed by 8 ports that allows and blocks the coolant flow in the different liquid circuit branches. As reported inside the patent registered by Tesla (Mancini *et al.*, 2019), the TMS adopted in all Tesla EVs operates in five states, each capable of multiple functions depending on the system requirements:

1. *Parallel mode*: Two parallel liquid loops are employed. The first one connects the drive unit (electric motor, inverter, and transmission) and the radiator, while the second one manages the battery. The interaction between the hot refrigerant at the compressor outlet and the electric motor, inverter, and transmission is achieved by the

Liquid Cooled Condenser (LCC). Instead, the chiller works as the HVAC system evaporator, cooling the battery pack. This state permits increasing the drive unit temperature to 50 – 60 °C, while the battery pack is cooled to achieve the optimal temperature target.

2. *Series mode*: The water flows sequentially through the drive unit, the radiator, and the battery pack into a unique secondary loop. This configuration is chosen to maximise the cooling effect of the TMS, achieving uniformity of the powertrain temperatures.
3. *Ambient source mode*: This state is used to integrate heat from the environment when the wasted heat from the drive unit and battery pack cannot manage the cabin temperature itself in cold climates. The radiator preheats the coolant at subzero temperatures by recovering heat from the environment. In some cases, the secondary loop can include the drive unit and the battery pack to recover other wasted heat from the powertrain components. The heated water interacts with the refrigerant through the chiller heat exchanger, which works as an evaporator. The HVAC operates as a heat pump, managing the cabin temperature.
4. *Wasted heat recovery*: This state recovers heat from the drive unit to warm the battery pack and the EV cockpit, representing one of the fundamental innovations of the TMS. The octovalve directs the liquid to the drive unit. The water recovers the wasted heat of the electric motor, inverter, and transmission, transferring part of it to the battery pack. The water flows to the chiller heat exchange, where the air conditioning refrigerant evaporates and recovers part of the drive unit's wasted heat. The HVAC operates as a heat pump to warm the EV cabin. The radiator is bypassed, achieving a TMS completely independent of environmental temperature.
5. *Series radiator bypass*: The secondary loop of this state works exactly as the *series mode*, but the radiator is bypassed. This strategy is used in subzero cold climates, avoiding the heat dissipation to the environment and promoting faster warming of the drive unit and the battery pack.

The system extremises the concept of energy efficiency by defining several working states to recover wasted heat and increasing the HVAC system's performance. The complexity lies in managing different heat loads by keeping comfortable conditions within the EV cabin, even in cold climates. The heating and cooling benchmarks represent significant features of the Tesla TMS. As highlighted by Wray et al. (Wray and Ebrahimi, 2022), TMSs that implement octovalve can preheat the EV battery pack for ambient temperatures lower than – 10 °C, while maintaining the cells between 30 °C and 35 °C in critical hot environments.

II.3.2 Status of TMSs in the railway sector

Battery Electric Multiple Units (BEMUs) are full electric battery trains that are emerging as a promising solution to decarbonise rail transport, especially on non-electrified or partially electrified lines. These trains rely on onboard battery packs to power electric motors, eliminating emissions related to Diesel engines and reducing the environmental impact (Mwambeleko and Kulworawanichpong, 2017). According to Popovich et al. (Popovich *et al.*, 2021), battery trains can achieve ranges of around 100 to 450 km, depending on the battery pack size and configuration. At the same time, energy consumption can be roughly half than conventional trains, offering both environmental and economic benefits. Streuling et al. (Streuling *et al.*, 2021) founded this outcome, analysing the primary energy saving between BEMUs and Diesel locomotives considering the power grid mix of Germany. According to the results, the development of BEMUs benefits from the integration with renewable energy sources and smart charging infrastructures, which can reduce lifecycle costs and increase grid reliability. Hybrid configurations that combine batteries and fuel cells, or partial overhead electrification, can extend range and operational flexibility, as demonstrated in train models tested in Italy, where full electric and fuel cell vehicles successfully replaced Diesel engines, while maintaining performance on real routes (Fragiacomo *et al.*, 2022; Pugi and di Carlo, 2024).

Li-ion batteries are increasingly used in railway applications, similarly to the automotive sector. An effective TMS is necessary to manage the optimal battery pack temperature, prevent thermal runaway, and extend the lifespan. Liquid-based and hybrid systems are generally preferred for their superior heat transfer capabilities and readiness, especially in high-power density battery packs for trains (Putra *et al.*, 2025). As for the automotive, both heating and cooling are necessary (X. Zhang *et al.*, 2022). The battery train industry is led by the major manufacturers (such as Stadler, Alstom, Siemens, Hitachi, and CRRC) to actively integrate advanced technologies into rolling stock to ensure safety, efficiency, and reliability in several environments. As reported by Boev et al. (Boev *et al.*, 2023), Alstom developed the first passenger operation of BEMUs in a project started in 2016, while other players successively developed their products. Currently, several commercially available BEMUs are available, such as the *Alstom Cordia Continental BEMU*, the *CAF Civity*, the *Siemens Mireo Plus B*, the *Hitachi Rail Blues*, and the *Stadler FLIRT Akku* (Wieser *et al.*, 2025). Literature lacks details about the TMSs of commercially available BEMUs, but their general features can be found in official technical documents and research papers.

II.3.3 Challenges and emerging issues of Li-ion battery thermal management

Despite the improvements and various studies published in the literature, several challenges are emerging concerning the thermal management of Li-ion batteries. As described previously, effective TMSs are essential to prevent issues such as thermal runaway, capacity degradation, and non-uniform temperature distribution within the battery packs. Active, passive, and hybrid technologies propose solutions to these issues, but each one has both useful advantages and critical drawbacks. This paragraph aims to report common issues affecting TMSs, identifying the principal questions that research and industries must resolve to achieve optimal thermal management of Li-ion battery packs in critical hot and cold environments.

Li-ion batteries are highly sensitive to temperature, with performance and safety compromised outside the optimal temperature range. Major challenges include the thermal runaway propagation caused by overheating and mechanical abuse (Srinivasan *et al.*, 2020), non-uniform heat generation and dissipation that produce localised hotspots (Shahjalal, Shams, Md. E. Islam, *et al.*, 2021), and accelerated degradation and performance decay caused by both high and low temperatures (X. Zhang *et al.*, 2022). Especially in cold weather, lithium plating and dendrite formation remain critical issues that current TMSs struggle to control properly, limiting costs, energy demand, and reliability. From a general perspective, active and passive technologies mutually compensate for their thermal weaknesses, finding the optimal trade-off by employing hybrid strategies. However, combining different TMSs increases costs and cannot offer the maturity for industries to confront regulatory frameworks in terms of safety and integrity. Internal heating strategies, despite offering the highest heating rates, suffer from lithium plating risks when non-optimised control strategies are employed, increasing battery pack aging.

The common challenge affecting all TMSs concerns inadequate internal temperature monitoring. While significant progress has been made in developing advanced cooling and heating strategies, no single solution fully addresses the diverse challenges posed by high energy density, fast charging, and operation in extreme environments (J. Lin *et al.*, 2021b). Most systems rely on surface sensors characterised by a lack of readiness, missing rapid internal changes that precede failure or dangerous phenomena (Srinivasan *et al.*, 2020), such as fires and explosions in hot weather or unusable vehicles in cold climates due to lithium plating. Accurate, real-time models for heat generation and dissipation are still under development, especially for complex battery packs (Guo *et al.*, 2025). Prediction models can significantly improve efficiency, especially when aging predictions are made to prevent degradation when battery packs must power certain thermal loads.

II.3.4 Future perspectives

According to the forecasts to 2033 presented by IDTechEx (Edmondson, 2023), air-based and liquid-based TMSs will remain dominant technologies for EVs on the market. Indirect cooling will continue to use large cold plates beneath or above the cells, while the channel shapes and paths will enhance the thermal management efficiency of Li-ion battery packs. The implementation of thermally conductive adhesives will fill thermal insulating air gaps between the battery pack and plates.

Interesting studies about novel liquids are opening opportunities to increase the thermal conductivity of coolants (Maiorino *et al.*, 2024). New substances can be employed to improve heat transfer for indirect, direct, and immersion cooling systems. Researchers are proposing two principal substitutes:

1. *Nanofluids*: They consist of liquids where solid particles made of metal (aluminium, copper, nickel, silver, or metal oxides) or silicon dioxide are incorporated to increase thermal conductivity. For instance, as reported by Liu et al. (Liu *et al.*, 2006), 0.1 vol% of copper particles in conventional fluids increases thermal conductivity by 23.8%.
2. *Liquid metals*: Several liquid metals (such as mercury or gallium) have been studied as substitutes for water and glycol mixtures due to their higher thermal conductivity. An electromagnetic pump is required for liquid metal flows, achieving lower noise and reliability than conventional pumps (Deng *et al.*, 2018). However, the employment of these devices increases the costs and complexity of the system. Despite their thermal advantages, liquid metals are generally unsuitable for immersion cooling systems because their high electrical conductivity poses risks of short circuits and electrical hazards (Xiang, Liu and Fan, 2022).

Other future technologies lie in Thermoelectric Modules (TEMs) (Maiorino *et al.*, 2024). These are lightweight, noiseless, and compact active thermal components that convert electricity into thermal energy by the Peltier effect. Compact size, absence of moving parts and fluids, and the ability to easily switch between cooling and heating modes are their principal strengths (Zhao and Tan, 2014). Yi et al. (Yi *et al.*, 2023) reported an interesting benchmark by experimentally studying a 5 W Li-ion battery. According to the results, the TEM maintained the average battery temperature at a constant 25 °C, achieving overall uniformity with a maximum internal variation of 4.7 °C.

Chapter III
Thermal Modelling of Li-ion Battery Cells in Natural Convection

III.1 Introduction

This chapter proposes a simplified thermal model based on the ECM method. The scope is delineating a general procedure to estimate the average temperature, the temperature field, and the internal heat generation rate in natural convection over time by employing the Bernardi et al. (Bernardi, Pawlikowski and Newman, 1985) equation, simple empirical correlations, and a reliable equivalent circuit. The temperature field can be obtained through the FEM by implementing the general heat conduction equation and appropriate Robin boundary conditions. The model was tested on a cylindrical 18650 LTO cell subjected to two typical discharging current profiles at 1C in natural convection. Three correlations for the Nusselt number found in the literature were applied. The formulas were proposed by Churchill and Chu (Churchill and Chu, 1975), Morgan (Morgan, 1975), and Kuehn and Goldstein (Kuehn and Goldstein, 1976). Two input current profiles were implemented to emulate a continuous and a partial discharge test. Their shapes were defined considering typical C_{rates} and discharge cycles of 1500 mAh LTO cells. The simplified thermal model was validated experimentally to analogise the numerical results with a solid reference established on empirical experience in a laboratory.

Although these results were strong evidence of the simplified thermal model's reliability, the experimental validation could not provide a criterion of choice for the best empirical correlation. CFD simulations were developed to obtain the dissipated heat rate exclusively from the temperature field of the air surrounding the cell. This approach also allowed the implementation of a more complex geometry for the analysis, demonstrating which Nusselt correlation can be used despite being obtained for simple cylindrical shapes. Once the results of the CFD simulations were experimentally validated, the comparison of dissipated heat rate trends through the Root Mean Square Error (RMSE) showed that Morgan’s formula is the most suitable correlation for the continuous discharge test. The Churchill and Chu correlation best approximates the dissipated heat rate of the partial discharge test. Due to the low order of magnitude of the dissipated heat rates, the RMSEs were divided by the peak dissipated heat rates to facilitate the interpretation of the results and were reported as percentages.

III.2 Simplified thermal model description

The thermal behaviour of LTO battery cells depends on several factors, determining the amount of heat generated within the cell volume and how it is partially dissipated in the environment. Certainly, the physical properties of the cell, such as density, specific heat, and thermal conductivity, contribute (Bryden *et al.*, 2018; Sheng, Su and Zhang, 2019). A higher specific heat means the battery can absorb more heat before its temperature rises due to an increase in thermal inertia (Sheng *et al.*, 2019). Density similarly contributes to this feature (Yang, Yan and Pak, 2023a). Instead, thermal conductivity determines how efficiently heat is transferred within the LTO cell and to its surroundings (Wei *et al.*, 2020). According to Yang et al. (Yang, Yan and Pak, 2023b), specific heat and density have the most influence in characterising the thermal behaviour of batteries instead of thermal conductivity.

Geometry is another model input that influences the convective heat transfer and the heat generation rate per volume. Shape and size impact the average temperature and the temperature field of the cell due to the surface area-to-volume ratio (Árpád, Kiss and Kocsis, 2024). According to Trinuruk et al. (Trinuruk *et al.*, 2023), different cell forms also directly impact internal heating generation due to their effect on the equivalent electric resistance. Regarding the heat transfer phenomenon inside the device, a larger volume at fixed thermal conductivity may affect the internal conductive resistance, limiting the heat dissipation to the environment (Jin Liu *et al.*, 2024).

Ambient conditions define the properties directly correlated to the natural convection. The environment impacts the dissipated heat rate over time due to the temperature difference between the external surface and the air or the convective heat transfer coefficient. According to Yang et al. (Yang *et al.*, 2020), when the convective heat transfer coefficient increases, the peak temperature region of the field is restricted and tends to be uniform. This consideration demonstrates how these parameters play an important role in the thermal behaviour of batteries.

Internal heat generation depends on the current discharge and charge profile. Several phenomena, such as ohmic loss, activation, and concentration losses, are principally responsible for the chemical energy decay stored in batteries (Maiorino *et al.*, 2024). There is a proportionality between the current intensity and the internal thermal energy generation over time (Du *et al.*, 2017). For this reason, a current profile is needed as input for the proposed model because it has a relevant impact on how heat is generated within the cell. Figure III.1 summarises the required inputs and outputs of the simplified thermal model. The model outputs are the average temperature trend over time, the temperature field, the heating generation rate, and the dissipated heat rate.

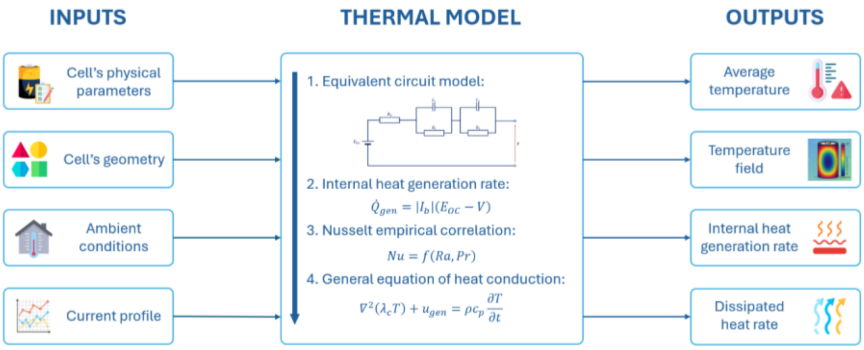

Figure III.1 *Schematic description of the simplified thermal model*

As represented by the central box in Figure III.1, the thermal model can be divided into four main parts:

1. *Equivalent Circuit Model*: It calculates the difference between the open circuit voltage E_{oc} and the real voltage V as a function of SOC.
2. *Heat generation rate*: The Bernardi et al. equation can be used to obtain the internal heat generation rate trend for that current profile. This parameter is the main cause of the temperature increment over time.
3. *Nusselt empirical correlation*: the Nusselt number's empirical correlations permit the estimation of the convective heat transfer coefficient h_{conv}. This parameter changes over time and follows a specific trend due to the dependence of the Rayleigh number on the cell's surface temperature.
4. *General equation of heat conduction*: supposing a uniform generation within the cell's volume and knowing its physical parameters, the general heat conduction equation achieves the temperature field. It is possible to determine its average value over time by integrating the temperature field over the cell's volume.

These steps will be discussed in detail after the description of the chosen reference Li-ion cell for the study.

III.2.1 Cylindrical Li-ion cell used for thermal analysis

The considered Li-ion cylindrical cell is a 1500 mAh 18650 LTO cell with a nominal voltage of 2.4 V. Other datasheet parameters are listed in Table III.1.

Table III.1 *Datasheet of the reference LTO 18650 cylindrical cell*

LTO 18650 cell datasheet			
Nominal voltage	2.4 V	Max charge current	15 A
Nominal capacity	1500 mAh	Standard discharge curve	1500 mAh
Charge cut-off voltage	2.8 V	Max discharge current	15 A
Discharge cut-off voltage	1.5 V	Battery weight	45 ± 5 g
Internal resistance	≤ 30 mΩ	Battery size	18 mm x 65 mm
Standard charge current	1500 mAh	Cycle times	> 20000 times

Thermal and physical parameters were recovered in the literature. Table III.2 summarises the constant parameters chosen for the analysis, which were also considered unchanged in each part of the cell's volume.

Table III.2 *Thermal parameters of the reference LTO 18650 cylindrical cell*

LTO 18650 cell thermal parameters	
Specific heat (c_p)	950 J·kg^{-1}K^{-1}
Axial thermal conductivity (λ_z)	14.7 W·m^{-1}K^{-1}
Radial thermal conductivity (λ_r)	1.5 W·m^{-1}K^{-1}
Density (ρ)	2703.8 kg·m^{-3}

According to Yu et al. (Yu *et al.*, 2023), the specific heat of an 18650 Li-ion cell typically assumes values between 884 J·kg^{-1}K^{-1} and 1016 J·kg^{-1}K^{-1}, while axial thermal conductivity assumes values between 12.6 W·m^{-1}K^{-1} and 16.7 W·m^{-1}K^{-1}. Radial thermal conductivity and density refer to the article written by Sheng et al. (Sheng *et al.*, 2021), in which their values are respectively equal to 1.5 W·m^{-1}K^{-1} and 2703.8 kg·m^{-3}. Regarding axial thermal conductivity and specific heat, their values were evaluated as the algebraic mean between the extremes of the definition intervals.

The geometry was defined considering the principal features of the LTO cell, such as round connections and electrodes. Figure III.2 represents the geometric model of the reference cell.

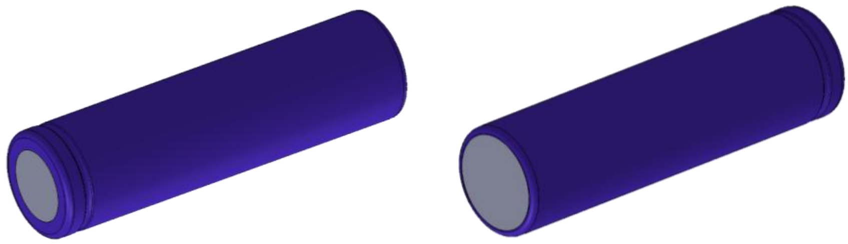

(a) (b)

Figure III.2 *Front (a) and back (b) views of the LTO 18650 cylindrical cell model*

Aluminium electrodes were implemented, considering their real bulk and schematising them as thin disks of 0.5 mm. Their diameters for the front and the back surfaces are 12 mm and 16 mm, respectively. In the thermal model, the electrodes are characterised by their own heat generation rate, separated by the Bernardi et al. equation (Bernardi, Pawlikowski and Newman, 1985).

III.2.2 Equivalent Circuit Model

The next step evaluates the difference between the open circuit voltage E_{oc} and the real voltage V. This value can be obtained using an Equivalent Circuit Model, such as the 2nd order Thevenin model. This approach permits achieving the optimal compromise between computational cost and reliability of the results. According to several studies published in the literature (Deng *et al.*, 2021; Shen *et al.*, 2021; Zhuang *et al.*, 2022; Bobobee *et al.*, 2023), the 2nd order Thevenin model is shown to be more accurate, stable, and robust compared to the 1st order RC model, but less computationally expensive than RC models of higher orders. The circuit's scheme is illustrated in Figure III.3.

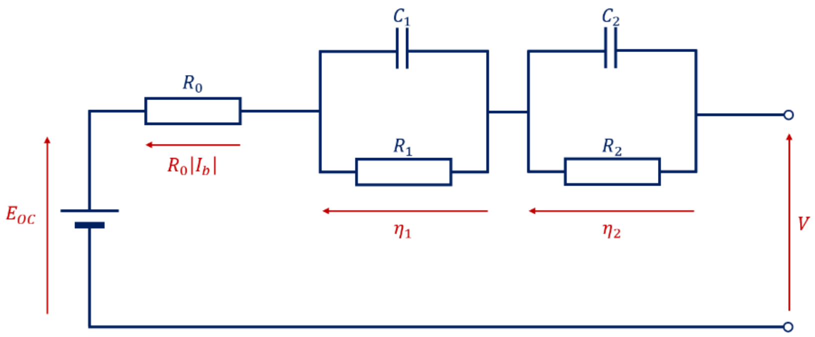

Figure III.3 *2nd order Thevenin model equivalent circuit*

The equivalent circuit's layout includes a voltage generator, a resistor, and two RC loops. Each component reflects a particular phenomenon occurring in a battery during the discharging and charging phases. While the open circuit voltage E_{oc} defines the voltage produced by a cell when no current flows in the circuit (Maiorino *et al.*, 2024), η_1 and η_2 represent the voltage drops caused by polarisation losses, typically associated with activation and concentration losses, respectively (Nikolian *et al.*, 2016). R_0 instead represents the ohmic losses of electrodes and terminals related to the Joule effect (Shen *et al.*, 2021).

These voltage drops can be calculated over time as reported from Formula (III.1) to Formula (III.3), applying the typical laws of circuit theory (B. H. Chen *et al.*, 2023).

$$\eta_0 = R_0|I| \tag{III.1}$$

$$\frac{d\eta_1}{dt} = -\frac{\eta_1}{R_1C_1} + \frac{|I|}{C_1} \tag{III.2}$$

$$\frac{d\eta_2}{dt} = -\frac{\eta_2}{R_2C_2} + \frac{|I|}{C_2} \tag{III.3}$$

I is the current intensity defined by any discharge and charge profile. Electric resistances and capacitances are evaluated through an experimental characterisation defined as Hybrid Power Pulse Characterisation (HPPC) (Zhang *et al.*, 2018). This procedure established the ECM of the reference LTO cylindrical by considering the dependence of these parameters on the SOC. Figure III.4 represents the results of resistances and capacitances as a function of State of Charge.

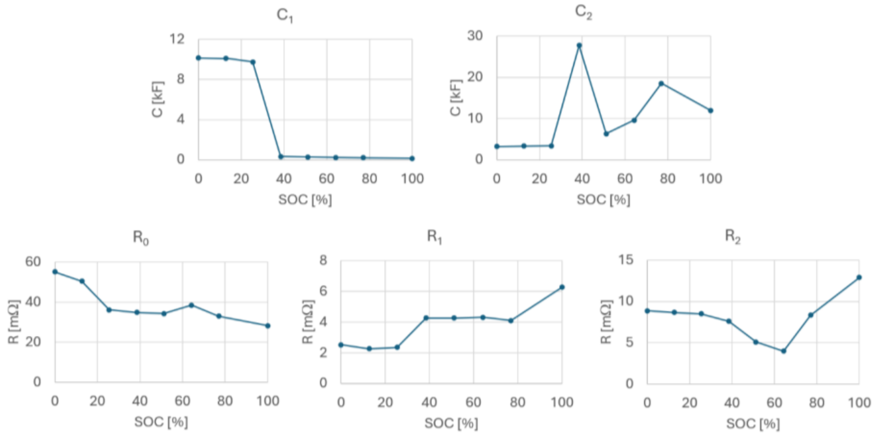

Figure III.4 *Equivalent circuit parameters obtained experimentally through HPPC*

By combining the input current profile, the formulas for the voltage drop, and the known ECM parameters as a function of SOC, the voltage drops of the resistor R_0 and the two RC loops can be calculated. As shown by Formula (III.4), it is possible to obtain the difference between E_{oc} and V indirectly through Kirchhoff's Voltage Law.

$$E_{oc} - V = R_0|I| + \sum_{i=1}^{2} \eta_i \tag{III.4}$$

III.2.3 Heat generation rate

Once the difference between the open circuit voltage and the terminal voltage of the cell is estimated over time, this data is used to calculate the heat generation rate. The heat generated by a battery cell is generally subdivided into two contributions, which consider the irreversible and reversible phenomena that occur in the device (Zhang *et al.*, 2023a). The first term is irreversible heat related to ohmic and polarisation losses. The second term is reversible heat produced by the variation of the chemical reaction's intercalation entropy within the electrodes (Zhang *et al.*, 2023a). Bernardi et al. (Bernardi, Pawlikowski and Newman, 1985) explicated these contributions, obtaining their equation represented as Formula (III.5) and detailed by Formulas (III.6) and (3.7).

$$\dot{Q}_{gen} = |I| \left[(E_{oc} - V) - \bar{T} \frac{\partial E_{oc}}{\partial \bar{T}} \right] \tag{III.5}$$

$$\dot{Q}_{irr} = |I| \cdot (E_{oc} - V) \tag{III.6}$$

$$\dot{Q}_{rev} = -|I| \cdot \bar{T} \frac{\partial E_{oc}}{\partial \bar{T}} \tag{III.7}$$

Due to the reversibility of the reactions in the electrodes, the intercalation entropy variation can be negative or positive, depending on the working conditions of the cell (Reynier *et al.*, 2004a; Viswanathan *et al.*, 2010). This means the reversible heat contribution can be negative or positive, depending on whether the redox reaction is exothermic or endothermic. This feature is well described by Formula (III.8), which can be considered true if the hypothesis of almost stationary chemical conditions is accepted (Reynier *et al.*, 2004b).

$$\frac{\partial E_{OC}}{\partial \bar{T}} = \frac{\Delta S_{rev}}{nF} \tag{III.8}$$

ΔS_{rev} is the entropy variation of the chemical species participating in the redox reaction.

According to Formula (III.5), the LTO cell's total internal heat generation rate depends on its average temperature. This means the calculator should determine the cell's mean temperature and then use this information to estimate the total heat generation for the next timestep. A simplifying hypothesis neglects reversible heat generation, but it can be applied only in particular cases. Several articles in the literature (Heubner, Schneider and Michaelis, 2016; Spitthoff *et al.*, 2023; Zhang *et al.*, 2023a) report that this contribution can be significant at low C_{rate} and high temperatures, such as 0.5C and 30 °C. Shao et al. (Shao *et al.*, 2023) proposed an in-depth study of how the reversible heat affects the total heat generation rate at 25 °C, and for two C_{rates} values equal to 0.1C and 1C. According to the results, Li-ion batteries exhibit exothermic heat throughout charge and discharge due to a relatively small proportion of reversible heat at 1C. It makes the negligibility of reversible heat a practicable hypothesis for the proposed analysis.

Formula (III.5), combined with Formula (III.3) and the neglect of the reversible heat contribution, defines the total heat generation rate used in the simplified thermal model. This is reported as Formula (III.9).

$$\dot{Q}_{gen} = |I| \left(R_0 |I| + \sum_{i=1}^{2} \eta_i \right) \tag{III.9}$$

The heat generation rate of electrodes must be evaluated differently because only ohmic losses occur. It can be determined both for the anode and the cathode by applying the second Ohm's Law, considering a current flow parallel to the LTO cell's axis. This is summarised by Formula (III.10).

$$\dot{Q}_{el,i} = \frac{1}{\sigma_{alu}} \frac{th_{el}}{\pi\left(\frac{{D_i}^2}{4}\right)} I^2 \qquad for\ i = anode, cathode \tag{III.10}$$

III.2.4 Nusselt empirical correlation

The next step is the estimation of the convective heat transfer coefficient h_{conv} using experimental correlations. This parameter depends on the temperature difference between the hot surface of the cell and the environment (Cengel, 2022). The convective heat transfer coefficient is assumed constant across the entire heat exchange area to reduce the model's complexity. The following correlations refer to a horizontal cylinder due to the cell's shape and positioning. This choice was made due to the plastic battery holder shape, which is projected to hold the battery cell on a horizontal surface.

The convective heat transfer coefficient was estimated using the Nusselt number. Calculation of the Rayleigh and the Prandtl numbers, respectively Ra_{air} and Pr_{air}, is necessary for utilising empirical correlations. The Rayleigh number was calculated as reported in Formula (III.11) (Rohsenow, Hartnett and Cho, 1998).

$$Ra_{air} = \frac{g\beta\left(\bar{T}_{sup} - T_{\infty}\right)D^3}{{\nu_{air}}^2} Pr_{air} \tag{III.11}$$

It depends on the coefficient of volume expansion β, the free-stream temperature T_{∞}, the characteristic length of the convection problem, the kinematic viscosity ν_{air}, and the Prandtl number. For this analysis, the characteristic length coincides with the cell's diameter. The surface temperature in Formula (III.12) is generally defined as a generic temperature of the surface. Instead, the simplified thermal model considers it the average temperature across the exposed surface over time. The thermal properties in Formula (III.11) vary, depending on the film temperature T_{film}. Considering the assumption of the average value of the surface temperature field, this parameter is calculated as reported by Formula (III.12) (Rohsenow, Hartnett and Cho, 1998).

$$T_{film} = \frac{\bar{T}_{sup} + T_{\infty}}{2} \tag{III.12}$$

Due to surface temperature variability over time, the Rayleigh number assumes different values depending on the physical properties of the air and the temperature difference between the cell and the environment. Consequently, the convective heat transfer coefficient varies in time due to the dependence of the Nusselt number on the Rayleigh number, as summarised by Formula (III.13). The thermal conductivity of air is represented as λ_{air}.

$$h_{conv} = \frac{Nu_{air}\ \lambda_{air}}{D} \tag{III.13}$$

As reported in the literature (Yesiloz and Aydin, 2013; Mahian *et al.*, 2016), this approach inevitably leads to a certain error when estimating the convective heat transfer coefficient due to an underestimated or overestimated value of the Nusselt number. For this reason, the thermal analysis of the reference cylindrical cell was made considering three different correlations for horizontal cylinders in natural convection. Formulas (III.14), (III.15), and (III.16) report the Nusselt correlations proposed by Churchill and Chu (Churchill and Chu, 1975), Morgan (Morgan, 1975), and Kuehn and Goldstein (Kuehn and Goldstein, 1976).

$$Nu_{air} = \left\{ 0.6 + \frac{0.387 \cdot {Ra_{air}}^{\frac{1}{6}}}{\left[1 + (0.559/Pr_{air})^{\frac{9}{16}}\right]^{\frac{8}{27}}} \right\}^2 \quad for\ Ra_{air} \leq 10^{12} \tag{III.14}$$

$$Nu_{air} = \begin{cases} 1.02 \cdot {Ra_{air}}^{0.148} & for\ Ra_{air} \leq 10^2 \\ 0.85 \cdot {Ra_{air}}^{0.188} & for\ 10^2 < Ra \leq 10^4 \end{cases} \tag{III.15}$$

$$\frac{2}{Nu_{air}} = ln\left[1 + \frac{2}{\left[\left\{0.518 \cdot Ra_{air}{}^{\frac{1}{4}}\left[1 + \left(\frac{0.559}{Pr_{air}}\right)^{\frac{3}{5}}\right]^{-\frac{5}{2}}\right\}^{15} + \left(0.1 \cdot Ra_{air}{}^{\frac{1}{3}}\right)^{15}\right]^{\frac{1}{15}}}\right] \qquad \text{(III.16)}$$

III.2.5 General equation of heat conduction

The final step is to collect all the previous information in the general heat conduction equation. Due to the cylindrical geometry of the LTO cell, the equation can be expressed using cylindrical coordinates *r*, *φ*, *z* as shown by Formula (III.17).

$$\lambda_r \left[\frac{1}{r}\frac{\partial}{\partial r}\left(r\frac{\partial T}{\partial r}\right) + \frac{\partial^2 T}{\partial \varphi^2}\right] + \lambda_z \frac{\partial^2 T}{\partial z^2} + u_{gen} = \rho c_p \frac{\partial T}{\partial t} \qquad \text{(III.17)}$$

Considering uniform internal heat generation in the cell, the known term of Formula (III.17) can be calculated by dividing the heat generation rate by the cell's volume *Vol*. In accordance with Bernardi et al. (Bernardi, Pawlikowski and Newman, 1985) equation, the expression of u_{gen} is reported in Formula (III.18).

$$u_{gen} = \frac{|I|}{Vol}\left(R_0|I| + \sum_{i=1}^{2} \eta_i\right) \qquad \text{(III.18)}$$

The heat generation rate per unit volume in the electrodes is determined identically using Formula (III.10) instead of Formula (III.9).

The boundary conditions were imposed considering the convective heat exchange between the LTO cell and the environment. The bottom, the top and lateral surfaces of the cell are considered adiabatic to emulate the thermal resistance provoked by the battery holder, which is in direct contact with them. Formulas (III.19), (III.20), and (III.21) define Robin's boundary conditions implementing the convective heat transfer coefficient h_{conv}.

$$\lambda_r \frac{\partial T}{\partial r}\bigg|_{r=R} = \begin{cases} h_{conv}(T(R,\varphi,z,t) - T_\infty) & for\ 0 \leq \varphi \leq \pi \\ 0 & for\ \pi < \varphi < 2\pi \end{cases} \tag{III.19}$$

$$\lambda_z \frac{\partial T}{\partial z}\bigg|_{z=0} = 0 \tag{III.20}$$

$$\lambda_z \frac{\partial T}{\partial z}\bigg|_{z=L_{LTO}} = 0 \tag{III.21}$$

The simulations emulate real conditions where the LTO cell and environment are initially in thermodynamic equilibrium. This condition is represented by Formula (III.23).

$$T(r,\varphi,z,0) = T_\infty \tag{III.23}$$

Finally, the dissipated heat rate can be calculated step by step by integrating the normal heat flux flowing through the exposed surface as indicated in Formula (III.24).

$$\dot{Q}_{conv} = \iint_A h_{conv}(T(R,\varphi,z,t) - T_\infty)\, dA \tag{III.24}$$

III.3 Simplified thermal model results

The research proposes two distinct input current profiles that emulate typical discharging and charging conditions of a commercial 1500 mAh LTO cell. The first one regards a continuous discharge test, which is characterised by this procedure:

1. A constant discharge at 1C lasting 140 s.
2. Null current for 38 s.
3. 10 charging cycles formed by a 1C charge for 15 s and null current part lasting 15 s.

The continuous discharge current profile is represented in Figure III.5.

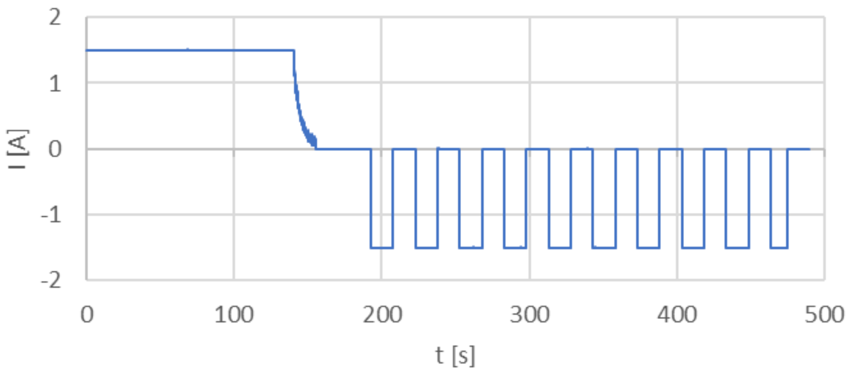

Figure III.5 *Continuous discharge test current profile*

The second concerns a partial discharge test, which develops similarly to the previous one at the initial discharge but differs in the repeated charge and discharge cycles. The procedure follows these steps:

1. A constant discharge at 1C lasting 165 s.
2. Null current for 38 s.
3. 10 charging and discharging cycles formed by two 1C charging lasting 15 s, interrupted by 15 s of null current, and a 1C discharge of 15 s.

Figure III.6 exhibits the partial discharge current profile.

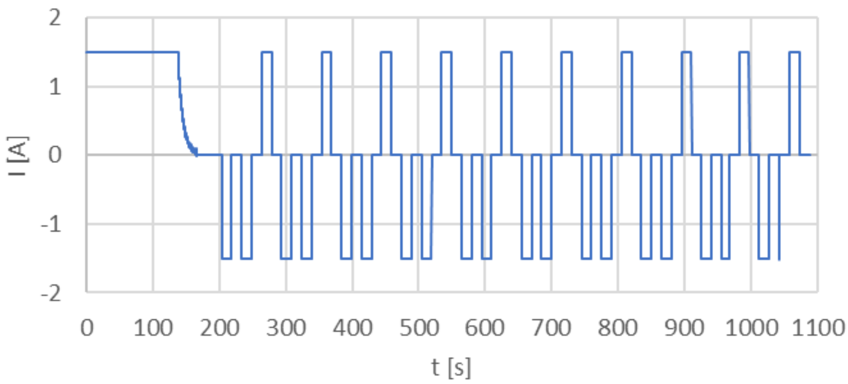

Figure III.6 *Partial discharge test current profile*

Ambient conditions are another fundamental aspect to consider. To ensure a direct comparison between the numerical and experimental analyses, the simulations for continuous and partial discharge tests were run using the actual ambient temperatures measured in the laboratory. This was possible due to the sequential nature of the workflow, where experimental data were collected before the numerical simulations. In agreement with the measurements, the ambient temperatures were assumed to be 21.8 °C and 21.0 °C for the continuous and the partial discharge, respectively.

Due to the symmetric boundary conditions and geometry, only a half-cylindrical cell was considered, further reducing the computational cost of the thermal model. As represented in Figure III.7, the symmetry manifests along the cell's axis.

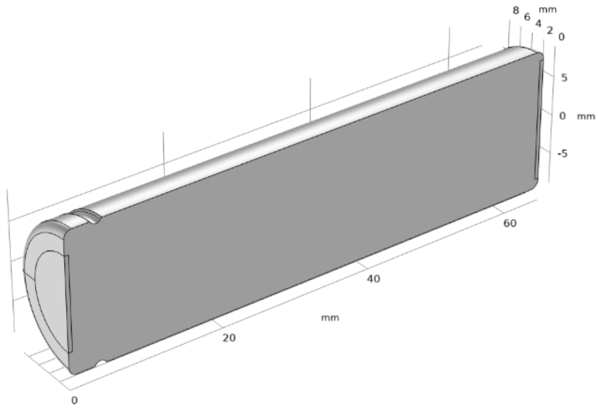

Figure III.7 *Half LTO cell geometry model used for the simulations*

III.3.1 Grid convergence and timestep independence

A grid convergence analysis and the timestep study were conducted to achieve the optimal compromise between accuracy and computational costs. There is no standardised procedure for these tests, and it mostly depends on the researcher's experience and knowledge (Lee *et al.*, 2020). It has been decided to compare the average temperature difference between the mean cell and the ambient temperature over time. This approach analysed the grid convergence and the timestep independence by considering one representative value for each simulation. The percentage error between simulations was evaluated by Formula (III.25), while Formula (III.26) calculates the mean temperature difference.

$$err_{\%} = \left| \frac{\overline{\Delta T}_i - \overline{\Delta T}_{fine}}{\overline{\Delta T}_{fine}} \right| \cdot 100 \tag{III.25}$$

$$\overline{\Delta T} = \frac{1}{\Delta t} \int_0^{t_{end}} (\bar{T} - T_\infty)\, dt \tag{III.26}$$

The grid was optimised when the percentage error between the selected and the finest mesh reached values below 2%. The same condition is applied to the timestep analysis.

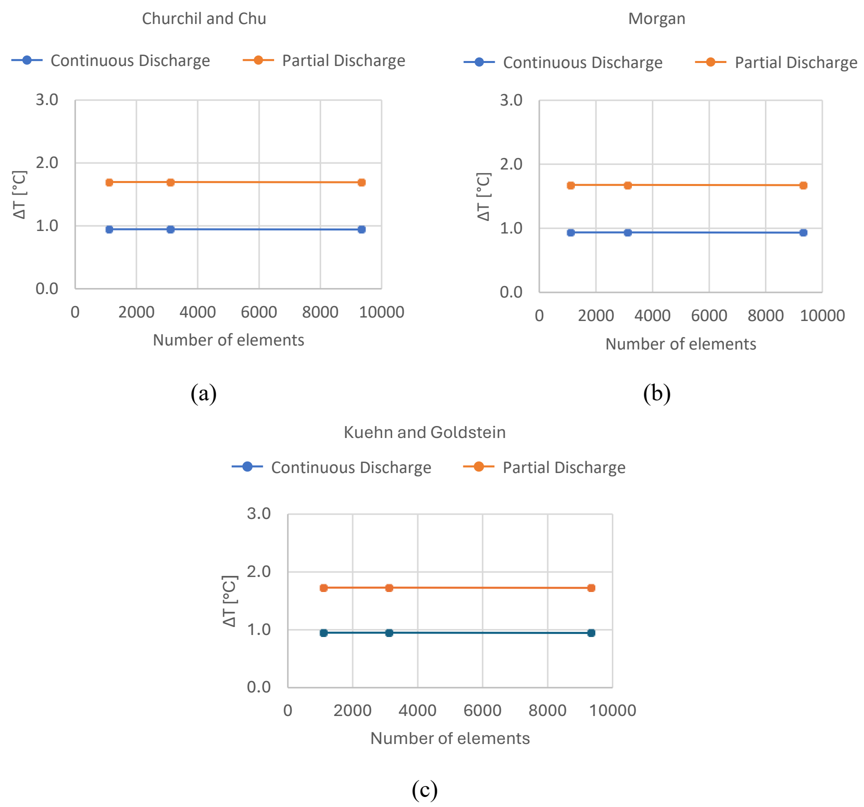

Figure III.8 *Grid convergence analysis results*

As represented in Figure III.8, the grid convergence analysis considered three different meshes formed by 1097, 3110, and 9332 elements. A constant timestep of 2 seconds was set for each simulation. According to the results, the mesh formed by 1097 elements reached the grid convergence condition for continuous and partial discharges. The analysis was made considering different Nusselt number correlations as described previously. Despite Formulas (III.14), (III.15), and (III.16) being different, they did not significantly influence the mesh thickness investigation. The uniformity of the temperature field explained this outcome. As described in the next paragraphs, the temperature gradients within the cell were almost null, meaning the thermal problem did not require a dense grid.

The timestep independence study allowed for the best transient solution resolution by implementing the coarse grid. By observing how charging and discharging cycles last in every test, three timesteps were considered: 2 s, 1 s, and 0.5 s. The results showed that the thermal problem was independent of the timestep. This feature may be explained by the thermal inertia of the cell, which produced slow temperature changes. This means a wide timestep of 2 s did not affect the accuracy of the solution. Figure III.9 represents the results of the timestep independence study.

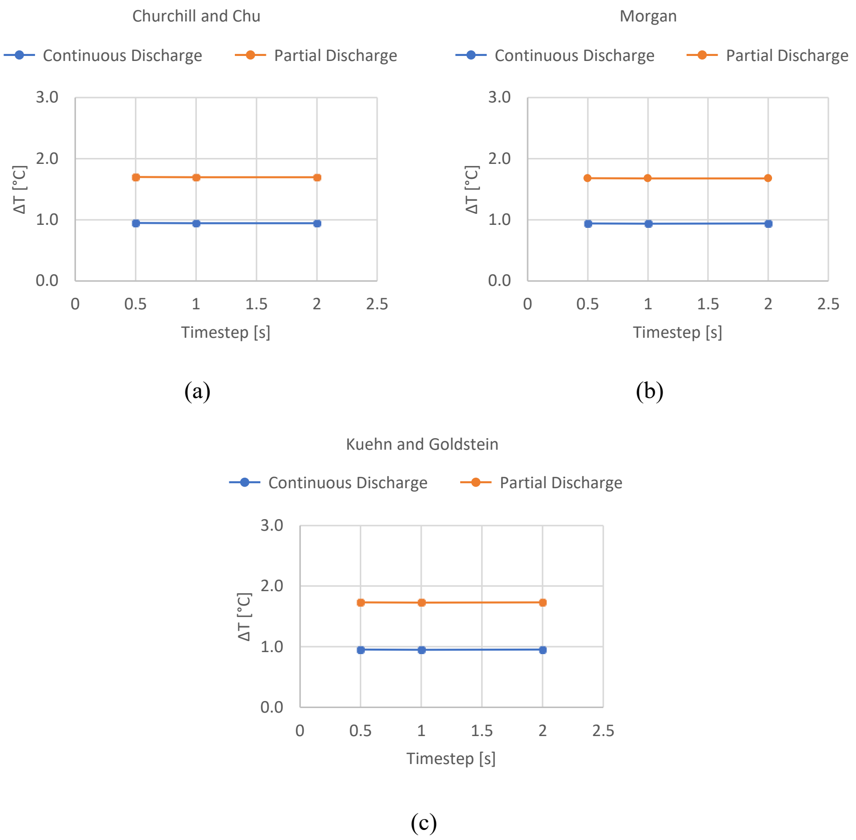

Figure III.9 *Timestep independence analysis results*

III.3.2 Analysis of the results

The results will be presented in steps defined previously. The heat generation ratio depends on the current intensity and the ECM's electrical parameters. As represented in Figure III.10, the heat generation rate trends retraced the current profiles. The peaks remained almost constant, indicating that the SOC influence on the voltage drops of the ECM is substantially limited.

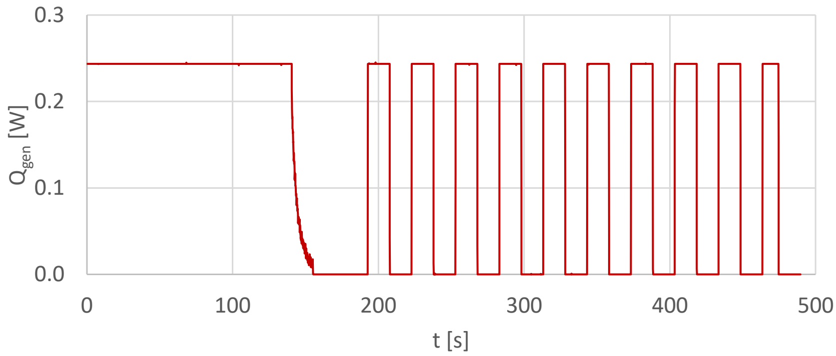

(a)

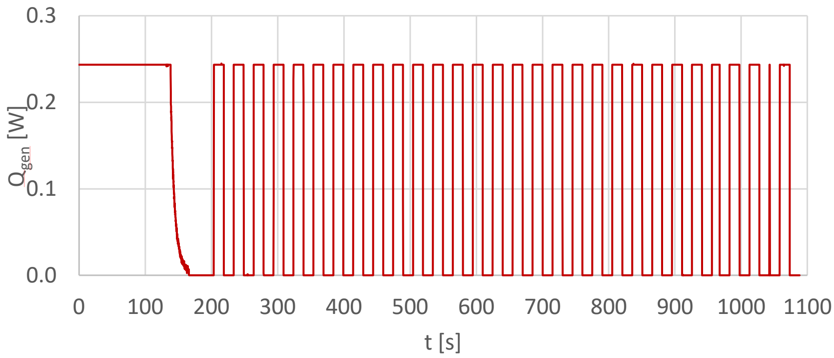

(b)

Figure III.10 *Internal heat generation rates for continuous (a) and partial (b) discharges*

The peak in both tests was equal to 0.240 W. Instead, the dissipated heat ratio increased over time due to the convective heat transfer coefficient growth. Initially, no heat was dissipated in the ambient because natural convection was not activated yet due to the infinitesimal difference between the cell's surface and the surrounding air temperatures. At the end of the continuous discharge test, the dissipated heat rates were equal to 0.005 W, 0.006 W, and 0.004 W, corresponding to the Churchill and Chu, the Morgan, and the Kuehn and Goldstein correlations. Due to the higher difference between the cell's surface temperature and the environment, these peaks were equal to 0.011 W, 0.013 W, and 0.008 W at the end of the partial discharge test. Instead, the electrodes generated an irrelevant amount of heat to the cell because its ratio assumes values lower than 10^{-3} W.

The average temperature had a growing trend over time. As described previously, an initial equilibrium condition between the ambient and the

LTO cell was considered for both tests, as evident in Figure III.11. For these current profiles, there were no dangerous phenomena related to thermal abuse because the peak temperatures reached values within the optimal range between 15 °C and 35 °C. There was one zone where the temperature did not rise, corresponding to a section with a null current profile. Figure III.11 represents several temperature trends, classified by the Nusselt number correlation.

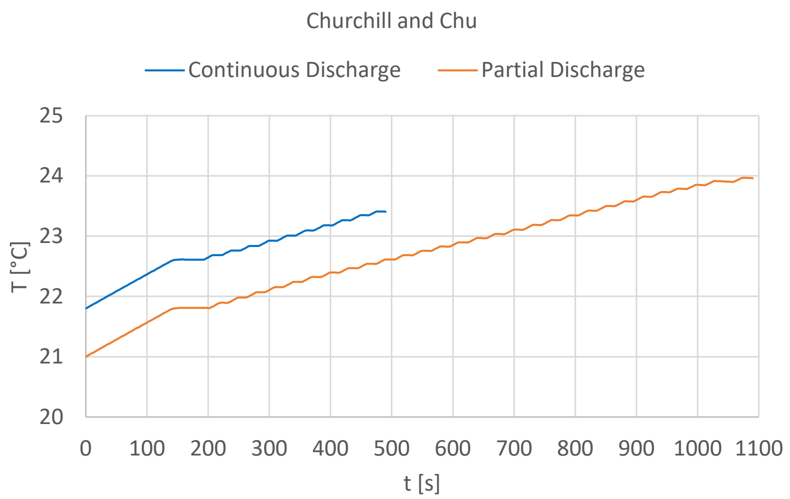

(a)

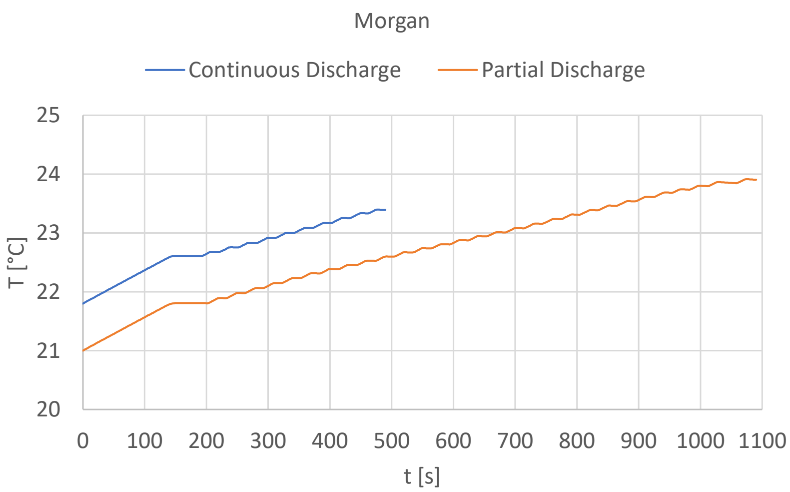

(b)

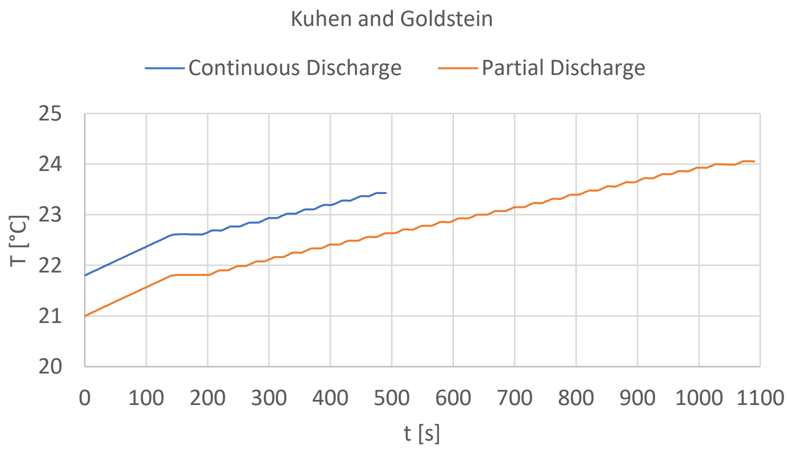

(c)

Figure III.11 *Average temperatures corresponding to Churchill and Chu (a), Morgan (b), and Kuehn and Goldstein (c) correlations*

Ending temperatures of the continuous discharge equal 23.4 °C for all the simulations, while they assume values of 24.0 °C, 23.9 °C, and 24.1 °C for the Churchill and Chu, Morgan, and Kuehn and Goldstein formulas.

The temperature field was uniform in all the cases because the maximum temperature difference over time did not exceed 0.1 °C. The LTO cylindrical cell size, geometry, and the Biot number explain this behaviour. The Biot number represents the ratio between the internal conductive resistance and the external convective resistance (El Diasty, Faziot and Budaiwlj, 1993) and is evaluated along the radius direction as Formula (III.27).

$$Bi_r = \frac{h_{conv} D}{\lambda_r} \qquad \text{(III.27)}$$

Parameters h_{conv} and λ_r were characterised by the same order of magnitude, while the diameter of the cell measured 18 mm. Biot number had an order of magnitude of 10^{-2}, indicating the internal conductive resistance was certainly lower than the convective due to the reduced size of the Li-ion cell. The greater obstacle to heat dissipation was the convective heat exchange, while within the cell's volume, there was no opposition to overcome. Figure III.12 represents the cell's contour for four different time instants of the continuous discharge simulation, referring to the Morgan correlation. Similar results were obtained for the partial discharge test and applying the other Nusselt correlations.

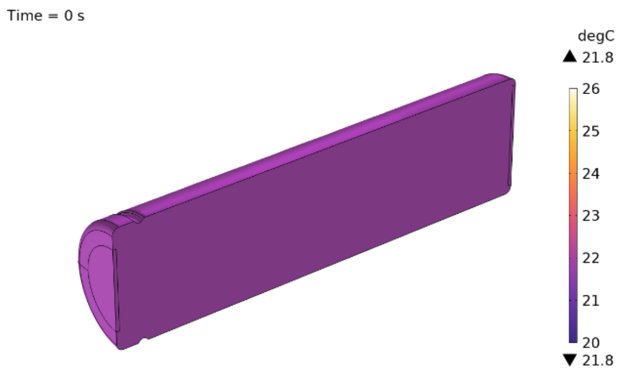
Time = 0 s
degC
▲ 21.8
26
25
24
23
22
21
20
▼ 21.8

(a)

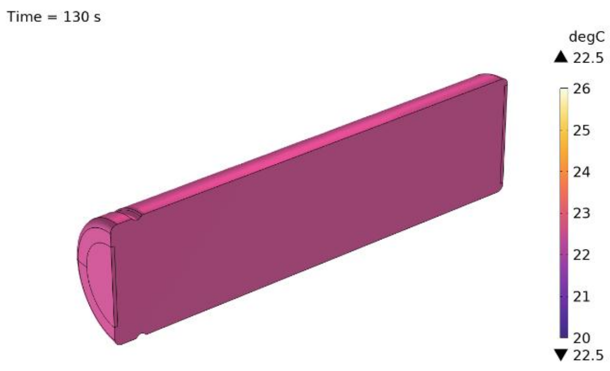
Time = 130 s
degC
▲ 22.5
26
25
24
23
22
21
20
▼ 22.5

(b)

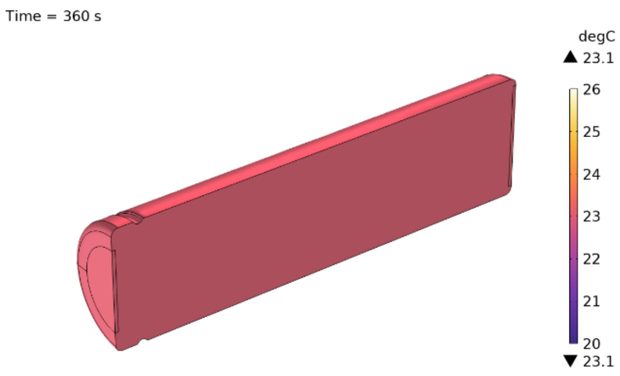
Time = 360 s
degC
▲ 23.1
26
25
24
23
22
21
20
▼ 23.1

(c)

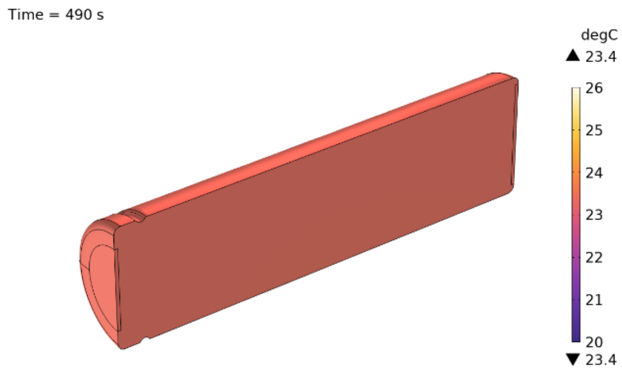

(d)

Figure III.12 *Contours of the LTO cell at 0 s (a), 130 s (b), 360 s (c), and 490 s (d) referred to the continuous discharge*

The convective heat transfer coefficient assumed different values depending on which correlation was used as the boundary condition parameter. As represented by Figure III.13, there is a relevant difference when comparing Formulas (III.15), (III.16), and (III.17). Despite differing in most parts of the tests, the results shared the same trend over time. The higher growth manifested at the beginning of both tests due to a rapid increase of the Rayleigh number in proportion to the temperature difference between the exposed surface and the environment. After a constant trend corresponding to the null current section, the h_{conv} increased more slowly due to the intermittence of the heat generation rate until the maximum value is reached.

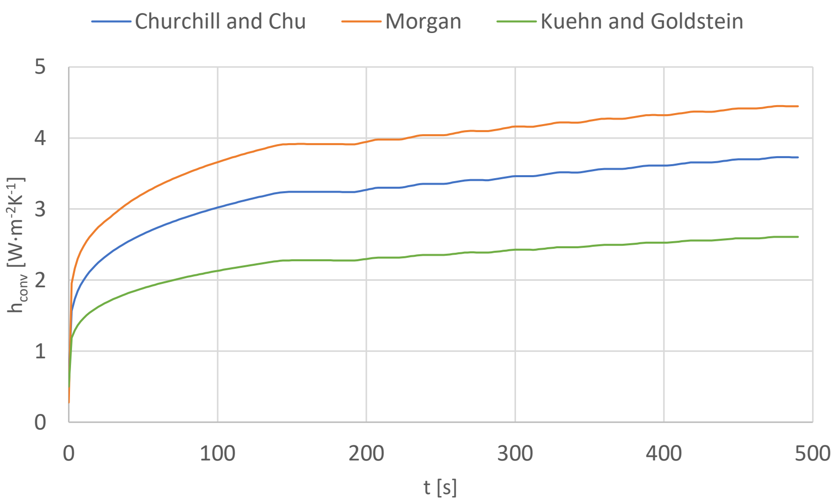

(a)

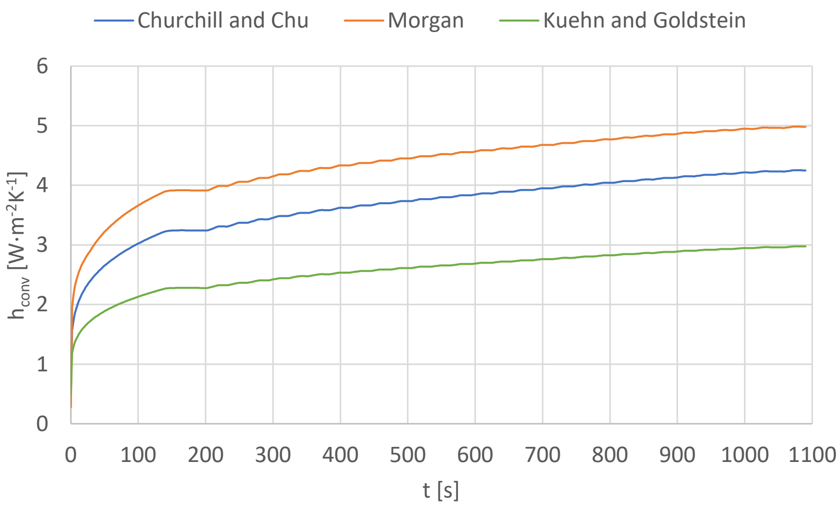

(b)

Figure III.13 *Convective heat transfer coefficient comparison for continuous (a) and partial (b) discharges*

Morgan correlations estimated the highest convective heat transfer coefficient to 4.4 W·m^{-2}K^{-1} and 5.0 W·m^{-2}K^{-1} for continuous and partial discharge. The Kuehn and Goldstein correlation returned the lowest coefficients, respectively equal to 2.6 W·m^{-2}K^{-1} and 3.0 W·m^{-2}K^{-1}, corresponding to –41% and –40% compared to the previous values. The formula proposed by Churchill and Chu achieved values between them in every step of the simulations, obtaining values equal to 3.7 W·m^{-2}K^{-1} and 4.3 W·m^{-2}K^{-1}.

III.3.3 Simplified thermal model experimental validation

The results were experimentally validated using the real cylindrical 18650 LTO cell represented in Figure III.14.

Figure III.14 *Real reference 1500 mAh LTO cell*

The black plastic object surrounding the cell is the battery holder made in ABS. Temperature measurements were done using a thermal camera whose accuracy was ±1.5 °C. Electric current was controlled by a battery cycler whose accuracy was <0.02% of the full scale, equal to 324 A. Figure III.15 shows the four temperature measurements for each discharge test and their corresponding time instant.

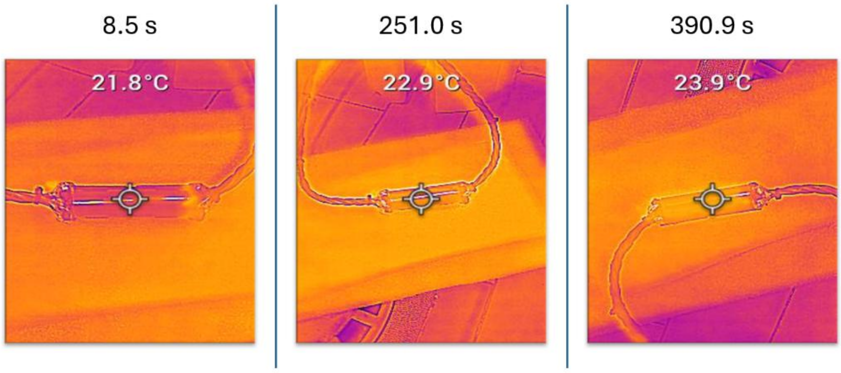

(a)

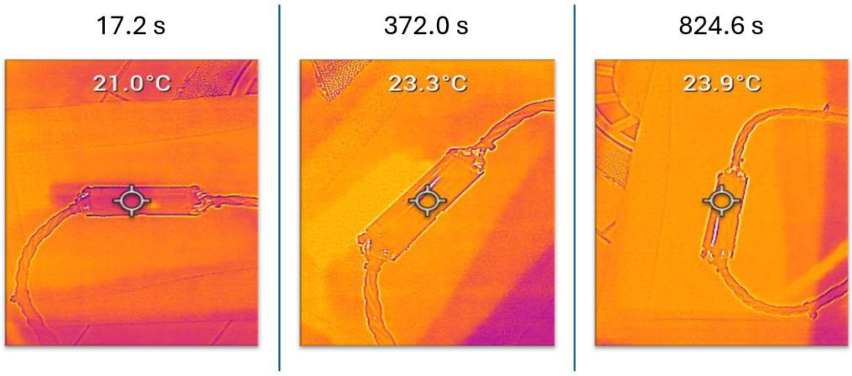

(b)

Figure III.15 *Temperature measurements for continuous (a) and partial (b) discharge tests*

Formula (III.28) expresses the percentage error ε_{exp} at the generic fixed time instant $\bar{t}$ between experimental and numerical results.

$$err_{\%,exp} = \frac{T_{exp}(\bar{t}) - \bar{T}(\bar{t})}{T_{exp}(\bar{t})} \cdot 100 \qquad \text{(III.28)}$$

As reported in Table III.3, the simplified thermal model achieved percentage errors within ±5%, demonstrating congruence between model and experimental results.

Table III.3 *Experimental percentage errors between temperature measurements and model outcomes*

CONTINUOUS DISCHARGE				PARTIAL DISCHARGE			
T_{exp} [°C]	Churchill and Chu	Morgan	Kuehn and Goldstein	T_{exp} [°C]	Churchill and Chu	Morgan	Kuehn and Goldstein
21.8	+0.2%	+0.2%	+0.2%	21.0	+0.5%	+0.5%	+0.5%
22.9	–0.6%	–0.6%	–0.6%	23.3	–4.2%	–4.2%	–4.1%
23.9	–3.0%	–3.1%	–3.0%	23.9	–2.0%	–2.1%	–1.8%

The results demonstrate a good correspondence between the simplified thermal model and the temperature measurements. The average temperature did not particularly differ when distinct Nusselt number correlations were applied. This is demonstrated by the almost identical percentage errors between model and temperature measurements reported in Table III.3.

The coefficient of correlation R^2 describes how the average temperature trends fit the temperature measurements. This approach gives a general perspective of the experimental validation without focusing exclusively on one-shot values. It is calculated as shown by Formula (III.29), while Formulas (III.30) and (III.31) describe the main terms.

$$R^2 = 1 - \frac{SSE}{SST} \tag{III.29}$$

$$SSE = \sum_{i=1}^{4} \left(T_{exp,i} - \bar{T}_i\right)^2 \tag{III.30}$$

$$SST = \sum_{i=1}^{4} \left(T_{exp,i} - \bar{T}_{exp}\right)^2 \tag{III.31}$$

The symbol $\bar{T}_{exp}$ indicates the mean value of the experimental temperature measurements. The different Nusselt correlations influence the R^2, obtaining the values reported in Table III.4.

Table III.4 *Coefficients of correlation for the continuous and the partial discharge*

COEFFICIENTS OF CORRELATION		
	Continuous discharge	**Partial discharge**
Churchill and Chu	98.3%	95.6%
Morgan	98.3%	95.8%
Kuehn and Goldstein	98.4%	95.4%

The results showed excellent agreement between the simplified thermal model and the temperature measurements. The continuous discharge achieved the best results, with an R^2 of 98.3% for the Churchill and Chu and the Morgan formulas, while the Kuehn and Goldstein correlation achieved 98.4%. The partial discharge test had the lowest correlation coefficients, but all simulations produced values above 95%. The Morgan expression had the highest R^2, but the differences among them are so small that all the correlations can be considered reliable.

III.4 Optimal choice of the Nusselt correlation using CFD

To handle the complex geometries and coupled physics involved in this study, the commercial FEM software COMSOL Multiphysics was selected. Indeed, although the simplified thermal model is a reliable procedure for estimating the thermal behaviour of the LTO cell without implementing complex equations, several considerations are necessary to achieve higher precision. Then the battery holder effects were implemented by considering the adiabatic hypothesis of the bottom and lateral surfaces of the LTO cell, but further study should confirm it. Nevertheless, the real exposed heat exchange area was lower due to the irregular shape of the plastic support. Finally, the Nusselt correlations referred to a horizontal cylinder in natural convection, which can be an unsophisticated hypothesis under certain conditions. The experimental validation demonstrates that the fundamental equations of the simplified thermal model are reliable and can effectively reproduce the thermal behaviour of an 18650 LTO cylindrical cell in natural convection. However, the procedure did not provide enough information to understand which Nusselt correlation is more suitable for this application due to the thermal camera accuracy. Indeed, as reported in the previous paragraph, the LTO cell temperature was measured at a single point on the external surface over time, but each measurement is affected by ±1.5 °C. This uncertainty could be reflected in the dissipated heat rate in further analysis, as suggested by Formula (III.24), because measurements cannot guarantee precision to a hundredth of Watts.

Computational Fluid-Dynamics (CFD) occurs by directly operating on the main issue cause. Modelling the velocity and temperature fields of the environment using the Navier-Stokes equations permitted avoiding all the dependences of the results on the empirical correlations, especially considering the dissipated heat rate over time. While the simplified thermal model calculated this output afterwards using the convective heat transfer coefficient, the CFD model integrates the heat flux field over the exposed surface. This approach is explicated in Formula (III.32).

$$\dot{Q}_{CFD} = \iint_A -\lambda_{air} \frac{\partial T}{\partial r} \, dA \tag{III.32}$$

This approach is more effective than the previous one because it bypasses measurement hardware drawbacks related to the thermal camera accuracy. As Formula (III.32) suggests, the three-dimensional temperature field of air proximate to the LTO cell surface provides the dissipated heat rate according to CFD analysis. Although it is an indirect method, the convective heat rate estimation is more accurate.

To implement the effects of the plastic support on the dissipated thermal energy through boundaries, the shapes and geometry were improved, emulating the real LTO cell and its ABS battery holder represented in Figure III.14. A surrounding volume of air permits applying the Navier-Stokes equation and inserting the buoyancy effects caused by local density gradients. The new geometry is represented in Figure III.16.

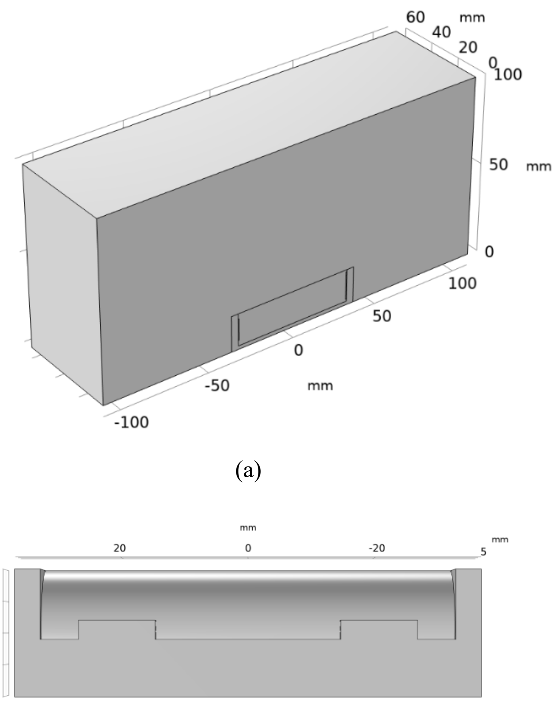

(a)

(b)

Figure III.16 *Geometry model for the CFD analysis (a) and particularisation of the battery holder (b)*

As in the previous case, the symmetry in boundary conditions and geometries permitted modelling a half-cell and half-battery holder. This expedient allowed the reduction of the computational cost that inevitably increased due to the Navier-Stokes equations.

III.4.1 Grid convergence and timestep independence

Grid convergence and timestep independence were developed to achieve the best compromise between precision and computational cost. However, the analysis did not compare the percentage error on the average temperature difference between cell and environment but considered the dissipated thermal energy on the top half-surface. It is a unique and global parameter for each simulation because it was estimated by integrating the dissipated heat rate, which deeply depends on the mesh thickness.

The dissipated thermal energy through the top half-surface of the cell is determined by integrating the corresponding heat rate, as indicated by Formula (III.33). Formula (III.34) expresses the percentage error evaluated between each mesh or timestep to proceed with the analysis.

$$E_{dis} = \int_{0}^{t_{end}} \dot{Q}_{conv}(t)\ dt \tag{III.33}$$

$$err_{\%} = \left| \frac{E_{dis,i} - E_{dis,fine}}{E_{dis,fine}} \right| \cdot 100 \tag{III.34}$$

The grid convergence analysis was developed considering four different meshes formed by 71783, 189340, 293077, and 614688 elements. Each simulation was performed imposing a constant timestep equal to 2 s. According to the results, the mesh formed by 293077 elements reached convergence. Compared to the simplified thermal model, the coarser mesh could not properly detect the thermal energy dissipated in the ambient because it depends on the temperature field surrounding the cell. A tight grid was necessary to analyse properly the air velocity field close to the cell's surface, as demonstrated by Figure III.17 (a).

A timestep independence study was performed considering the same timestep of the simplified thermal model, because the rapidity of the phenomenon should be independent of the model itself. The analysis was made by implementing the optimal mesh found by the grid convergence study. The timestep of 1 s achieved percentage errors below 2% for both tests. The results are reported in Figure III.17 (b).

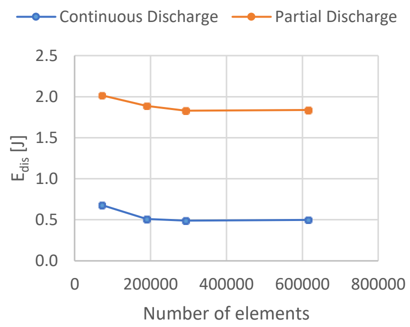

(a)

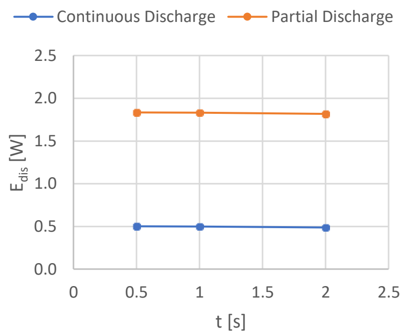

(b)

Figure III.17 *Results of the grid convergence (a) and timestep independence (b) analysis*

III.4.2 Analysis of the results

The CFD analysis aimed to improve the convective heat transfer modelling. This analysis did not influence the heat generation trends, SOC, and voltage drops of the ECM. The updated results concern exclusively the average temperature trends over time and the temperature contours, which include the thermal boundary layer surrounding the cell and its battery holder.

Figure III.18 represents the results for both discharge tests. The curves were almost identical to the previous case, but several differences occurred. The first part of the graph replicated identically the simplified thermal model for both tests until the null current section ended.

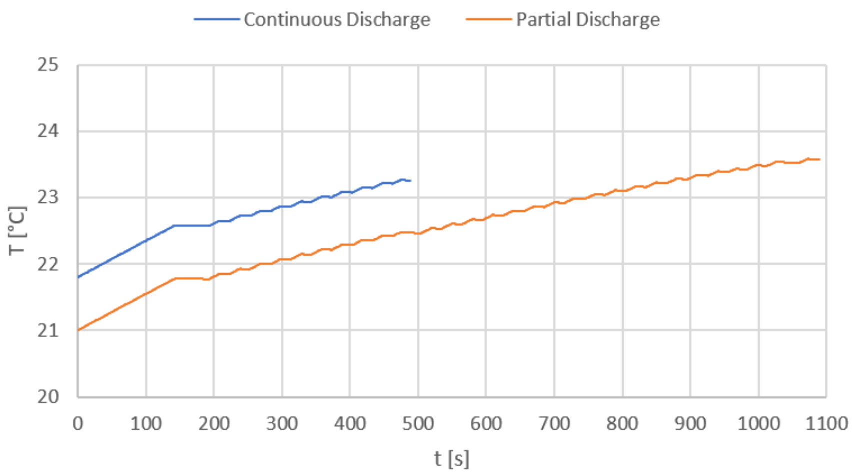

Figure III.18 *Average temperature trends obtained by the CFD analysis*

While the simplified model reached peak temperatures of about 24 °C at the end of the partial discharge tests, the CFD model reached a lower maximum of 23.6 °C. This indicates that, at the same internal heat generation rate, the heat dissipation differed when using Formula (III.24) instead of Formula (III.32) after the null current section. This behaviour was also observed during the continuous discharge test, but it was limited to a peak average temperature of 23.3 °C instead of 23.4 °C.

The temperature distribution in the cell and environment confirmed the hypothesis of adiabatic surfaces rather than modelling the plastic battery holder. While the bottom surface of the battery holder was adiabatic due to the added thermal resistance of the flooring, it was possible to integrate the heat flux over the lateral surfaces of the battery holder, as shown in Formula (III.32). The results showed that these contributions were negligible on both sides, as their peak was on the order of 10^{-8} W. The discussion of the Biot number previously presented can be directly applied to the CFD analysis because the heat generated was dissipated in the environment solely in the radial direction. The thermal conductivity of the cell in the axial direction did not influence the thermal behaviour of the cell. Figure III.19 displays the contours for the partial discharge test at four different steps, clearly showing how the air near the cell's surface has a higher temperature than the free slip zone. Similar results were obtained for the continuous discharge tests.

(a)

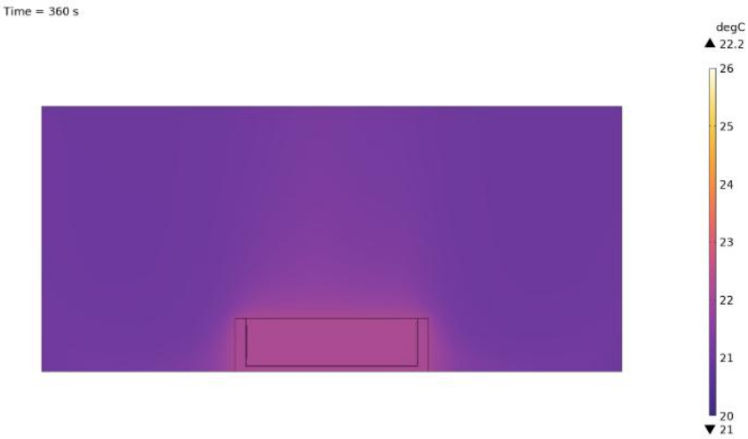

(b)

(c)

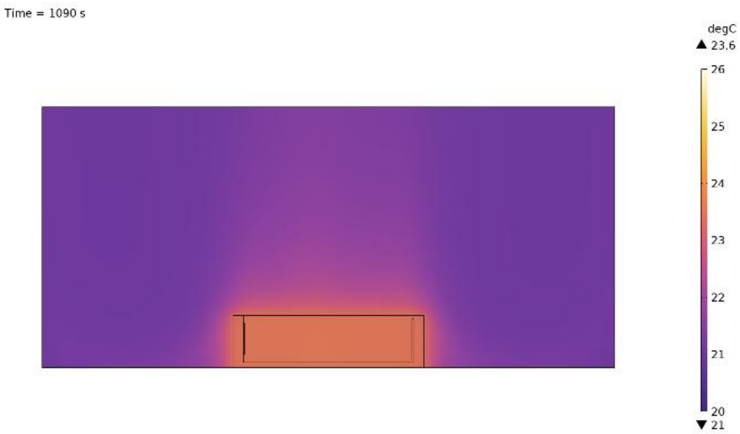

(d)

Figure III.19 *Contours of the LTO cell at 0 s (a), 360 s (b), 720 s (c), and 1090 s (d), referred to the CFD partial discharge simulation*

III.4.3 CFD model experimental validation

The CFD model was experimentally validated, like the simplified thermal model. Temperature measurements shown in Figure III.15 were compared to the average temperature trend of the cell using Formula (III.28). While the first data point had percentage errors comparable to the simplified thermal model, the other comparisons resulted in higher percentage errors, still within ±5%. Table III.5 presents the results for each temperature measurement for both tests.

Table III.5 *Experimental percentage errors between temperature measurements and the CFD numerical results*

CONTINUOUS DISCHARGE		PARTIAL DISCHARGE	
T_{exp} [°C]	CFD	T_{exp} [°C]	CFD
21.8	+0.2%	21.0	+0.5%
22.9	–0.2%	23.3	–4.7%
23.9	+3.4%	23.9	–3.1%

The R^2 reached optimal values through CFD modelling, particularly during the partial discharge. According to the results, the coefficient of correlation for the continuous discharge test was 97.8%, while it was 96.1% for the partial discharge test. These values decreased by –0.7% and increased by +0.9% compared to the Kuehn and Goldstein and the Morgan formulas, which had the highest R^2 among the Nusselt empirical correlations. The outcome demonstrated the reliability of the CFD model, especially for long-duration tests.

III.4.4 Comparison between heat rates and choice of the Nusselt correlation

The CFD analysis results showed a good correspondence between empirical correlations and surrounding air modelling through the Navier-Stokes equations. Experimental validation for both models achieved percentage errors between simulation outcomes and temperature measurements in ±5%, while the coefficients of correlation reached values over 95%. The main inconvenience of studying temperatures was the proximity of the results, although the convective heat exchange was modelled in several ways. The comparison between temperatures and experimental validation could not provide a criterion for choosing the optimal empirical Nusselt correlation. Therefore, it was necessary to compare dissipated heat rates directly related to the convective heat exchange.

As reported previously, the difference in the average temperature peak values suggested that the dissipated heat rates assumed different trends in the second part of the discharge tests. The dissipated heat rate trends during both tests are compared in Figure III.20.

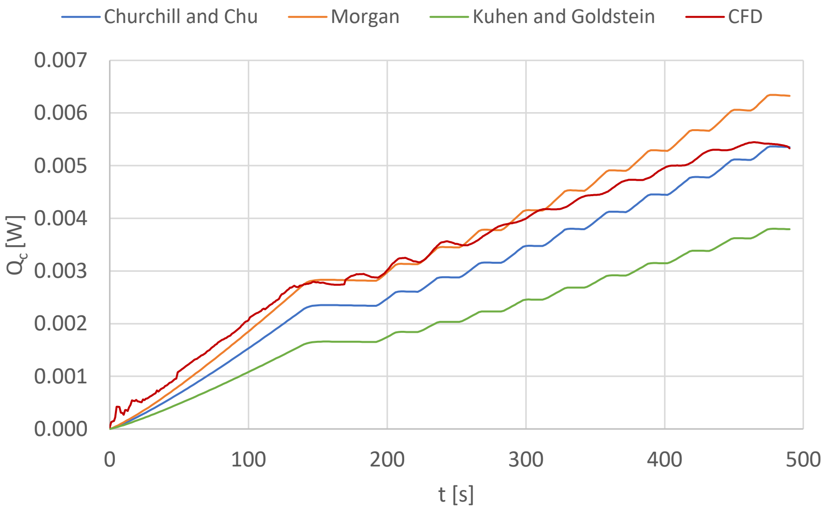

(a)

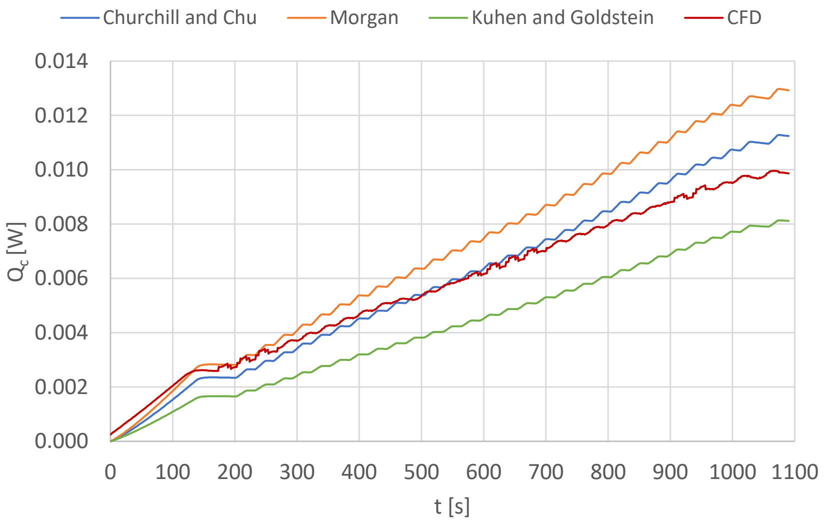

(b)

Figure III.20 *Dissipated heat rate trends for continuous (a) and partial (b) discharges*

According to the CFD analysis, the dissipated heat rate assumed higher values at the beginning of both tests, indicating a higher dissipation than the simplified approach. This difference manifested significantly between the CFD outcomes and the Kuehn and Goldstein correlation. The dissipated heat rate estimated using Formula (III.16) was lower by −41% and −34% compared to the CFD outcome for continuous and partial discharges at the beginning of the null current section. The correlation proposed by Morgan produced the closest trend, achieving percentage differences of +1% and +5% in the same conditions.

When discharge cycles occurred, the dissipated heat rate increased. The rapidity of the curves was changed by using different correlations or by applying the CFD. This feature is the main cause of the discrepancy in the peak average temperatures. According to the CFD analysis, when the null current section of the continuous discharge ended, the dissipated heat rate increased by 0.002 W in 290 s. The Churchill and Chu correlation and the Morgan expression manifested a higher increment of 0.003 W, indicating a more rapid increasing trend. Although the Kuehn and Goldstein correlation produced the maximum span with the CFD results, the growing velocity was the same. The results of the partial discharge test are completely analogous because the trends had similar slopes.

The optimal Nusselt correlation was selected by comparing the Root Mean Squared Error (RMSE) between the CFD results and the outcomes of the simplified thermal model. The correlation with the lowest RMSE was identified as the best for the presented cases. Because of the low magnitude of the results, the RMSE was calculated as a percentage of the maximum dissipated heat rate for each CFD simulation. Its expression is shown in Formula (III.35).

$$RMSE_{\%} = \frac{100}{max\left(\dot{Q}_{CFD}\right)} \sqrt{\sum_{i=1}^{4} \frac{\left(\dot{Q}_{CFD,i} - \dot{Q}_{conv,i}\right)^2}{4}} \qquad \text{(III.35)}$$

Table III.6 reports the RMSE for each correlation. According to the results, the Morgan correlation best suited the continuous discharge test by achieving an error of 6.3%. The Churchill and Chu formula enabled an optimal estimation of the dissipated heat rate trend for the partial discharge test. Although the Kuehn and Goldstein correlation displayed the same growth rate over time, its selection resulted in no acceptable error when comparing the CFD and the simplified thermal model.

Table III.6 *Percentage RMSEs between the CFD and the simplified thermal model*

	CONTINUOUS DISCHARGE			PARTIAL DISCHARGE		
	Churchill and Chu	**Morgan**	**Kuehn and Goldstein**	**Churchill and Chu**	**Morgan**	**Kuehn and Goldstein**
$RMSE_{\%}$	8.8%	6.3%	25.6%	5.8%	15.6%	16.1%

Therefore, the Morgan correlation was regarded as the most reliable method for the continuous discharge test. Conversely, the Churchill and Chu correlation was identified as the most dependable formula for the partial discharge test. This behaviour suggests that for tests lasting more than 500 seconds, the Churchill and Chu correlation is the best option. The Morgan correlation, on the other hand, is more suitable for shorter tests (below 500 seconds). This outcome is demonstrated by the different slope of the dissipated heat rate related to both correlations. Indeed, the Morgan correlation is more accurate in capturing the faster initial dissipation, whereas Churchill and Chu formula offer a better fit in the long run, avoiding the overestimation of dissipation that characterises Morgan over extended timescales.

III.5 Summary of the relevant outcomes

According to the simplified thermal model, the peak internal heat generation rate reached 0.240 W, matching the peak currents observed in both tests. The heat dissipation ratio increased over time, driven by the growth of the convective heat transfer coefficient. Initially, natural convection was inactive because the temperature difference between the cell's surface and the surroundings was minimal. By the end of the continuous discharge test, the dissipated heat rates were measured as 0.005 W, 0.006 W, and 0.004 W, based on the Churchill and Chu, Morgan, and Kuehn and Goldstein correlations, respectively. Higher peaks of 0.011 W, 0.013 W, and 0.008 W were recorded for the partial discharge test. The imbalance between heat generated and dissipated caused the temperature to rise over time. However, the cell did not reach dangerous conditions because the peak average temperatures of both tests remained within the optimal temperature range for Li-ion batteries. These peaks were 23.4 °C and nearly 24.0 °C for the continuous and partial discharge tests, respectively. The temperature distribution was uniform across all tests, due to the low radial Biot number, which was on the order of 10^{-2}. Although the convective heat transfer coefficients evaluated by empirical correlations varied significantly, especially toward the end of the simulations, they did not notably affect the overall temperature trend. This was confirmed by experimental validation, which involved three temperature measurements taken with a thermal camera and a real LTO cylindrical cell. The results showed that the simplified thermal model achieved percentage errors within ±5%, with correlation coefficients of 98.3% and 95.6% for the continuous and partial discharge tests, respectively.

The detailed CFD model included the actual ABS battery holder and examined the practical applicability of empirical correlations originally developed for simple cylindrical geometries, avoiding drawbacks related to the low measurement accuracy of the thermal camera as the dissipated heat rate was derived from the temperature field of the ambient air. This method affected the average temperature peaks, which were lower at 23.3 °C and 23.6 °C. The temperature field appeared uniform, confirming the assumption of adiabatic lateral and bottom surfaces. After verifying that the CFD results matched the experimental temperature measurements within a ±5% error margin, the CFD analysis showed that the Morgan correlation yielded the lowest RMSE for the full discharge test. The Churchill and Chu formula was suitable for the partial discharge test. The results suggested that the Morgan correlation is most appropriate for simulations under 500 seconds, whereas the Churchill and Chu correlation is better for longer-duration tests. The Kuehn and Goldstein correlation predicted the dissipated heat rate with a slope similar to the CFD model during the second phase of testing. The higher RMSEs made it less accurate and practical.

Despite the analysis have been conducted at 1C of peak current, at higher C_{rate} the reliability of the modelling can be improved because the impact of experimental accuracy is effectively reduced. This is primarily because testing at higher rates, such as 2C or 4C, involves significantly higher currents that result in greater heat generation and a much larger temperature difference. Consequently, the ±1.5 °C margin of error associated with the thermal camera becomes negligible relative to the overall temperature increase, minimizing its influence on the final calculations. This perspective is further supported by the fact that thermal management is inherently more critical and demanding during high C_{rate} operations, where accurate trend replication is paramount.

Chapter IV
Design of a Cold Plate System for a Commercial LTO Battery Pack

IV.1 Introduction

The present chapter addresses a critical gap in thermal management systems research, which generally relies on simplified laboratory configurations. It discusses the development and optimisation of an innovative liquid cold plate utilizing a heat sink and minichannel technology specifically for a commercially available battery pack used in the automotive and railway sectors. The analysis of this existing product, with its inherent restricted space and thermal constraints, provides a step toward industrial applicability. The goal is to keep the average temperature of each cell within the range 20 °C to 30 °C, which is more conservative than the optimal interval defined by Pesaran et al. (Pesaran, Santhanagopalan and Kim, 2013). At the same time, another target is to control the maximum internal temperature span below 5 °C. The environment interface consists of a close enclosure that contains the battery pack. Its surface temperature is hypothesized to be 45 °C, as the test regulations of Li-ion battery packs in a critical hot ambient. The design process was established as an optimal compromise between component bulk and required thermal efficiency. The primary contribution is two-fold. The work proposes an optimised minichannel cold plate design, developed through a continuous improvement process starting from a commercial configuration, which successfully mitigates the maximum temperature span across the cells and the average temperature control. Second, this research introduces an iterative design methodology that first leverages simplified analytical sizing to guide initial choices (channel diameter and fluid velocity) and subsequently employs

Finite Element Method (FEM) analysis to validate or refine these preliminary hypotheses. As the previous case, COMSOL Multiphysics was selected as simulation package for the analysis. The final optimized cold plate, featuring vertical minichannels, demonstrates superior thermal performance and is presented as a solution directly feasible for commercial applications.

IV.2 Materials and methods

IV.2.1 Battery pack description and characterisation

The study analysed the Toshiba SCiB Type3-20 Battery Pack. The device is formed of 24 Toshiba SCiB prismatic cells of 20 Ah, arranged in two modules of 12 connected in series. The modules are connected in parallel, determining a 2P12S configuration. Table IV.1 reports other datasheet features of a single 20 Ah Toshiba SCiB (Toshiba, 2026a) and the Type 3-20 battery pack (Toshiba, 2026b).

Table IV.1 *Datasheet of the Toshiba SCiB (Toshiba, 2026a) cell and the Type-3-20 battery pack (Toshiba, 2026b)*

Toshiba SCiB 20 Ah cell		Toshiba SCiB Type3-20 Battery Module	
Nominal capacity	20 Ah	Model name	FM1202CCA04A
Nominal voltage	2.3 V	Rated capacity	40 Ah
Cell type	LTO	Nominal energy	1104 Wh
Energy density	89 Wh·kg^{-1}	Nominal voltage	27.6 V
Dimensions	116 x 22 x 106 mm	Maximum current	160 A
Weight	550 g	Weight	14 kg

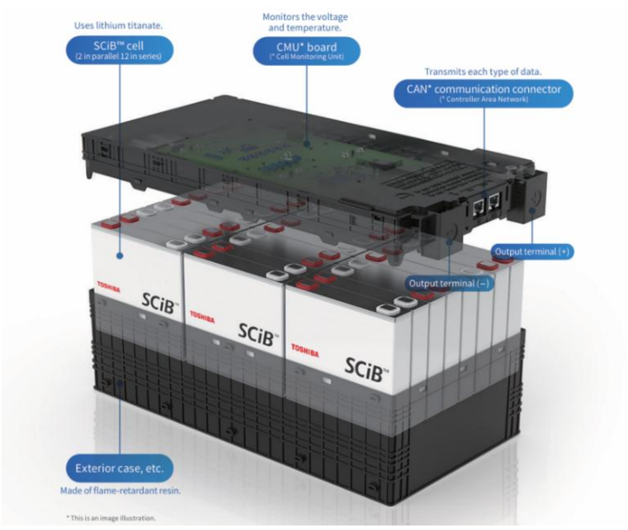

(a)

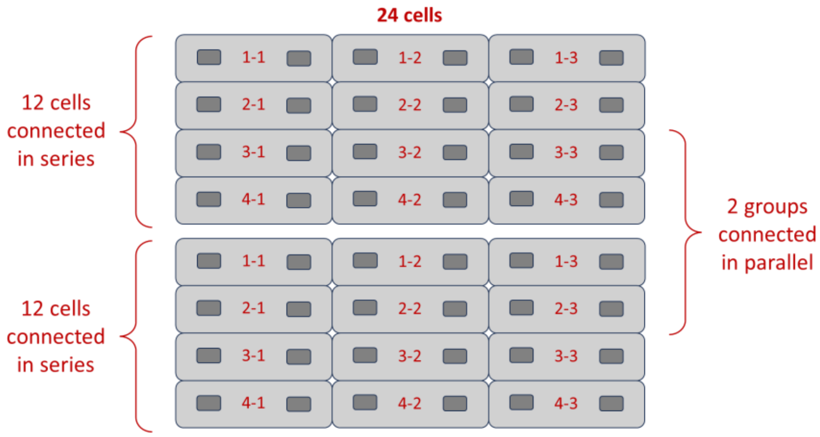

(b)

Figure IV.1 *Toshiba SCiB Type 3-20 battery pack (a) and cell arrangement (b)*

Thermal properties and physical parameters of the cells were recovered in the literature. Zatta et al. (Zatta *et al.*, 2025) proposed a thermal study on a prismatic 20 Ah LTO cell whose datasheet features are extremely analogous to the Toshiba SCiB cell. Table IV.2 reports the specific heat, thermal conductivity, and density of the cell body, while the electrodes are made of aluminium.

Table IV.2 *Thermal properties and physical parameters considered for the analysis (Zatta et al., 2025)*

Thermal properties and physical parameters		
Specific heat ($c_{p,cell}$)	1100	$J{\cdot}kg^{-1}K^{-1}$
Thermal conductivity (λ_{cell})	x: 0.8; y: 31; z: 31	$W{\cdot}m^{-1}K^{-1}$
Density (ρ_{cell})	1977	$kg{\cdot}m^{-3}$

The geometry of the single cell was defined by the datasheet indications, replicating the exact shape and dimensions. Figure IV.2 represents the geometrical model of the prismatic cell and the reference coordinate system in accordance with the thermal conductivity reported in Table IV.2.

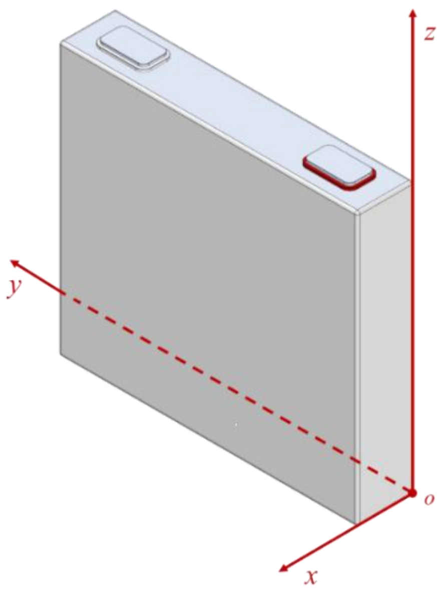

Figure IV.2 *Toshiba SCiB 20 Ah cell geometry model and reference coordinate system*

The peak heat generation rate of the battery pack was another piece of information for the cooling system design. It is a significant part of the thermal load and influences the dimensions of the diameters and the coolant velocity (Lai *et al.*, 2019). This parameter can be calculated by estimating the internal heat generation of a single cell in maximum discharge current conditions of the battery pack. As reported in Table IV.1, the maximum discharge current of the Toshiba SCiB Type3-20 is equal to 160 A, corresponding to a 4C rate. Due to the arrangement of the cells in two parallel modules, each one is characterised by a peak current of 80 A.

The application of the mentioned procedure was carried out using the Bernardi et al. (Bernardi, Pawlikowski and Newman, 1985) equation, reported in Chapter III as Formula (III.18). In accordance with other studies (Nazari and Farhad, 2017; Wu *et al.*, 2021; Zhang *et al.*, 2023b; X. Li *et al.*, 2024), reversible heat is generally neglected at high currents and low temperatures. The chosen discharge condition, characterised by the maximum acceptable C_{rate} by the battery pack, makes the negligibility of reversible heat a practicable hypothesis for the design process. The difference between the open-circuit and terminal voltage was obtained by applying the 2nd order Thevenin model, whose ECM is represented in Figure III.3. Its typical resistances and capacitances were evaluated through the Hybrid Power Pulse Characterisation (Zhang *et al.*, 2018). The procedure established the ECM electrical parameters of the reference prismatic cell depending on SOC, as the simplified thermal model proposed in Chapter III.

The HPPC of the Toshiba SCiB cell was performed by Hussain et al. (Hussain, Khan and Pathak, 2024), who obtained the fitted equations reported from Formulas (IV.1) to (IV.5). Resistances and capacitances are evaluated in Ohms (Ω) and Farads (F), respectively.

$$R_0(SOC) = 0.00114 \cdot SOC^5 - 0.00053 \cdot SOC^4 - 0.00212 \cdot SOC^3 + 0.00256 \cdot SOC^2 - 0.00135 \cdot SOC + 0.0011 \quad \text{(IV.1)}$$

$$R_1(SOC) = 9.394 \cdot 10^{-2} \cdot SOC^5 - 0.22316 \cdot SOC^4 + 0.1927 \cdot SOC^3 - 7.445 \cdot 10^{-2} \cdot SOC^2 + 1.243 \cdot 10^{-2} \cdot SOC - 8 \cdot 10^{-5} \quad \text{(IV.2)}$$

$$C_1(SOC) = (2.189 \cdot SOC^5 - 2.439 \cdot SOC^4 - 1.432 \cdot SOC^3 + 2.125 \cdot SOC^2 - 6.165 \cdot SOC - 1.8605) \cdot 10^7 \quad \text{(IV.3)}$$

$$R_2(SOC) = -0.02445 \cdot SOC^5 + 0.08901 \cdot SOC^4 - 0.11083 \cdot SOC^3 + 0.05648 \cdot SOC^2 - 0.01145 \cdot SOC + 0.00201 \quad \text{(IV.4)}$$

$$C_2(SOC) = (-1.0811 \cdot SOC^5 + 2.5486 \cdot SOC^4 - 2.1855 \cdot SOC^3 + 0.83536 \cdot SOC^2 + 0.13927 \cdot SOC + 0.0240214) \cdot 10^6 \quad \text{(IV.5)}$$

The maximum value of the curve represented in Figure IV.3 corresponds to the thermal load portion related to the battery pack internal generation. A dynamic calculation was performed by simulating a 4C constant discharge of the 20 Ah Toshiba SCiB cell through Simulink. Due to the SOC dependency of the circuit parameters, the generated heat changes over time. The corresponding electrical internal impedance variation of the cell principally causes it. According to the results, the peak heat generation rate to be implemented in the system design phase equals 22.0 W.

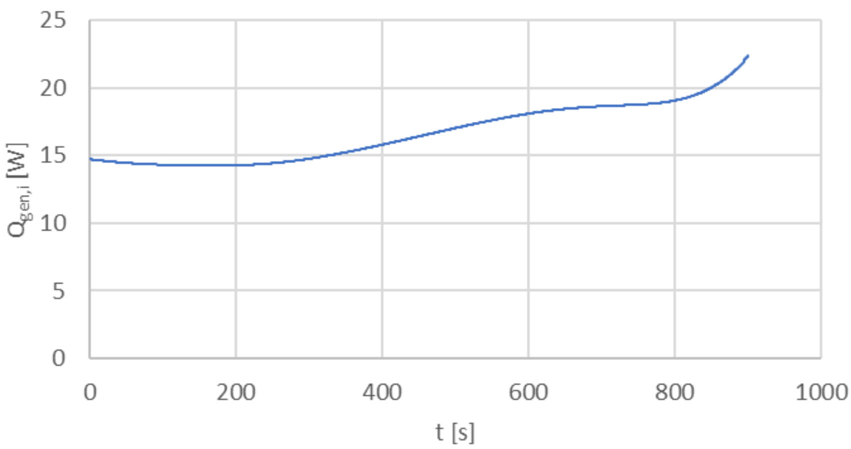

Figure IV.3 *Internal heat generation rate of the single prismatic cell at 4C constant discharge*

The characterisation of the battery pack and its cells also regarded the heat generation rate of the electrodes. The exposed parts of the electrodes are made of aluminium. Hypothesizing a normal direction of electric current through the electrodes, the heat generation rate was estimated using the 2nd Ohm's law for pure resistive electric loads, as reported in Formula (IV.6).

$$\dot{Q}_{gen,el} = R_{el}|I| = \frac{1}{\sigma_{alu}} \frac{th_{el}}{A_{el}} |I| \quad \text{(IV.6)}$$

The heat generation rate for both electrodes is $1.9 \cdot 10^{-3}$ W. It corresponds to less than 1% of the internal heat generation rate of the entire cell. Therefore, this contribution was neglected.

IV.2.2 Thermal boundary conditions

Figure IV.1 (a) represents the Toshiba Type3-20 battery pack and its exterior case, which is made of a flame-retardant resin. Research highlights several key advantages of using these materials in Li-ion battery packs, such as the delay or prevention of fire spreads (Chen *et al.*, 2025), self-extinguishing ability (Zhu *et al.*, 2025), and improved thermal stability (Gao *et al.*, 2020). Due to these features, flame-retardant cases are also necessary concerning safety standards and regulations (Jahl *et al.*, 2025).

During the design phase, the enclosure defined the boundary conditions of the thermal problem, specifically concerning two principal contributions:

1. *Natural convection*: The exterior case influences the airflow around the battery pack. While in open spaces the velocity field depends on a single surface temperature, within the enclosure, the temperature of two parallel sides affects the flow.
2. *Irradiance*: Irradiance significantly influences the boundary conditions of the problem. While in open spaces the heat flux depends on single object emissivity for two parallel surfaces, the heat transfer is governed by the emissivity of both surfaces.

The enclosure temperature surfaces were set at 45 °C. This choice was made in accordance with IEC 62660-1:2010 international standard. It concerns the performance of Li-ion batteries in ordinary working conditions (Di Persio and Ruiz, 2018). The regulation establishes the number of times that a battery can withstand charging and discharging before its capacity decays to a specified value under a certain charging and discharging profile (Zhou *et al.*, 2022). The document specifies that the test temperature is set to 45 °C ± 2 K to verify the behaviour of Li-ion battery packs under thermal stress conditions.

The mentioned boundary conditions can be particularised for each surface of the battery pack. The surfaces were numbered for reference in boundary conditions as A_1, A_2, A_3, and A_4. Due to the problem symmetry, it was possible to study half of the battery pack, as represented in Figure IV.4.

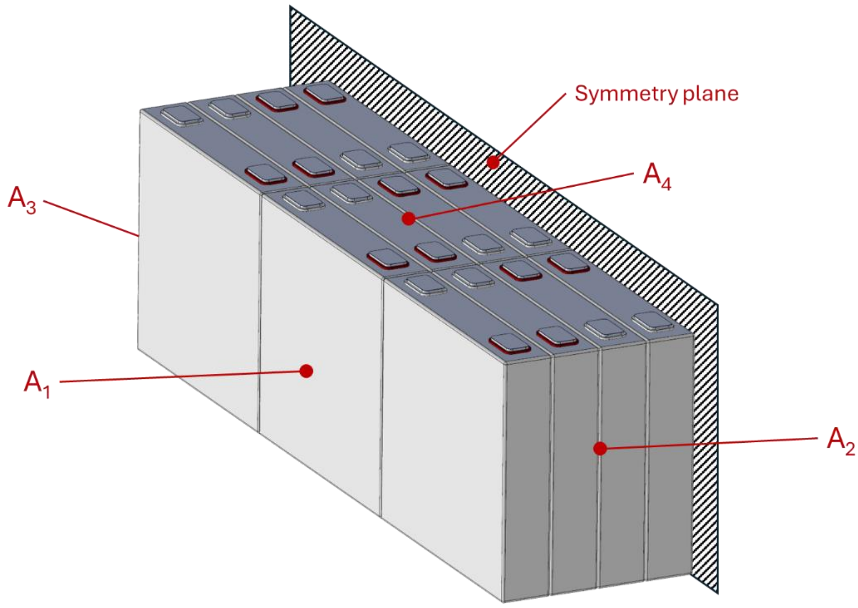

Figure IV.4 *Details of the battery pack and its boundary surfaces*

Surfaces A_1, A_2, and A_3 were exposed to the vertical sides of the insulated case, while the surface A_4 was exposed to the upper horizontal surface. Instead, the battery pack bottom area was in contact with the enclosure base and supposed adiabatic. The natural convective heat exchange was calculated side by side by applying a simplified model of free convection inside enclosures (Cengel, 2022). When the Nusselt number is known, the rate of heat transfer through the enclosure can be determined from Formula (IV.7).

$$\dot{Q}_{conv,i} = h_{enc}A_i(T_{enc} - \bar{T}_i) \qquad for\ i = 1, 2, 3 \tag{IV.7}$$

The elements in Formula (IV.7) are the natural convective heat transfer coefficient h_{nat}, the heat exchange surface A_i, the enclosure temperature T_{enc}, and the average temperature of the battery pack surface $\bar{T}_i$. The natural convective heat transfer coefficient was obtained through the MacGregor and Emery (Macgregor and Emery, 1969) correlation. Supposing an air enclosure thickness t of 10 mm (Bai *et al.*, 2023), this formula is particularly suitable for this application. Formulas (IV.8) and (IV.9) report the Rayleigh number expression for vertical enclosures and the mentioned correlation. All air properties, indicated by the subscript *air,enc*, are to be evaluated at the average fluid temperature between T_{enc} and $\bar{T}_i$ (Cengel, 2022).

$$Ra_{air,enc} = \frac{g\beta_{air,enc}(T_{enc} - \bar{T}_i)t^3}{{\nu_{air,enc}}^2} Pr_{air,enc} \tag{IV.8}$$

$$Nu_{air,enc} = 0.42\, {Ra_{air,enc}}^{1/4} {Pr_{air,enc}}^{0.012} \left(\frac{H}{t}\right)^{-0.3} \begin{cases} 10 < H/t < 40 \\ 1 < Pr_{air,enc} < 2 \cdot 10^4 \\ 10^4 < Ra_{air\ enc} < 10^7 \end{cases} \tag{IV.9}$$

The irradiation contribution was estimated using the simplified model of two parallel slabs, well known in the literature (Rohsenow, Hartnett and Cho, 1998). The model can be applied by neglecting the side edge effects of the enclosure. Formula (IV.10) reports the inward radiative heat transfer rate in a generic surface of the battery pack exposed to the enclosure.

$$\dot{Q}_{rad,i} = \frac{A_i \sigma ({T_{enc}}^4 - {\bar{T}_i}^4)}{\frac{1}{\varepsilon_{enc}} + \frac{1}{\varepsilon_i} - 1} \qquad for\ i = 1, 2, 3, 4 \tag{IV.10}$$

The physical quantities listed in Formula (IV.10) include the Stefan-Boltzmann constant σ and the emissivity ε of the flame-retardant case and the battery pack surfaces. The emissivity values were recovered in the literature, considering typical constant parameters applied to black plastic (Chen and Chen, 2016), standard white coating (Shakir *et al.*, 2022), and polished aluminium (Calvagna *et al.*, 2022). The black plastic corresponds to the enclosure, the white coating to the battery pack vertical surfaces, and the polished aluminium to the top horizontal surfaces. Table IV.3 reports the emissivity values found in the literature.

Table IV.3 *Typical emissivity values applied to the enclosure and the battery pack surfaces (Chen and Chen, 2016; Calvagna et al., 2022; Shakir et al., 2022)*

	Emissivity
Black plastic	0.94
White coating	0.90
Polished aluminium	0.05

A conductive contribution was hypothesized on surface A_4. While the vertical surfaces experienced combined heat transfer mechanisms involving convection and irradiance, the horizontal top surface of the battery pack could not exhibit free convection. This happens because natural convection in horizontal enclosures is primarily driven by buoyancy forces resulting from a hot bottom surface and a cold top surface (Sezai and Mohamad, no date). If the top surface is hotter than the bottom, as in the presented design, the fluid near the top becomes less dense and tends to remain above the denser, cooler fluid below (Jobby, Khatamifar and Lin, 2025). This configuration is gravitationally stable, suppressing convective motion and making heat transfer dominated by conduction and irradiance. Formula (IV.11) represents the conductive heat transfer rate concerning the horizontal surface of the battery pack.

$$\dot{Q}_{cond,4} = \frac{\lambda_{enc}\, A_4}{t}\,(T_{enc} - \bar{T}_4) \qquad \text{(IV.11)}$$

IV.2.3 Design process and assumptions

This research focuses on developing and optimising an innovative liquid cold plate with vertical heat sinks and minichannel technology. It is specifically designed to be integrated into a commercially available battery pack used in demanding automotive and railway applications. The entire design process was carried out as an exercise in achieving the best balance, weighing the need for high thermal efficiency against the goal of minimizing overall component size. The design process was based on two features:

1. *Progressive optimisation of the cold plate*: The design process was obtained through a continuous improvement process that started from a commercial-type cold plate to the final solution. Each step represented an improvement of the previous technology by focusing on a specific issue, effectively mitigating the maximum temperature span within the cells and providing precise average temperature control.
2. *Preliminary sizing and FEM verification*: Each cold plate was realised by a two-step process. The first concerned a preliminary sizing of the channels, applying simplified hypotheses and empirical correlations to achieve the desired targets. The second one was realised through FEM modelling. This further approach validated the preliminary sizing results and verified the feasibility of the simplified assumptions. In case of disagreement, FEM modelling was used as a correction tool.

Figure IV.5 schematises the principal steps of the preliminary sizing procedure. These actions are contextualised in the following paragraphs, depending on the proposed cold plate technology.

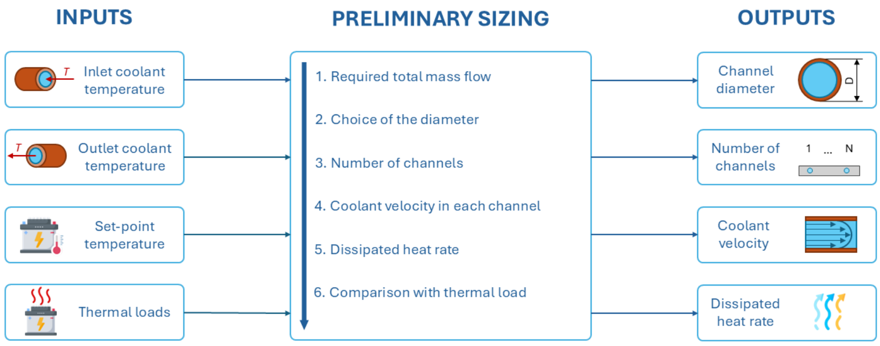

Figure IV.5 *Preliminary sizing procedures listed step by step*

For the preliminary channel sizing, the cooled water inlet and outlet temperatures were treated as design parameters and were therefore prescribed as part of the initial assumptions. The same approach was applied to the set-point temperature of the battery pack cells. The goal was to maintain the cells' average temperature within 20 °C to 30 °C. This is a more conservative range than the optimal defined by Pesaran et al. (Pesaran, Santhanagopalan and Kim, 2013) establishing a safety margin for the battery pack during ordinary working conditions. The set-point temperature for each cell was determined as the midpoint of the design interval, corresponding to 25 °C. Formula (IV.12) indicates how the average temperature of each cell was calculated. The term *Vol* represents the volume of a single 20 Ah cell.

$$\bar{T}_{cell} = \frac{1}{Vol} \int_{Vol} T(x, y, z)\, dVol \tag{IV.12}$$

At the same time, the liquid cold plate must realise uniformity throughout the battery pack, managing the maximum internal temperature difference below 5 °C. Formula (IV.13) reports how the temperature span was estimated.

$$\Delta T_{max} = max\{T(x, y, z)\} - min\{T(x, y, z)\}\, for\ (x, y, z) \in Vol \tag{IV.13}$$

The uniformity of the temperature field within each cell was achieved by minimising the Biot number. A small Biot number ($Bi \leq 0.1$) indicates that internal conduction is much efficient than external convection, leading to a nearly uniform temperature field inside the object. A large Biot number ($Bi > 1$) means significant internal temperature gradients, causing a non-uniform field (Cengel, 2022). Formula (IV.14) defines the Biot number along a generic direction.

$$Bi_i = \frac{h_w l_i}{\lambda_{cell}} \qquad for\ i = x, y, z \tag{IV.14}$$

The previous paragraphs described the models and criteria to estimate the total thermal load. The internal heat generation rate of each cell and heat transfer through lateral surfaces create a unique thermal load that determines the cooling capacity of the refrigeration unit. Formula (IV.15) indicates this design input parameter.

$$\dot{Q}_{tot} = N_{cell} \cdot \dot{Q}_{gen} + \sum_{i=1}^{3} \dot{Q}_{conv,i} + \sum_{i=1}^{4} \dot{Q}_{rad,i} + \dot{Q}_{cond,4} \tag{IV.15}$$

N_{cell} represents the number of cells. Figure IV.6 summarises the thermal load contributions from the boundaries and the internal heat generations.

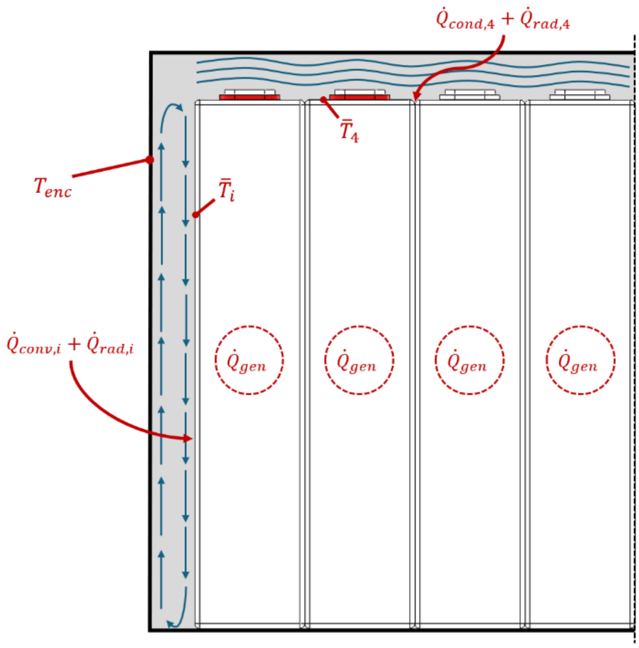

Figure IV.6 *Scheme of the heat loads of a half battery pack*

A preliminary evaluation of the required cooling capacity was performed by imposing the battery pack's surface temperatures equal to the set-point of 25 °C. According to the results, the total internal heat generation rate is 528.0 W, while the inward heat rates by convection, irradiance, and conduction are 8.4 W, 13.2 W, and 3.5 W. The total thermal load is 553.0 W and corresponds to the refrigeration unit's nominal cooling capacity of the TMS. Applying the symmetry hypothesis, the required cooling capacity for half the battery pack is 276.5 W.

IV.3 Progressive design of the innovative cold plate system

IV.3.1 Internal heating strategies

IV.3.1.1 Preliminary sizing

Designs coupling copper serpentines embedded in silicon or aluminium cold plates show superior cooling compared to air-based systems, maintaining battery temperatures below critical thresholds and reducing temperature differences across cells. For example, a silicon cold plate with copper tubes kept the maximum battery temperature below 41.9°C and reduced energy consumption by 47.4% compared to forced air cooling (X. Li *et al.*, 2019). This technology has reached a level of maturity that makes it a readily available product on the market. For this reason, an aluminium cold plate was chosen as the study's baseline. It was designed to manage the temperature of 12 cells, corresponding to half a battery pack. According to the previous paragraph, the thermal load to dissipate was equal to 276.5 W. Despite being added another element that increase the battery pack system height, the volume inside the enclosure was supposed unaltered. Especially the spacing between surface A_4 and the enclosure was not changed because it has been necessary to guarantee optimal space for electrical connections of electrodes. This means the enclosure increased its overall height.

The shape and configuration of the plate and the copper serpentine were inspired by the Boyd CP10 4-pass Tubed Cold Plate (Boyd, no date) represented in Figure IV.7.

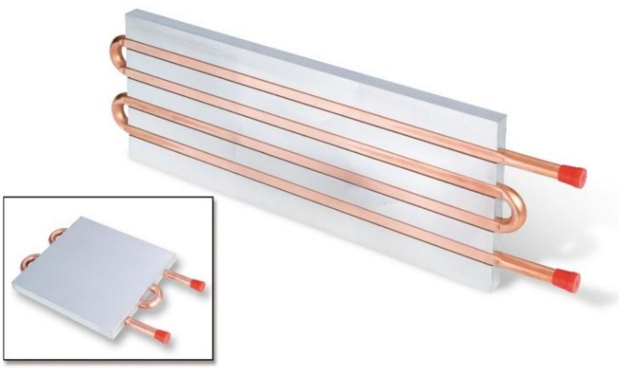

Figure IV.7 *Boyd CP10 4-pass Tubed Cold Plate*

Figure IV.8 presents the preliminary sizing flow chart for this cold plate, which is a further extension to the general procedure defined in Figure IV.5. Because the Reynolds number depends on the hydraulic diameter and the non-linearity of the Nusselt empirical correlations, the calculations were performed using an iterative approach.

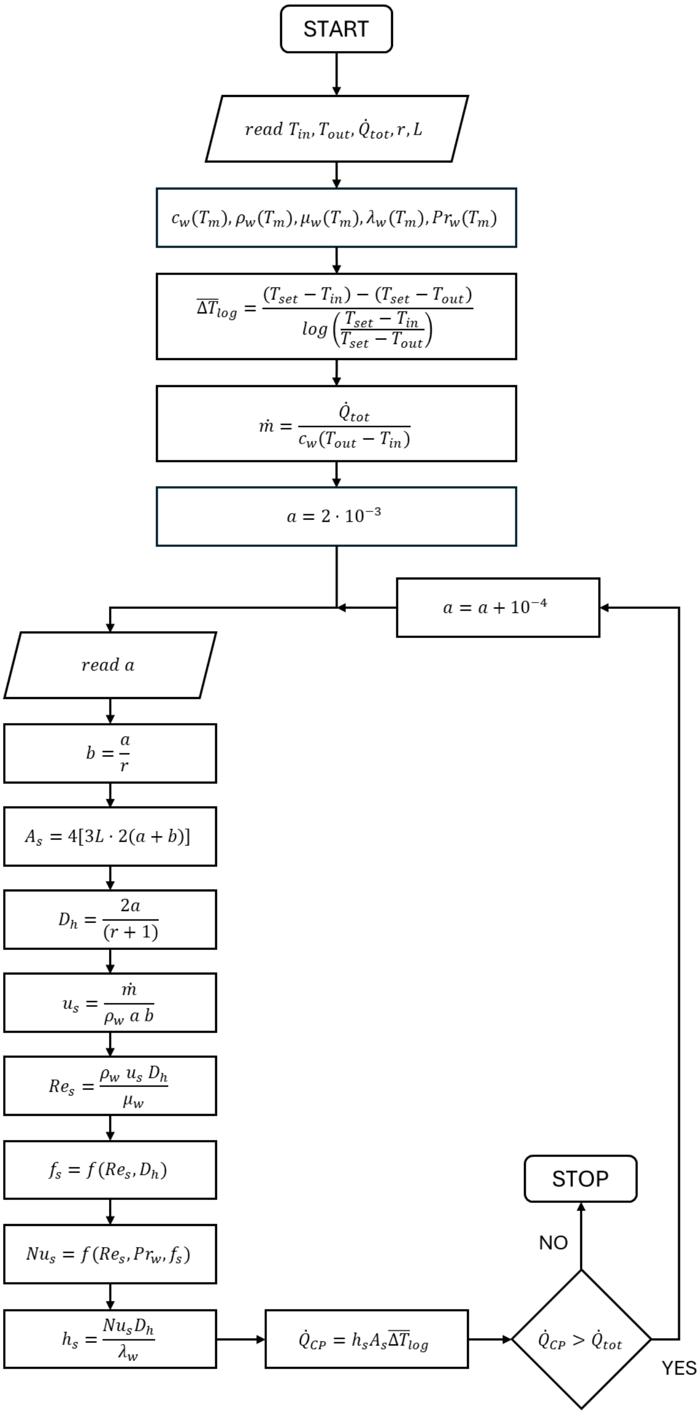

Figure IV.8 *Flow chart of the preliminary sizing procedure of the commercial-type cold plate*

The preliminary sizing scope focused on determining the optimal hydraulic diameter of the copper serpentine for maintaining the battery pack cells' average temperature within 20 °C and 30 °C. The design process considered a fundamental practical aspect: the minimum coolant velocity. As reported in the literature (Salhein, Kobus and Zohdy, 2022; Z. Chen *et al.*, 2023; Deng *et al.*, 2024; Zhang *et al.*, 2025), water velocities above 0.5 $m \cdot s^{-1}$ in water distribution systems are generally recommended to prevent air bubble stagnation and support optimal heat exchange efficiency. For this reason, it was decided to implement a copper serpentine characterised by a rectangular section to increase the coolant velocity by adopting a highly flattened geometry. The chosen aspect ratio r equalled 3 and was defined as the length a of the section divided by the height b.

The inlet and outlet water temperatures were determined based on the cell's set-point temperature and the design temperature interval. The outlet temperature was 20.0 °C, as the lower limit of the design interval, while the inlet temperature was 17.0 °C. This choice was made to limit the pressure drops of the copper serpentine while keeping the cold plate temperature field sufficiently uniform. Table IV.4 summarises the design inputs chosen for the commercial-type cold plate.

Table IV.4 *Commercial-type cold plate design inputs*

Commercial-type cold plate inputs		
Inlet temperature T_{in}	17.0	°C
Outlet temperature T_{out}	20.0	°C
Aspect ratio r	3	

Nu_w and f_w indicate the Nusselt number evaluated for the water flow inside the serpentine and the friction factor related to pressure drops within the duct. A_s represents the heat exchange surface between the coolant and the battery pack. Formulas (IV.16) and (IV.17) represent the Nusselt number correlations, the friction factor expressions, and the heat exchange surface between water and the battery.

$$Nu_s = \begin{cases} 3.61 & for\ Re_s < 2300 \\ \dfrac{(f_s/8) \cdot (Re_s - 1000) \cdot Pr_w}{\left[1 + 12.7 \cdot (f_s/8)^{0.5} \cdot \left({Pr_w}^{2/3} - 1\right)\right]} & for\ 3 \cdot 10^3 < Re_s < 5 \cdot 10^6 \end{cases} \quad \text{(IV.16)}$$

$$f_s = \begin{cases} 68.36/Re_s & for\ Re_s < 2300 \\ 0.316\ {Re_s}^{-1/4} & for\ 4 \cdot 10^3 < Re_s < 10^5 \end{cases} \quad \text{(IV.17)}$$

The first correlations of the Nusselt number and the friction factor valid for *Re* lower than 2300 correspond to a fully developed laminar flow in the hypothesis of constant heat flux (Cengel, 2022). Gnielinski (Gnielinski, 1976) developed the second Nusselt correlation, valid for fully developed turbulent flows in ducts. The second empirical correlation for the friction factor is valid for fully developed turbulent flows in smooth pipes and was proposed by Blasius (Blasius, 1913). The heat exchange surface was estimated as the perimeter of the rectangular section of the serpentine multiplied by the length of the battery pack. The result is multiplied by 4 because the serpentine has 4 passes. This formula is valid under the assumption of negligible heat transfer with the environment through the U-bend surfaces.

According to the results, the required rectangular section length was 6 mm. Therefore, the required height was 2 mm. Table IV.5 reports all the results of the preliminary sizing.

Table IV.5 *Commercial-type cold plate preliminary sizing results*

Commercial-type cold plate preliminary sizing								
D_h [mm]	a [mm]	b [mm]	u_s [$m \cdot s^{-1}$]	$\dot{m}$ [$g \cdot s^{-1}$]	Re_s	Nu_s	h_s [$W \cdot m^{-2} K^{-1}$]	$\dot{Q}_{CP}$ [W]
3	6	2	2.0	22	5479.0	9.7	1995.7	274.2

IV.3.1.2 FEM verification

The commercial-type cold plate was implemented for the FEM analysis. The verification process aimed to demonstrate the cold plate thermal efficiency and evaluate the correctness of the preliminary sizing. The simulation was run in steady-state operation. As reported by the Raynolds number in Table IV.5, the flow regime in the serpentine was dominated by turbulence. The FEM analysis required a dedicated turbulence model coupled with the Navier-Stokes equations, as they provide essential closure to the system and enable practical, accurate predictions (Rodriguez, 2019). The chosen turbulence model for this application was the Algebraic Y Model, often referred to as Algebraic Stress Model (ASM), which is a Reynolds-Averaged Navier-Stokes (RANS) model effective for duct flows, especially in predicting secondary motions and mean flow features (Sharma, 1983). The sorting among the RANS models was performed by reducing the computational cost of the numerical simulations without influencing the precision of the results.

A preliminary mesh independence test was developed to achieve the optimal compromise between accuracy and computational costs. There is no standardised procedure for these tests, and it mostly depends on the researcher's experience and knowledge (Lee *et al.*, 2020). Referring to Figure IV.1 (b), it has been decided to compare the maximum internal temperature span of cell 1-1, as described by Formula (IV.13). The mesh was retained optimally when the percentage error between the temperature span of the selected meshes and the finest mesh achieved values below 1.5 %. The percentage error was estimated using Formula (IV.18).

$$err_{\%,i} = \left| \frac{\Delta T_{max,i} - \Delta T_{max,fine}}{\Delta T_{max,fine}} \right| \cdot 100 \qquad \text{(IV.18)}$$

Fig. IV.9 shows the mesh independence results. According to the analysis, the optimal grid is characterised by 765191 elements.

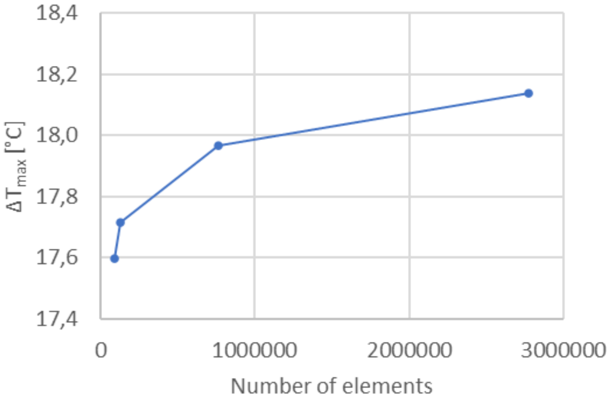

Figure IV.9 *Mesh independence analysis for the commercial-type cold plate simulation*

The cold plate did not reach the targets concerning the set-point temperature and the maximum temperature span for each cell of the battery pack. The average temperatures of the cells exceeded the design conditions, and the cold plate proved to be ineffective. Figure IV.10 reports the average temperatures (a) and the maximum temperature spans (b) of each cell belonging to a half battery pack. It also specifies the arrangement of the coolant inlet and outlet through the open sections of the serpentine. The red background colour indicates the target was not reached. Instead, the water outlet temperature was represented in green because it was extremely close to the design value.

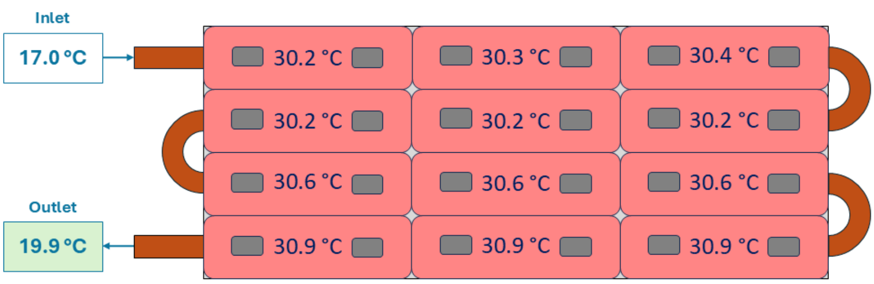

(a)

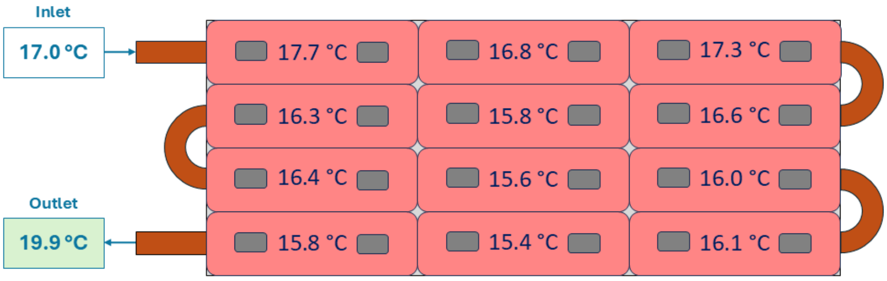

(b)

Figure IV.10 *Average temperatures (a) and maximum temperature spans (b) for the commercial-type cold plate*

The outlet temperature was subsequently obtained through the FEM simulation, after imposing the coolant inlet temperature, the heat load, and the geometry. The result of 19.9 °C is significant because it differed from the design value by 0.1 °C. The temperature field obtained through the simulation is shown by the contour reported in Figure IV.11.

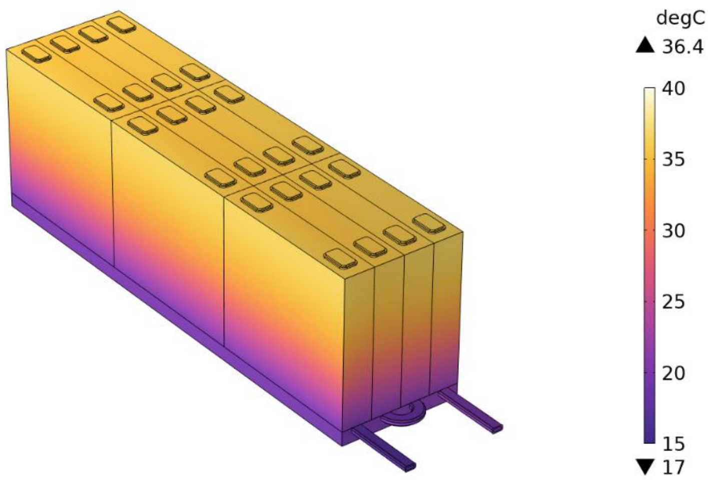

Figure IV.11 *Temperature contour of the commercial-type cold plate*

It showed a strong temperature gradient along the z-axis, while complete uniformity was achieved on the horizontal section planes. This behaviour can be explained by the preferred direction of heat dissipation and the low thermal conductivities of the battery pack. The thermal load was dissipated only in the vertical direction because the cold plate serpentine was positioned at the bottom of the battery pack. Due to the higher temperature of the enclosure, there was no dissipation through the lateral and top surfaces of the cells. The low thermal conductivity, on the other hand, resulted in a higher conduction resistance compared to the convection thermal resistance. The Biot number demonstrated this behaviour. Referring to Formula (IV.14) applied along the z-axis, and using the data reported in Tables IV.1 and IV.5, the Biot number was approximately 355. Such a high value indicates a highly irregular temperature field along the vertical direction.

IV.3.2 Cold plate with vertical heat sinks

IV.3.2.1 Preliminary sizing

The dissipation along the vertical direction of the thermal load is critical due to the low thermal conductivity of the cells and the inward heat contribution on the battery pack surfaces. To overcome these issues, the first improvement consisted of implementing vertical heat sinks to direct part of the thermal load in the horizontal direction. The heat sinks were developed along the length of the cold plate because, despite the thermal conductivity evaluated on the x-axis being lower than on the y-axis, the shorter cell width compensated for this issue. The thickness of a single heat sink was 1 mm to reduce the overall increase in width of the battery pack module.

From this point, two distinguished solutions will be compared concerning the horizontal cold plate. The first is called Serpentine Cold Plate (SCP) and refers to the adoption of a copper serpentine, such as the commercial-based technology. The second one implements rectangular horizontal minichannels and was called Horizontal Minichannel Cold Plate (HMCP). According to the classification reported by Kandlikar and King (Kandlikar and King, 2014), the difference between conventional channels and minichannels lies in hydraulic diameters. A channel is defined as minichannel if its hydraulic diameter assumes values below 3 mm. The HMCP was designed to achieve an improved distribution of coolant under a single cell rank compared to a unique concentration of water in a duct. Rectangular sections were adopted to ensure a coolant velocity higher than 0.5 $m \cdot s^{-1}$, as in the previous preliminary sizing. Due to the feasible efficacy of both configurations, the thermal analysis was conducted with serpentine and minichannels. Figure IV.12 represents both cold plates with heat sinks and cells.

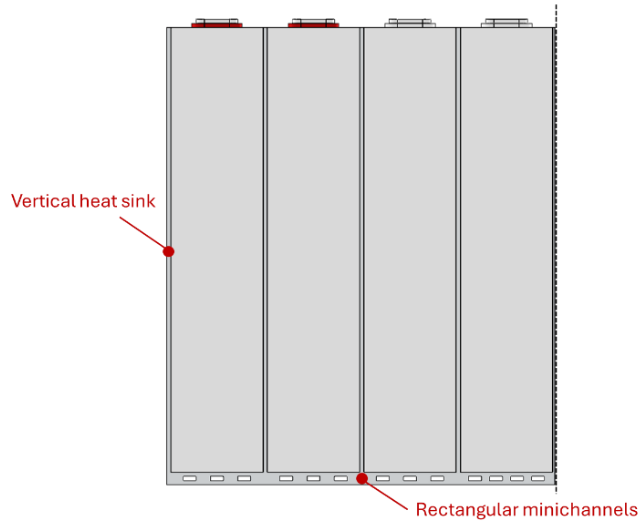

(a)

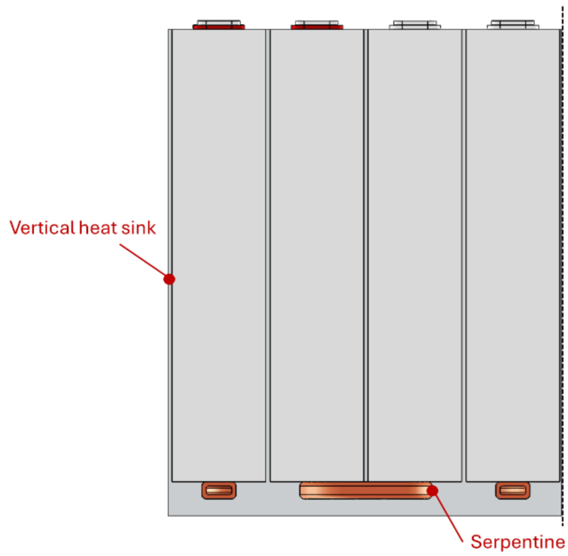

(b)

Figure IV.12 *Front view of the cold plate with the rectangular minichannels (a) and the serpentine (b)*

The HMCP cross-sections were designed by applying the flow chart shown in Figure IV.13.

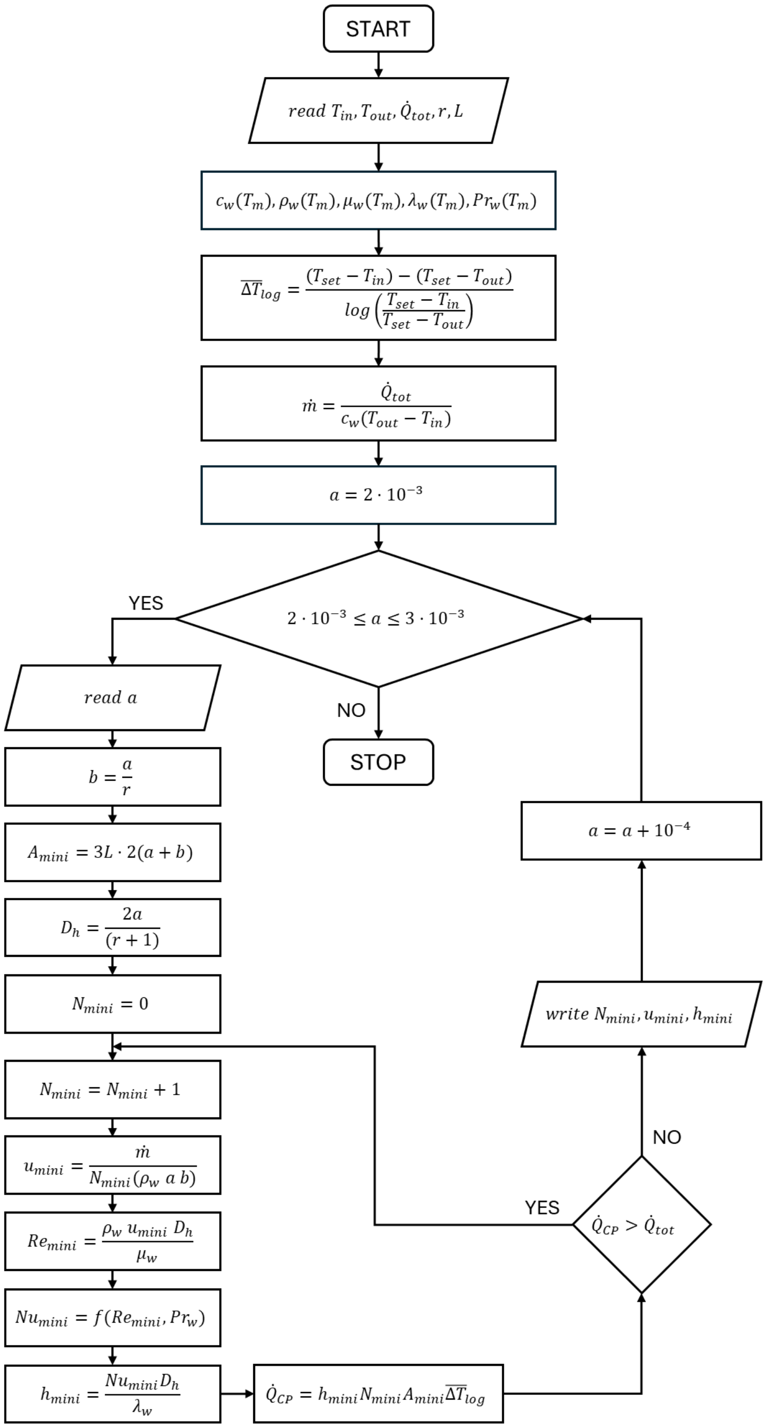

Figure IV.13 *Flow chart of the preliminary sizing procedure of the cold plate with heat sinks*

The preliminary sizing was performed considering the same inputs defined in Table IV.2. However, the inward heat through A_l changed because the enclosure interacted with the heat sink's polished aluminium surface, which has a lower emissivity. This change resulted in a limited effect on surface A_l. The contribution was reduced by 4.5 W, which equates to a 1.6% reduction of the total thermal load of the half battery pack. Due to the negligible reduction in inward heat flux through the heat sink's lateral surface, the sizes of the SCP did not change.

The flow chart presented in Figure IV.13 represents an additional step of the overall method. It differs from the previous one in the calculation of the optimal number of minichannels. The thermal load can be managed by adjusting two design variables: the cross-section and the number of minichannels. With the cross-section fixed, the goal is to identify the optimal number of minichannels that exactly dissipates the thermal load. Once the section and minichannel number that meet the load are identified, the best option must be chosen. This choice was based on the minimum water flow velocity and the Biot number *Bi*. Specifically, the optimal solution is the one that ensures a minimum velocity of 0.5 m·s^{-1} and minimises the convective heat transfer coefficient h_{mini}. Although choosing the minimum h_{mini} reduces convective heat exchange, it also lowers the Biot number to its lowest value, resulting in a more uniform temperature distribution within the battery pack.

The Nusselt number correlations for the minichannels are reported as Formula (IV.19). The first one valid for fully laminar flow in minichannels was proposed by Choi et al. (Choi, Barron and Warrington, 1991), while the second referred to a fully turbulent flow was advanced by Wu et al. (Wu and Little, 1984).

$$Nu_{mini} = \begin{cases} 0.000972\, {Re_{mini}}^{1.17} {Pr_w}^{1/3} & for\ Re_{mini} < 2000 \\ 0.00222\, {Re_{mini}}^{1.09} {Pr_w}^{0.4} & for\ Re_{mini} > 3000 \end{cases} \quad \text{(IV.19)}$$

The preliminary sizing results are reported in Table IV.6.

Table IV.6 *Cold plate with heat sinks preliminary sizing results*

Cold plate with heat sinks preliminary sizing								
D_h [mm]	a [mm]	b [mm]	N_{mini}	u_{mini} [m·s^{-1}]	Re_{mini}	Nu_{mini}	h_{mini} [W·m^{-2}K^{-1}]	$\dot{Q}_{CP}$ [W]
1.2	3	1	13	0.6	801.7	5.9	1174.0	271.2

The heat sink's width was 1 mm to limit the increase in bulk of the cold plate compared to the battery pack. The updated width of the battery pack and the heat sinks is 5.1% larger than the original configuration. For optimal thermal performance, the minichannels were positioned equidistant from each other and from the heat sinks. As Figure IV.12 (a) represents, the arrangement consisted of three rows of 3 minichannels each, followed by a final row of 4 minichannels.

IV.3.2.2 FEM verification

The FEM verification demonstrated how the heat sinks help direct the thermal load to the cold plate and then dissipate through the coolant. As in the previous case, the turbulent water flow was analysed through the Algebraic Y Model. Instead, due to the Reynolds number being lower than 2300, the flow regime of the HMCP was completely laminar. Despite that, the convective heat transfer coefficient achieved the same order of magnitude as the turbulent flow inside the serpentine.

The mesh independence analysis was performed by choosing the best grid for both configurations, achieving a percentage error of less than 1.5% between the maximum temperature spans. According to the results, the HMCP required a coarser mesh than the solution implementing the SCP. In particular, the optimal mesh for the serpentine configuration consisted of 2659396 elements, while the minichannel configuration required 626025 elements. Figure IV.14 represents the mesh independence analysis results.

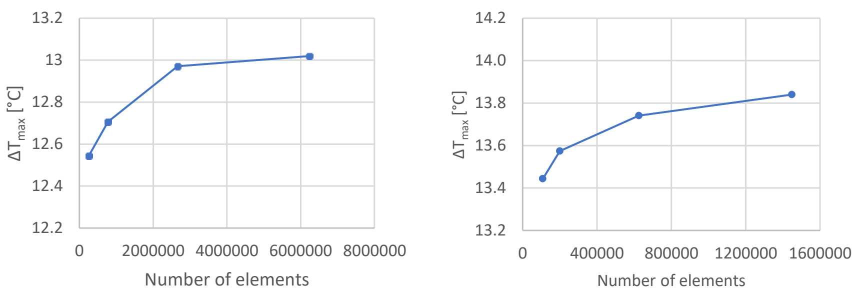

(a) (b)

Figure IV.14 *Mesh independence analysis for the SCP (a) and HMCP (b) coupled with vertical heat sinks*

The vertical heat sinks greatly enhanced heat dissipation compared to the commercial cold plate. The temperature gradients along the z-axis decreased, and the average temperature of all cells remained within the design range of 20 °C to 30 °C. The maximum temperature span was reduced in cell 3-1 by 5.3 °C for the HMCP and by 5.1 °C for the SCP. However, these temperature differences still exceeded the 5 °C limit. Figure IV.15 shows the results of the FEM verification process. The arrows in Figs. IV.15 (c) and (d) mark the water inlets and outlets.

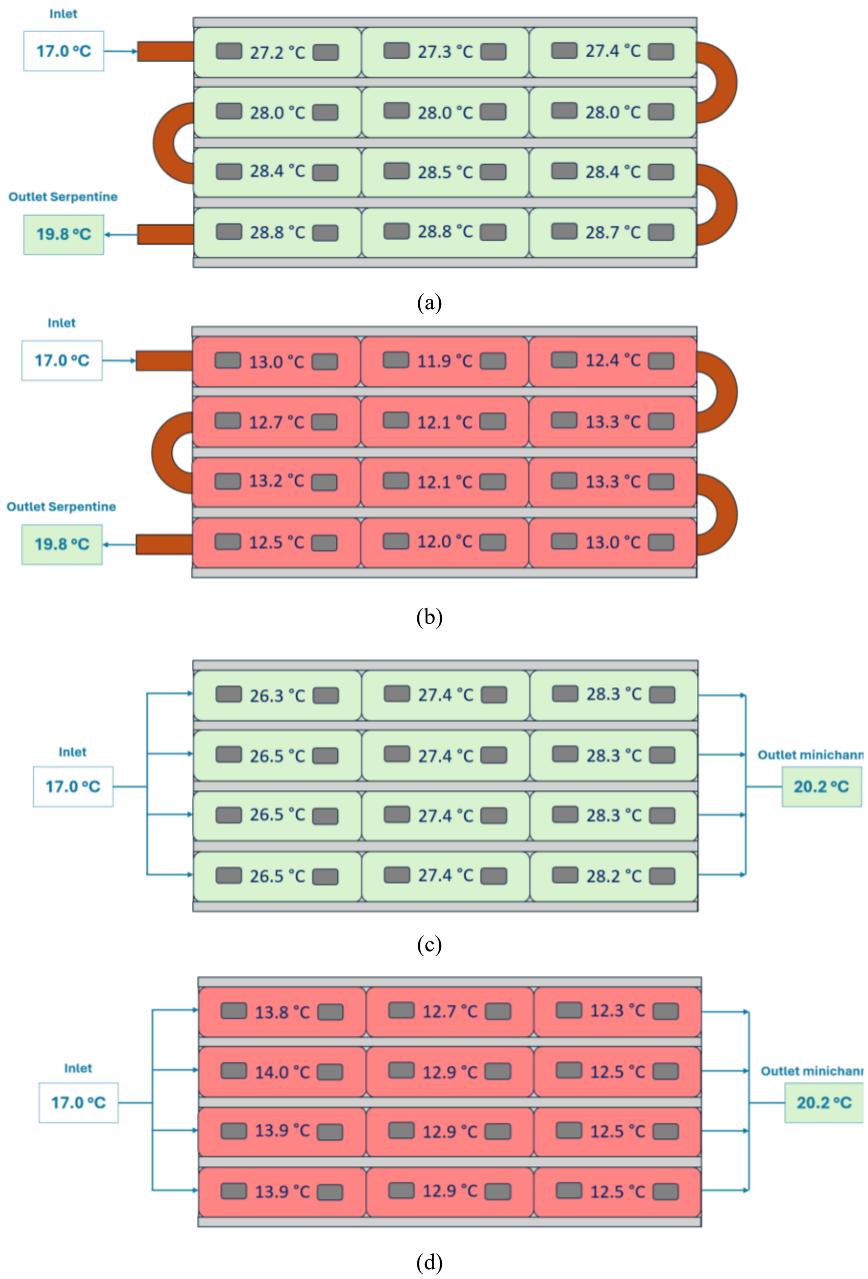

Figure IV.15 *Average temperatures (a and c) and maximum temperature spans (b and d) for the SCP and HMCP coupled with vertical heat sinks*

Figure IV.16 shows the temperature contours for the SCP and the HMCP. The picture demonstrates the efficacy of the heat sinks for both solutions. In fact, the upper body of the battery pack reaches lower temperatures compared to the commercial-type cold plate. This is the primary cause of the average temperatures and maximum temperature spans. Nevertheless, another expedient had to be found to thermally manage the upper body and further improve the temperature field uniformity along the vertical direction.

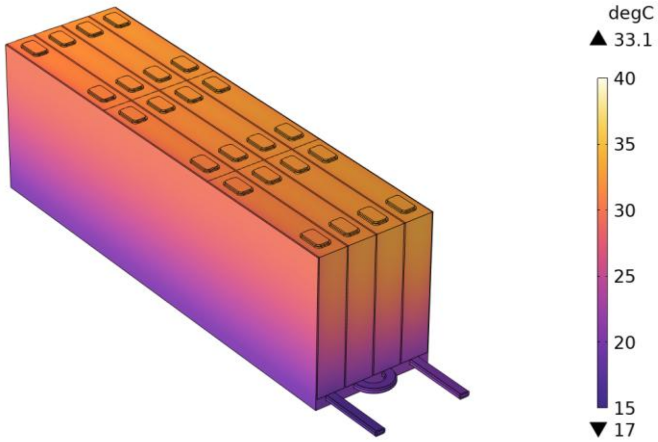

(a)

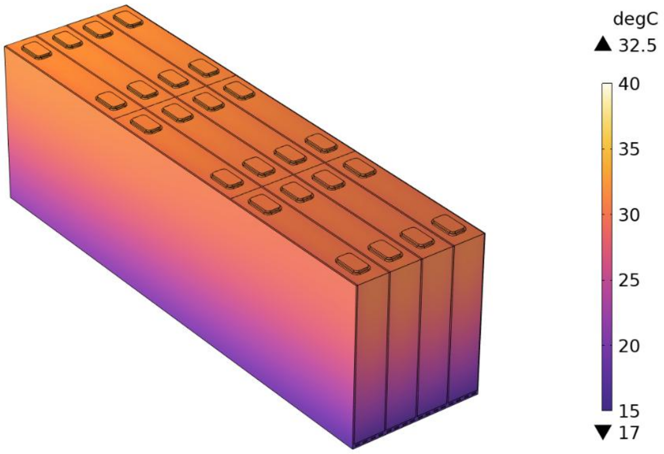

(b)

Figure IV.16 *Temperature contours of the SCP (a) and the HMCP (b) coupled with vertical heat sinks*

IV.3.3 Horizontal and vertical cold plates coupling

IV.3.3.1 Preliminary sizing

As evident in Figure IV.16, the highest temperatures were on the top of the battery pack. This information indicated that precautions were necessary to decrease the temperature of the cells on the upper body. Due to the conduction resistance of the passive heat sinks, a vertical temperature field would develop regardless of the chosen thickness. The solution to this issue was converting the passive heat sinks into active elements by implementing Vertical Cold Plates (VCPs) within the cells. The novel configuration evolved from an exclusively horizontal active cold plate to a coupled solution formed by clusters of cold plates developed on both vertical and horizontal directions. The VCPs were formed by minichannels characterised by a straight path.

Due to the addition of VCPs between each row, the thermal load was dissipated by distributing the total load among the cold plates. The choice of load distribution among the plates directly influenced the minichannel size, such as the serpentine geometry. There was no unique way to decide, as it depends on which direction should be prioritized for the heat fluxes. An initial approach involved distributing the thermal load proportionally to the heat exchange areas of the vertical and horizontal cold plates. The SCP and the HMCP were designed to remove 20% of the total heat load, while the VCPs dissipated the other 80%. The thermal load of a single row equals the total battery pack load divided by 4, corresponding to 67.3 W. The total heat load of the battery pack slightly decreases compared to the previous preliminary evaluation because, as reported in Table IV.3, the VCPs aluminium surfaces have a lower emissivity compared to the battery cells' white coating. This reduction corresponded to –2.3% of the original load.

The 80% portion of the total load assigned to the vertical plates was equally distributed among the four pairs. A pair of VCPs was thus designed to dissipate heat from a single row of cells. The sizing process was performed by applying the flow charts shown in Figs. IV.8 and IV.13 and updating the new load distribution. The distribution of loads for a pair of VCPs is schematised in Figure IV.17.

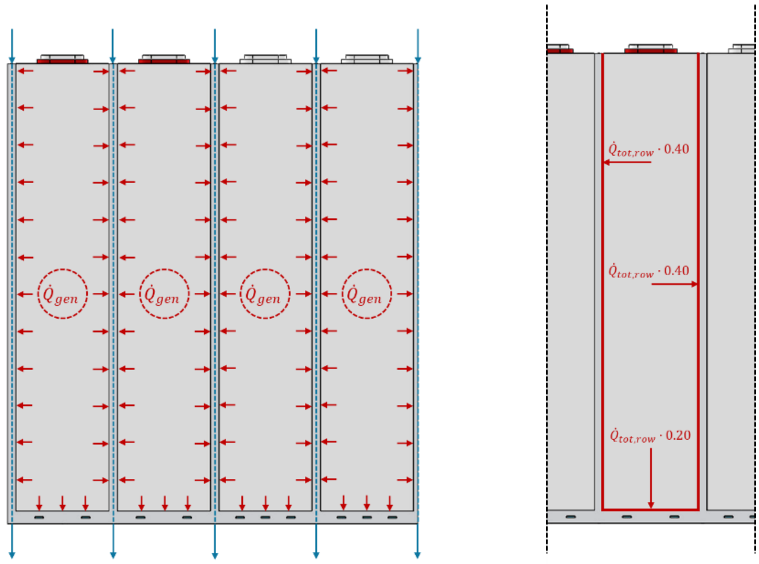

Figure IV.17 *Schematisation of the dissipated heat distribution among the cold plates (a) and a single row (b)*

The input parameters for the preliminary sizing differed from previous cases. The goal was to enhance the technical solution through several improvements. The first change involved the inlet and outlet conditions. The design inlet temperature increased from 17.0 °C to 18.5 °C. This increase was achieved by expanding the overall heat exchange surface through the addition of VCPs, which improved the thermal efficiency. While it was feasible to set an outlet temperature of 20 °C for the SCP and VCPs coupling, this was not possible for the HMCP because the required number of channels exceeded the maximum limit set by the geometric constraints. Therefore, the outlet design temperature for the rectangular minichannels was 21.5 °C.

The second change regarded the aspect ratios *r*. The lower heat load the HMCP had to dissipate (20% of the total) resulted in a low required mass flow and velocity below 0.5 $m \cdot s^{-1}$. This problem was overcome by reducing the cross-sectional area of the channels to increase fluid velocity, as required by the mass continuity equation. Consequently, the aspect ratio was changed from 3 to 5. This issue was not observed for the SCP redesign. For this reason, the copper serpentine aspect ratio was 1, while a circular cross-section was applied for the minichannels embedded in the VCPs.

The preliminary results for the horizontal cold plate serpentine, rectangular minichannels, and the straight minichannels of a single vertical cold plate are reported in Table IV.7.

Table IV.7 *Cold plate with vertical minichannels preliminary sizing results*

Horizontal and vertical cold plates preliminary sizing			
	SCP	HMCP	VCP
D_h [mm]	2.0	0.7	0.7
a [mm]	2.0	2.0	/
b [mm]	2.0	0.4	/
N	1	10	24
T_{in} [°C]	18.5	18.5	18.5
T_{out} [°C]	20.0	21.5	20.0
u [$m \cdot s^{-1}$]	1.7	0.5	0.5
Re	2677.0	359.6	318.6
h [$W \cdot m^{-2}K^{-1}$]	1277.1	658.0	1677.2
$\dot{Q}$ [W]	55.1	53.3	26.8

The arrangement of the horizontal cold plate's rectangular minichannels included two rows of 2 channels each, followed by two rows of 3 channels. In contrast, the vertical cold plate's width was increased from 1 mm for the heat sinks to 2 mm. The revised width of the battery pack and the vertical minichannels represent a 10.2% increase over the original configuration.

IV.3.3.2 FEM verification

Adopting VCPs increased the system's thermal efficiency. As indicated by the Reynolds number reported in Table IV.7, the SCP flow regime was characterised by turbulence, while the HMCP was completely laminar. In agreement with the previous FEM analysis, the chosen turbulence closure equations were applied using the Algebraic Y Model. The mesh independence analysis was conducted to identify the optimal grid for both configurations. According to Figure IV.18, the best meshes consisted of 7958247 and 12471820 elements, respectively, for the SCP and HMCP.

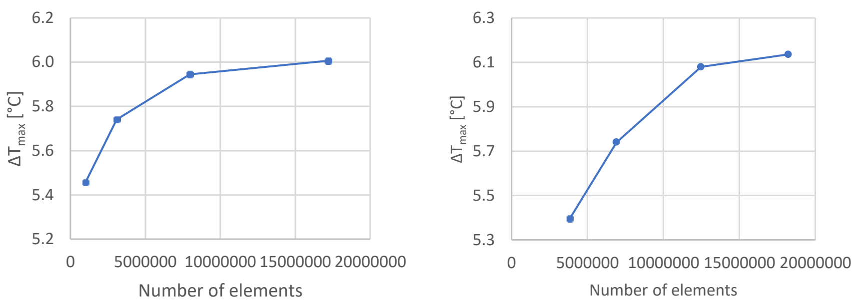

(a) (b)

Figure IV.18 *Mesh independence analysis of the SCP (a) and the HMCP (b) coupled with VCPs*

According to the results, the implementation of VCPs significantly improved the thermal efficiency of the TMS. The FEM simulations' results are reported in Figure IV.19.

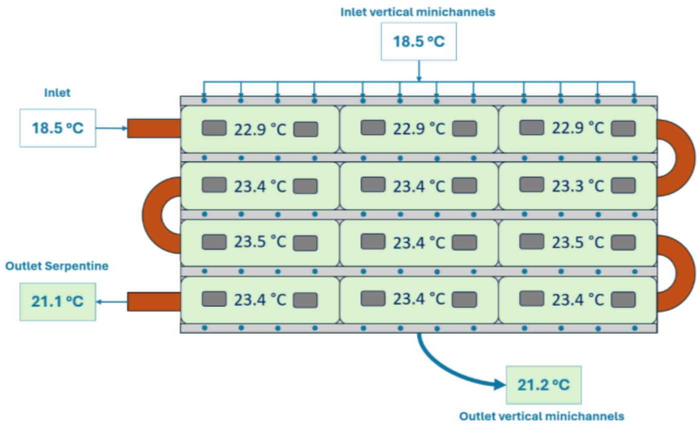

(a)

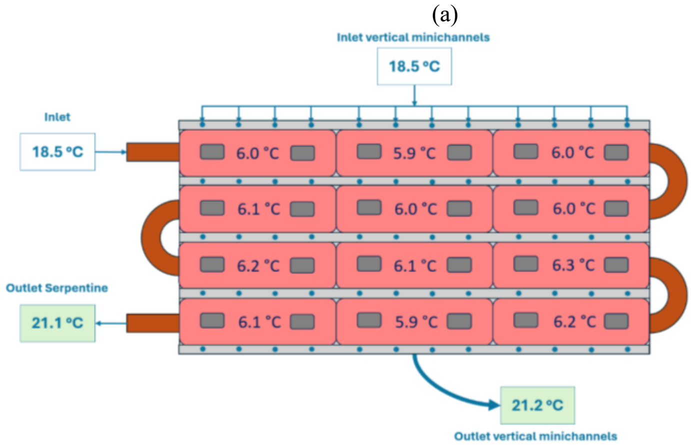

(b)

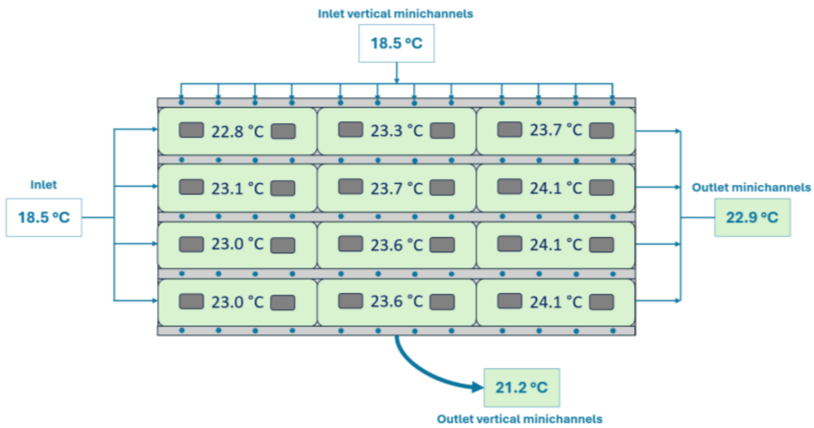

(c)

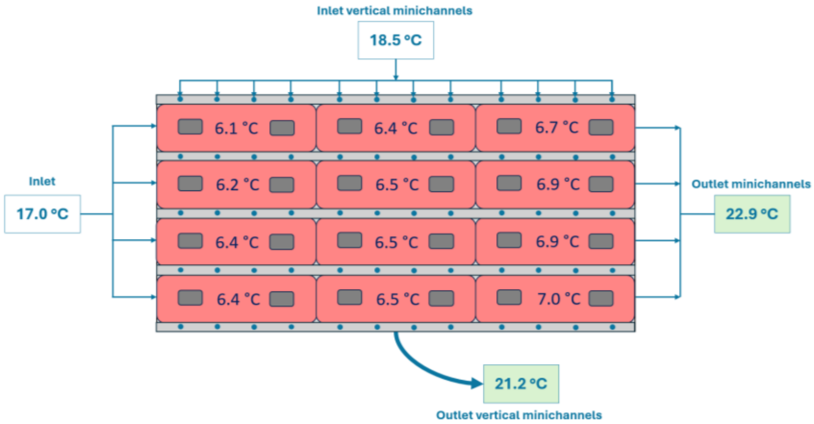

(d)

Figure IV.19 *Average temperatures (a and c) and maximum temperature spans (b and d) for the SCP and HMCP coupled with VCPs*

The average temperatures of each cell fall within the design target range defined between 20 °C and 30 °C, although they were evaluated below the set-point temperature of 25 °C. The most interesting improvement concerned the maximum internal temperature span. Every cell achieved a more uniform internal temperature field compared to the previous solution. The maximum values reached 6.3 °C and 7.0 °C for the SCP and the HMCP, respectively. This is a remarkable result because it demonstrated how the cold water interacting with the top body of the battery pack managed the hot areas. The water outlet temperatures, instead, assumed slightly higher values than the initial sizing. This may result from the thermal load distribution among the cold plates, which did not fully match the original design intent. The phenomenon could stem from the significant difference in thermal conductivities of the battery pack along the x-axis and the z-axis. The temperature contours shown in Figure IV.20 demonstrate the effectiveness of the VCPs on the upper body of the cells. The top areas experienced lower temperatures compared to the previous solution, as evinced by comparing the peak values on the temperature scales with Figure IV.16.

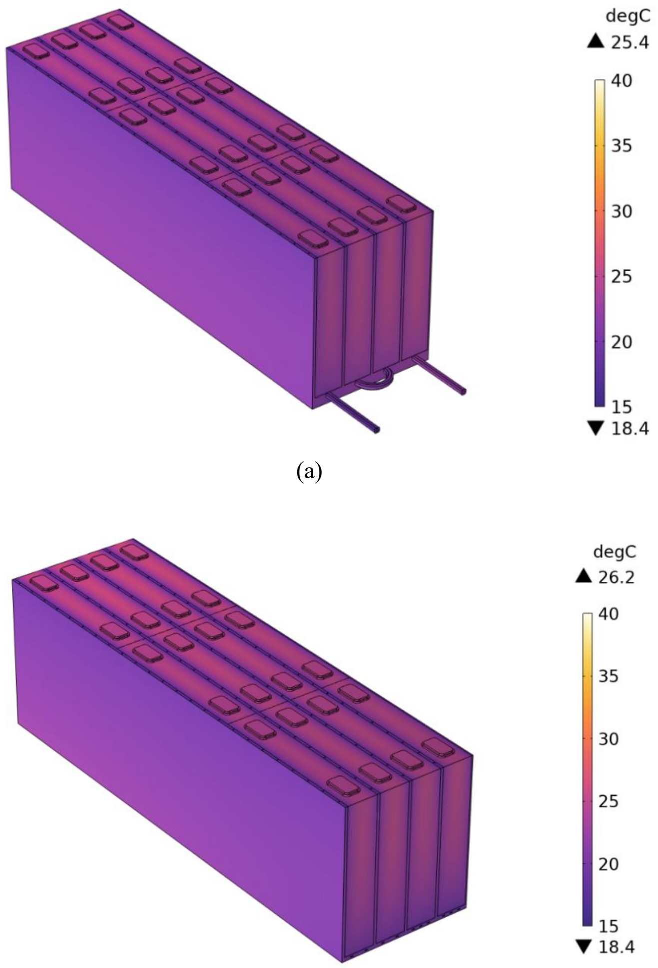

(b)

Figure IV.20 *Temperature contours of the SCP (a) and the HMCP (b) coupled with VCPs*

IV.3.4 Final configuration

IV.3.4.1 Preliminary sizing

The final configuration of the study concerns a revised version of the previous solution. The design was refined by addressing thermal features of the battery pack and practical constraints. The first consideration involved the thermal behaviour observed in the previous case. The FEM simulations revealed that the average temperature of each cell dropped below the design set-point. To restore the target temperature range, the inlet and outlet water temperatures were therefore increased to 23.0 °C and 24.0 °C, respectively.

Once the temperature issue was corrected, the thermal load distribution was re-evaluated. The previous FEM verification highlighted that the high thermal conductivity of the battery cells along the z-axis significantly lowered the conductive resistance in that direction. This imbalance resulted in the horizontal plate being underutilized, leading to non-optimal thermal uniformity across the cell surfaces. To address this, the thermal partition was revised to allocate a larger fraction of the overall heat dissipation requirement to the horizontal cold plate in the subsequent design iterations, thereby compensating for the inherent preferential heat path along the z-axis within the battery cell stack.

Lastly, as shown in Figure IV.1 (a), the electrodes are electrically connected, and no space is available above the cells. Therefore, the inlets and outlets for the vertical cold plates must be positioned both under the horizontal plate basis. To meet this requirement, a U-shaped geometry for the VCPs minichannels was adopted, arranged in groups of four. Figure IV.21 compares the previous and current configurations.

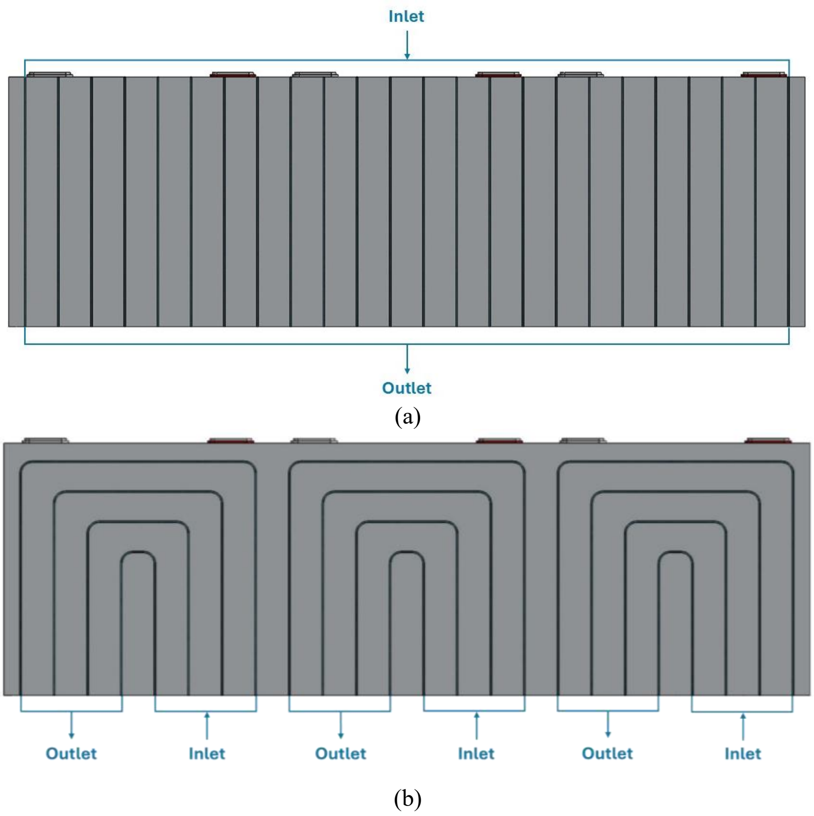

Figure IV.21 *Old (a) and new (b) arrangements of VCPs minichannels*

The manufacturing feasibility of U-shaped minichannel cold plates is increasingly supported by emerging technologies that enable the creation of complex fluid paths through architectures that traditional techniques cannot achieve. Conventional production routes generally require a two-step process where channels are machined into a substrate and then sealed with a brazed or bonded lid, a method that is largely restricted to simpler, straight geometries (Rastan *et al.*, 2020). Creating components with intricate internal bends or double-layer U-trajectories is often not feasible using these subtractive approaches. In contrast, Additive Manufacturing (AM), such as Laser-Powder Bed Fusion (Parlak, 2024), acts as an optimal solution by removing these geometric constraints. AM facilitates the production of single-piece, leak-tight cold plates with fully integrated U-shaped channels in a single build. This technology offers several critical advantages for such designs:

1. *Seamless geometry*: It permits smooth transitions and complex 3D routing without the need for separate lids or risky brazing operations that could block small channels (Chliszcz *et al.*, 2025).
2. *Integrated enhancements*: Complex internal features, such as or topology-optimized pin-fins, can be embedded directly within the U-shaped paths to maximize thermal-hydraulic performance (Ozguc *et al.*, 2025).
3. *Advanced architectures*: AM enables double-layer microchannels and integrated manifolds that significantly improve temperature uniformity across the plate (Parlak, 2024).

Although challenges such as internal surface roughness and powder removal must be managed, AM represents a transformative manufacturing route for high-performance, integrated cooling solutions that surpass the limits of traditional fabrication.

While the SCP and the HMCP needed to be redesigned as reported previously, the U-shaped minichannels introduced an additional degree of freedom, represented by the vertical spacing among them. This parameter affected the heat exchange surface between the coolant and the battery pack while keeping the same number and diameter. The optimal vertical spacing for the U-shaped channels was estimated using an iterative preliminary procedure. This process involved calculating the heat exchange surface for a single group of four U-shaped minichannels and adjusting the vertical spacing until the heat dissipation rate matched 1/3 of a single row thermal load. The flow chart, shown in Figure IV.22, has a similar structure to the previous one.

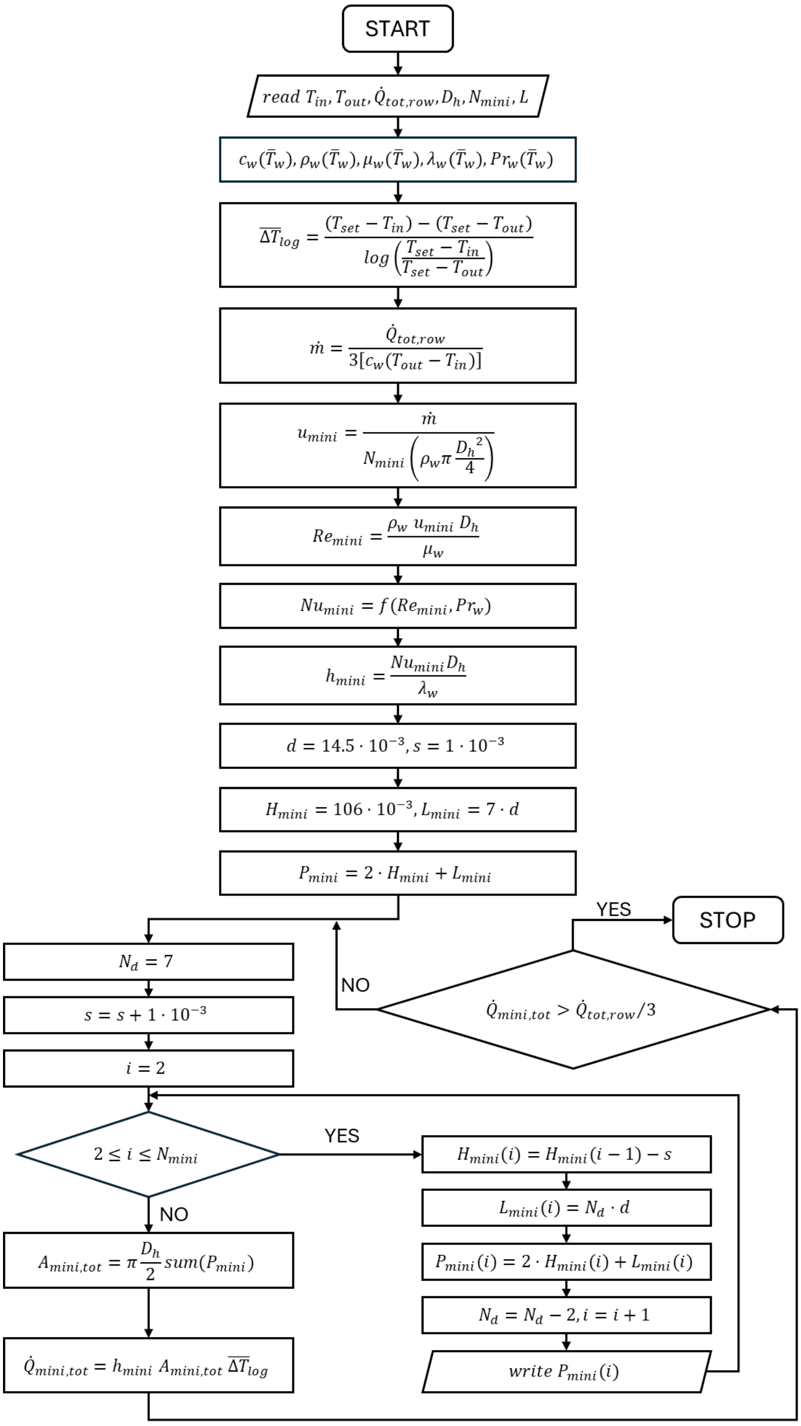

Figure IV.22 *Flow chart of the preliminary sizing procedure of the U-shaped minichannels*

N_d represents the number of spaces between the vertical sections of a single U-shaped minichannel. The term *d* indicates the step between two U-shaped minichannels, and *s* represents the vertical spacing between two minichannels. The path length of a single U-shaped minichannel was indicated as P_{mini}. The preliminary sizing results are reported in Table IV.8. The optimal spacing of the VCPs minichannels was 13 mm.

Table IV.8 *Cold plate with U-shaped minichannels preliminary sizing results*

Final configuration preliminary sizing			
	SCP	HMCP	VCP
D_h [mm]	3.0	0.7	0.7
a [mm]	3.0	2.2	/
b [mm]	3.0	0.4	/
N	1	14	12
T_{in} [°C]	23.0	23.0	23.0
T_{out} [°C]	24.0	24.0	24.0
u [$m \cdot s^{-1}$]	3.1	1.2	1.2
Re	8784.0	1242.1	923.4
h [$W \cdot m^{-2} K^{-1}$]	4205.9	2366.4	2424.5
$\dot{Q}$ [W]	87.8	87.8	7.8

IV.3.4.2 FEM verification

The requirement of lower bulk on the battery pack top partially affected the thermal efficiency of the solution. According to the results, the cells reached higher maximum temperature spans than the previous solution. The average temperature of the cells increased as expected, achieving values much closer to the design set point of 25 °C. This behaviour was observed during the mesh independence analysis, which was performed for the SCP and HCMP by applying the same turbulence closure equations and numerical models.

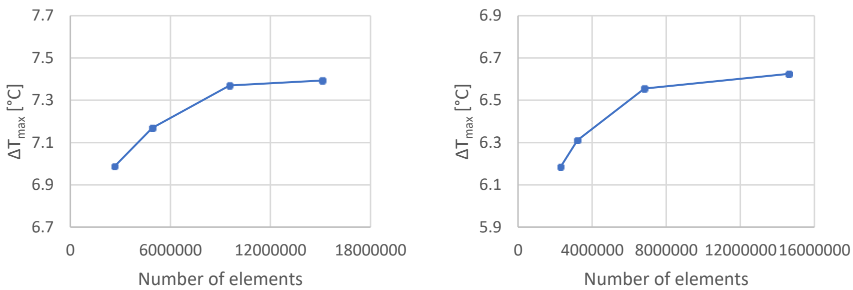

(a) (b)

Figure IV.23 *Mesh independence analysis of the SCP (a) and HMCP (b) coupled with VCPs formed by U-shaped minichannels*

As represented in Figure IV.23, the results indicated the optimal grids were formed by 9547933 and 9818966 elements, respectively, for the SCP and the HCMP.

The higher internal maximum temperature spans were produced by a different interaction between the cell's lateral surfaces and the water. While the previous case was accurately designed to allow thermal interaction between the inlet coolant flow and the warmer body of the battery pack, the U-shaped minichannels could not replicate the same condition. This was caused by the continuous increase in water temperature through the minichannels' path, which incremented the overall temperature field of the VCPs and exacerbated local heat dissipation. Moreover, the convective heat transfer coefficient correlations reported in the previous paragraphs are specifically designed for straight minichannels. Applying these formulas to minichannels characterised by curved paths may lead to lower precision due to a different velocity field than the characterisation conditions.

Figure IV.24 shows how the issue occurred in SCP by comparing the VCPs' temperature fields manifested in the current and previous minichannel arrangements. The temperature scales for both pictures were defined considering the minimum and maximum temperatures registered for each case. Figure IV.24 (b) also highlights a higher outlet temperature compared to the preliminary sizing phase, indicating a higher dissipated heat rate through the VCPs than expected.

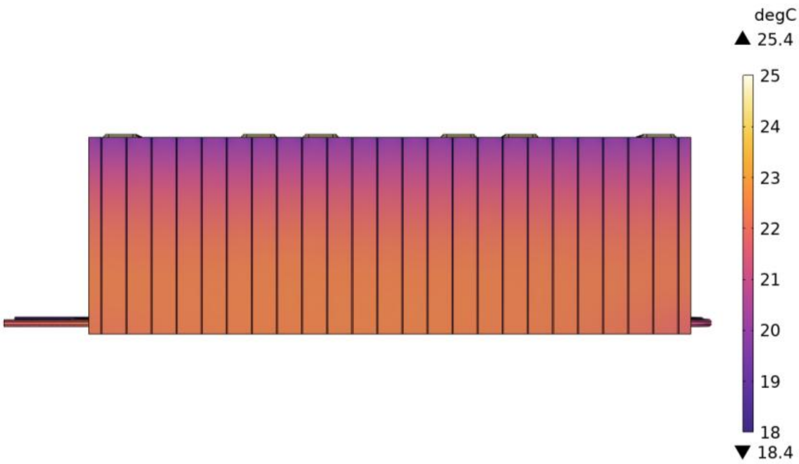

(a)

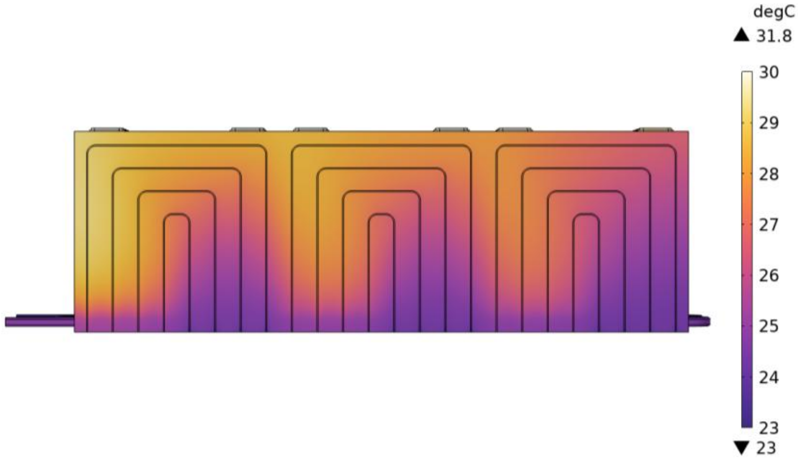

(b)

Figure IV.24 *Detailed contour comparison between the straight (a) and U-shaped (b) minichannel arrangements*

The issue was overcome by increasing the coolant velocities for both the copper serpentine and all the minichannels. The correction aimed to decrease the outlet temperature and achieve a uniform temperature field for the VCPs. According to the FEM results, the revised velocities were 4.0 $m \cdot s^{-1}$and 3.5 $m \cdot s^{-1}$ for the SCP, and 2.0 $m \cdot s^{-1}$and 3.5 $m \cdot s^{-1}$ for the HMCP (respectively referred to the horizontal cold plate channels and the U-shaped minichannels of the VCPs). Figure IV.25 reports the average temperatures and the maximum internal spans of each cell. The increments restored the optimal thermal conditions of the battery pack, achieving the target average temperature range and internal temperature spans under 5 °C for both solutions.

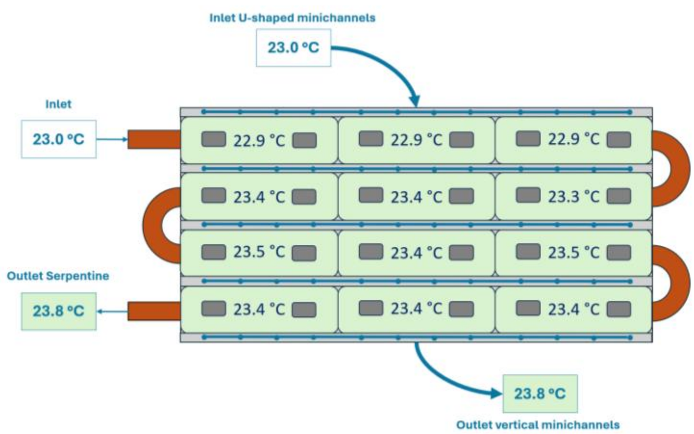

(a)

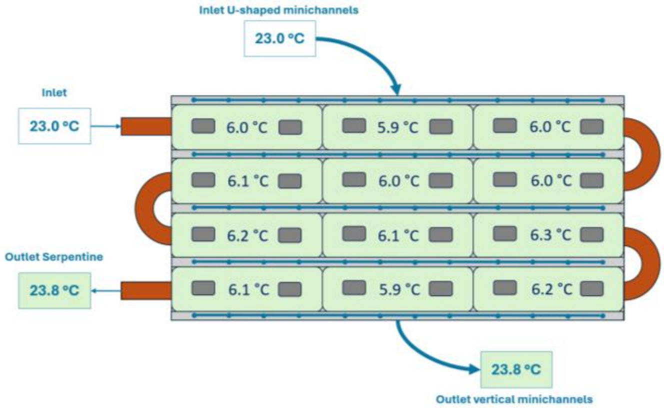

(b)

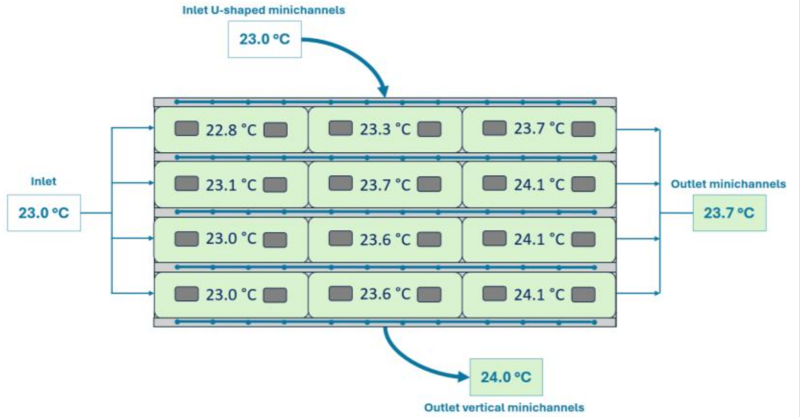

(c)

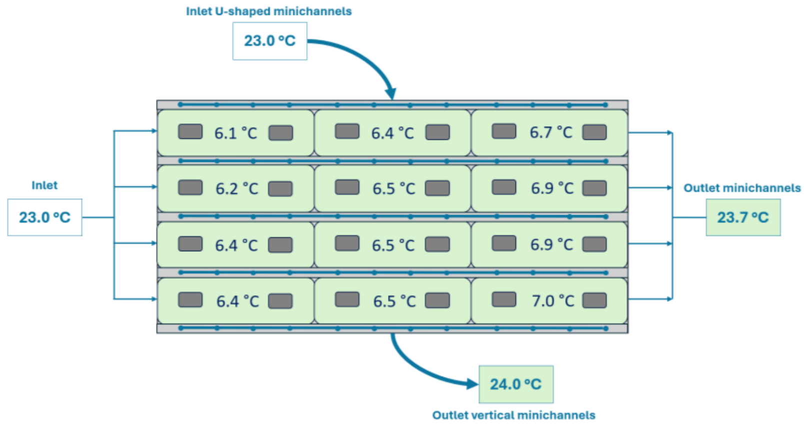

(d)

Figure IV.25 *Average temperatures (a and c) and maximum temperature spans (b and d) of the SCP and HMCP coupled with VCPs formed by U-shaped minichannels*

Increasing the mass flow was the unique option to achieve a uniform internal temperature field within the cells. The most challenging aspect was represented by low thermal conductivities, which impede a correct heat dissipation through the cold plates. However, an increment of velocity consequently produced higher pressure drops within the channels. The temperature contours of both configurations are represented in Figure IV.26.

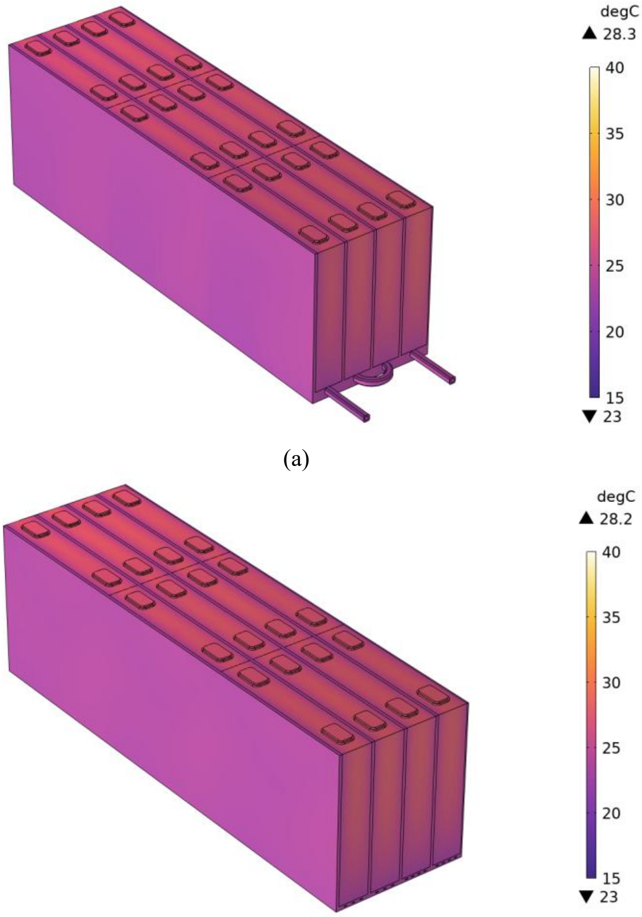

(b)

Figure IV.26 *Temperature contours of the SCP (a) and the HMCP (b) coupled with VCPs formed by U-shaped minichannels*

The optimal solution was identified by comparing the SCP and the HMCP pressure drops under optimal thermal management conditions, using corrected velocities. According to the results, the total pressure drops in the minichannels were 2.0 bar for the HMCP configuration, calculated as the sum of contributions from horizontal and vertical cold plates. In contrast, the SCP configuration exhibited total pressure drops of 3.4 bar, which is 70%

higher than the HMCP. This was despite the serpentine duct having a wider diameter compared to a single minichannel. Corrected velocities help explain this behaviour. The SCP required significantly higher velocities to achieve thermal management comparable to the HMCP, even though the minichannels have much smaller cross-sections. The benefit of the larger hydraulic diameter in the copper serpentine was offset, leading to increased pumping power requirements. Instead, the HMCP configuration resulted in a substantially more energy-efficient system.

This aspect has been further explored through an energetic analysis by comparing the required pumping power of both solutions. The study was conducted by applying a simplified approach. The channels'geometry and the fluid velocity were properly estimated using the procedures described in the previous paragraphs. The presumed pumping power was calculated as the product of the total inlet volumetric water flow by the pressure drop estimation obtained from the FEM analysis. The corresponding expression of the pumping power is given in Formula (IV.20).

$$\dot{L}_p = \left(\sum_i A_{sec,i} \, u_i \right) \Delta p \qquad \text{(IV.20)}$$

According to the results, the SCP configuration required a total pumping power of 11.4 W (including serpentine and vertical minichannels). The total pumping power required by the HMCP was 4.1 W, corresponding to a −64% lower energy demand. The energetic analysis demonstrated that the HMCP configuration is particularly effective because it has two distinct advantages:

1. *Reduced volumetric flow rate*: The total volumetric flow rate required by the HMCP corresponds to 73 $l \cdot h^{-1}$, while the SCP required a volumetric water flow of 120 $l \cdot h^{-1}$. The smaller inlet cross-sections of minichannels compared to the copper serpentine achieved this, coupled with the slower fluid flow in minichannels.
2. *Reduced pressure drops*: The FEM analysis confirmed the lower pressure drops of the minichannels compared to the copper serpentine due to the lower velocity, the straight path of horizontal minichannels, and the laminar fluid regime compared to the turbulent flow produced by the SCP.

IV.4 Bulk and weight analysis

Once the thermal and hydraulic efficiency was analysed, the study focused on investigating the additional bulk and weight caused by the implementation of heat sinks or minichannels. The previous solutions employed an aluminium cold plate, while the SCP embedded a copper serpentine. The CAD models returned information on the volume and weight of each component. The increment in size affected the height and width of the battery pack module, while the length was unchanged. Regarding the heights of horizontal cold plates, the SCP was higher than the HMCP (8 mm against 3 mm) due to the higher encumbrance of the serpentine. Consequently, there are cases where the proposed solution reaches a lower bulk and weight than the baseline cold plate. Table IV.9 reports a comprehensive comparison. Percentual variations are referred to the commercial-type cold plate dimensions.

Table IV.9 *Bulk and weight comparison referred to the commercial-type cold plate*

Bulk and weight percentage variations						
	SCP			HMCP		
	Height	Width	Weight	Height	Width	Weight
Heat sinks	0%	+5.1%	+58.7%	–4.7%	+5.1%	–18.1%
VCPs	0%	+10.2%	+109.4%	–4.7%	+10.2%	+40.1%
Final	0%	+10.2%	+111.8%	–4.7%	+10.2%	+39.6%

According to the results, the SCP solutions increase bulk and weight, especially when VCPs are employed. Instead, HMCP requires less space on the bottom plate because rectangular minichannels are shorter than serpentines. This difference entailed a reduction of less than 5% in height for all HMCP configurations. The increment in width was partially limited and did not exceed +10%. Removing the copper serpentine significantly limited the weight impact of the VCPs, while the configurations implementing heat sinks was 18.1% lighter than the commercial-type cold plate. The final HMCP configuration employing U-minichannels is 39.6% heavier than the commercial-type cold plate, corresponding to 324 grams.

IV.5 Summary of the relevant outcomes

The design process involved several configurations, initially sized using empirical correlations and then refined using Finite Element Method (FEM) simulations. The results were obtained as follows:

1. *Baseline configuration failure*: An initial commercial-type cold plate formed by a single copper serpentine failed to meet the thermal constraints. The low thermal conductivity along the battery pack's z-axis and the inward heat fluxes from the warmer enclosure resulted in an inhomogeneous internal temperature field and average temperatures exceeding the maximum threshold.
2. *Vertical heat sinks integration*: Integrating 1 mm thick vertical heat sinks partially resolved the initial issue by supporting the top thermal load dissipation through the cells' vertical surfaces. In this phase, two horizontal cold plate (SCP and HMCP) configurations were introduced and compared. FEM verification confirmed that the average temperature fell into the optimal range. The maximum

temperature span was reduced by 5.3 °C for the HMCP and 5.1 °C for the SCP in cell 3-1, representing the greatest improvement among the others. However, the unavoidable conductive thermal resistance of the heat sinks required active cooling for the top battery pack body due to the persistent vertical temperature gradients.

3. *VCPs integration*: coupling SCP and HMCP with Vertical Cold Plates (VCPs) formed by straight circular cross-section minichannels improved the battery pack temperature field uniformity. However, the maximum temperature difference of each cell exceeded the 5 °C limit, while the average temperatures deviated from the 25 °C set-point.
4. *Final optimised solution*: to resolve the obstruction of electrode connections caused by the VCPs inlet arrangement, U-shaped minichannels were properly sized and implemented into the vertical cold plates. Although this design choice slightly reduced thermal uniformity, the solution successfully achieved the thermal constraints by applying a correction to the coolant velocities determined by FEM analysis. However, the necessary correction resulted in increased pressure drops for both configurations.

The final comparison demonstrated the hydraulic superiority of the HMCP for this application. Indeed, the optimised HMCP registered a total pressure drop of 2.0 bar, while the SCP configuration registered a total pressure drop of 3.4 bar. Therefore, the pumping power required by the SCP was 70% higher than that of the HMCP solution. This finding shows that, despite the copper serpentine having a wider hydraulic diameter, the HMCP required lower coolant velocities to achieve the thermal constraints, resulting in a more energy-efficient system. An energetic analysis was performed to evaluate the pumping power required by both configurations, based on volumetric water flow and FEM-estimated pressure drops. The HMCP configuration demonstrated a significant 64% reduction in energy demand compared to the SCP (4.1 W instead of 11.4 W). This superior performance is attributed to a reduced volumetric flow rate (73 $l \cdot h^{-1}$ instead of 120 $l \cdot h^{-1}$) achieved through smaller minichannel cross-sections and slower fluid velocity, alongside lower pressure drops resulting from a straight horizontal path and a laminar fluid regime. The bulk and weight analysis estimated that VCPs increase the battery pack weight by 324 g (a +39.6% increase).

Compared with previous solutions, this weight increment is considered acceptable due to the excellent thermal management capabilities and the reduced impact on the EV's overall weight. Across various studies, modern battery electric passenger cars (from compact to midsize) commonly fall between 1.4 tons and 1.8 tons, including full-electric versions (Machedon-Pisu and Borza, 2023). Therefore, for each module, the weight increases by seven orders of magnitude from the total vehicle weight.

In conclusion, the HMCP formed by U-shaped vertical minichannels represented the best optimised solution, finding the best trade-off between thermal efficiency, size, encumbrance, and energy demand. Figure IV.27 illustrates the general arrangement of the battery pack and the cold plate system, including overall dimensions.

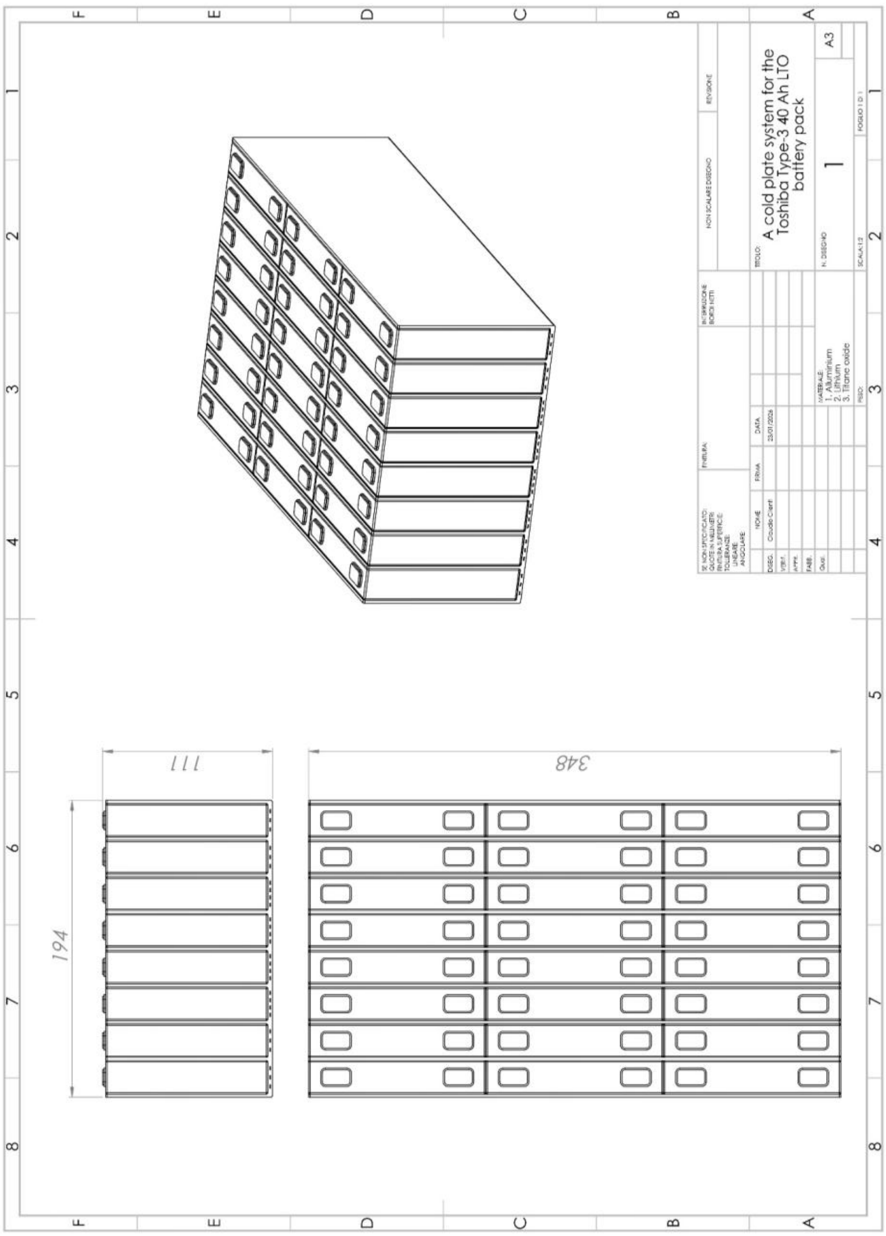

Figure IV.27 *Cold plate system final optimised configuration*

Chapter V
Conclusions

The scope of this thesis focused on developing efficient Thermal Management Systems (TMSs) for Electric Vehicles (EVs) in commercial applications. After analysing current technologies in the literature, the work aimed to bridge the gap between academic research and primary solutions in the electric transport market. A simplified thermal model, directly applicable to industry, was proposed to understand the thermal behaviour of Li-ion battery cells subjected to any current profiles in natural convection. The results identified the thermal loads of Li-ion battery cells and their temperature increment over time due to internal heat generation. The subsequent analysis investigated the development of a novel liquid-based cold plate system made of vertical and horizontal minichannels. The design was based on the Toshiba Type-3 20, commonly used in EVs with high-power battery packs. Practical considerations included boundary thermal conditions of the battery pack and international standards (IEC 62660-1:2010), which were essential for calculating inward heat fluxes during normal operating conditions. The State of the Art reviewed recent TMS developments by academia, and compared various coolants and substances (such as air, liquids, refrigerants, and Phase Change Materials). Despite advancements, the automotive and railway industries continue to favour liquid-based TMSs for their reliability and readiness. Most electric vehicles on the market employ indirect cooling strategies with water and glycol mixtures as secondary fluids. HVAC systems are actively integrated to regulate water temperature flowing to the battery pack, electric motor, and other components. Tesla's innovative system enables five different thermal management strategies based on environmental conditions and waste heat recovery from the powertrain, utilizing the octovalve (an eight-port rotary valve) that activates different branches of the secondary loop depending on the mode. The *BMW i3* was among the first commercial vehicles to implement a refrigerant-based TMS. However, the subsequent *BMW i4 eDrive40* demonstrated that indirect liquid cooling remains the optimal solution in the automotive industry. Regarding electric trains, most BEMUs proposed by leading railway industry players employ indirect liquid cooling strategies. This review highlights that electric transport companies regard liquid-based TMSs as the most reliable and promising technology for future development. This insight guided the research approach in this thesis, which focused on designing an innovative liquid-based TMS through a numerical approach. This choice was the first step, aiming to bridge the gap between industry and academia.

The simplified thermal model in Chapter III aids in thermally characterizing Li-ion battery cells in natural convection, which is preferred because it reflects the batteries' intrinsic nature without external cooling influences that limit temperature rise. The model was applied to a 18650 LTO cylindrical cell with a nominal capacity and voltage of 1500 mAh and 2.4 V. Thermal parameters were obtained from literature, based on typical ranges reported in research articles and reviews. The workflow consisted of four main steps: the Equivalent Circuit Model (ECM), internal heat generation rate modelling, empirical correlations of the Nusselt number, and the implementation of the general heat conduction equation. The electrical parameters of the ECM were experimentally determined through HPPC tests. Several trends showed dependency on state of charge (SOC), which was incorporated into the Bernardi et al. equation for internal heat generation. Using empirical correlations significantly reduced computational costs compared to CFD analysis, while maintaining reliability and affordability. To better characterize convective heat exchange around the cell, three correlations (developed by Churchill and Chu, Morgan, and Kuhen and Goldstein) were used. The research employed two different current profiles, simulating full and partial discharges at 1C. Results showed the LTO cell remained below the maximum threshold temperature of 35°C, with temperature uniformity due to the low Biot number ($Bi \ll 1$), regardless of the correlation used. Experimental validation confirmed that the methodology provides accurate results when Li-ion cells undergo multiple charge and discharge cycles. A thermal camera (accuracy ±1.5 °C) measured the cell's average temperature. The percentage errors between numerical and experimental results were within ±5%, and the root mean square errors (RMSE) exceeded 95%, indicating excellent agreement. The subsequent CFD analysis supported the reliability of the simplified model by identifying which empirical correlation best suited cylindrical Li-ion cells during continuous cycling. Morgan's correlation was suitable for simulations under 500 seconds, while Churchill and Chu's was better for longer durations.

Chapter IV detailed the core research of the thesis, focusing on enhancing thermal dissipation from the battery pack to the coolant using an optimised, innovative cold plate system. Temperature targets were set within the safe range of 20 – 30°C, with internal temperature gradients limited to 5°C per cell, while minimising pumping power. The low thermal conductivities of the Toshiba SCiB prismatic LTO cell, especially along the x-axis, posed significant challenges. The modelling approach from Chapter III was crucial in estimating maximum internal heat generation and defining the primary thermal loads. However, a comprehensive approach was needed for inward heat fluxes. Estimates showed boundary inward contributions accounted for nearly 10% of the total thermal load. The iterative design process revealed the limitations of commercial serpentine cold plates, which often fail to maintain internal temperature uniformity due to low vertical thermal conductivity. An initial attempt involved vertical heat sinks that transferred heat horizontally, reducing vertical gradients. Two horizontal cold plate designs (SCP and HMCP) were developed and analysed using the Finite Element Method (FEM). Results showed that average temperatures remained within the ideal operating range. Cell 3-1 experienced the most significant improvement, with the HMCP and SCP reducing the maximum temperature spread by 5.3°C and 5.1°C, respectively. Despite these improvements, vertical temperature gradients persisted due to conductive thermal resistance, necessitating active cooling in the upper section of the battery pack. Circular cross-section minichannel VCPs improved temperature uniformity, keeping maximum spans below 7°C per cell. However, the electrode connection obstructions made this option less reliable. Although U-shaped minichannels reduced thermal efficiency, they offered an optimal compromise between heat dissipation and obstruction management. Increasing water velocity within minichannels was the standpoint for reaching temperature targets, despite higher pressure drops. The optimized HMCP had a total pressure drop of 2.0 bar, while the SCP registered 3.4 bar. As a result, the SCP's required pumping power was 70% higher than the HMCP's. These findings suggest that, despite the larger hydraulic diameter of the copper serpentine, the HMCP required lower coolant velocities to meet its thermal needs, making it more energy efficient. Lower coolant velocities and pressure drops result in lower energy demand from the TMS, reducing the overall energy consumption of the vehicle when comparing SCP and HMCP. Volume and weight analyses indicated that VCPs increased the battery pack weight by 324 g. Although the weight increased by 39.6% higher than the commercial-type cold plate, the impact on the total mass of the vehicle is negligible. The volume increase was minimal, as the horizontal plate was 5 mm shorter than the baseline, and the width increased by only 9 mm (+10.1%). Ultimately, the HMCP with U-shaped vertical minichannels proved to be the best design, offering an optimal balance of thermal performance, size, and energy consumption.

The findings of this research open several promising avenues for future investigation, aimed at further bridging the gap between theoretical modelling and industrial implementation. These developments can be categorised into four primary areas:

1. *Integration of the simplified model into industrial tools*: The ECM model developed in this thesis has demonstrated significant potential for integration into industrial software tools. Its implementation can potentially provide rapid predictions of the thermal behaviour of Li-ion cells under arbitrary current profiles, enabling the identification of thermal criticalities before the physical prototyping of a cooling system. However, the effectiveness of this tool is strictly dependent on a robust characterization via Hybrid Pulse Power Characterization (HPPC) tests. Consequently, a fundamental step forward would be the creation of extensive databases containing circuit parameters as a function of the State of Charge for various cell formats (prismatic, cylindrical, and pouch). A closer synergy between battery manufacturers and the EV industry is essential to standardise and optimise the design processes.
2. *Implementation of Thermal Topology Optimisation (TTO)*: Despite the demonstrated efficiency of the proposed cold plate system, the pressure drops exceeding 1.0 bar remain a challenge compared to conventional serpentine designs. Leveraging the design freedom offered by Additive Manufacturing (AM), topology optimization algorithms can be employed to redefine minichannel geometries. This would aim to maintain high thermal performance while significantly reducing hydraulic resistance. Novel minichannel geometries must be investigated, as U-shaped designs present challenges when positioning the inlet and outlet at the top of the VCPs. This is due to the physical constraints imposed by the electrodes, which prevent the placement of manifolds at the top of the battery pack. Furthermore, implementing horizontal U-shaped channels would inevitably result in higher pressure drops, given the greater distance the coolant would have to travel to flow from the inlet to the outlet section.
3. *Two-phase heat exchange*: Shifting from single-phase liquids to two-phase refrigerants offers a paradigm shift in efficiency. The latent heat of evaporation ensures thermal uniformity across both horizontal and vertical plates, effectively eliminating the temperature gradient between inlet and outlet without necessitating excessive flow rates.
4. *Industrial prototyping of hybrid TMS*: A more disruptive frontier involves the development of hybrid TMSs through the integration of Heat Pipes or composite Phase Change Materials. Although such solutions require substantial research and development investment, their potential for high-power applications is immense. The inclusion of PCMs would allow the system to passively manage thermal peaks during ultra-fast charging or high-discharge cycles, reducing the immediate load on the active pumping system. This

hybrid approach represents a sophisticated evolution toward more resilient and energy-efficient thermal management architectures for next-generation electric transport.

References

Airò Farulla, G. *et al.* (2023) “Optimal design of lithium ion battery thermal management systems based on phase change material at high current and high environmental temperature,” *Thermal Science and Engineering Progress*, 42. Available at: https://doi.org/10.1016/j.tsep.2023.101862.

Akinlabi, A.A.H. and Solyali, D. (2020a) “Configuration, design, and optimization of air-cooled battery thermal management system for electric vehicles: A review,” *Renewable and Sustainable Energy Reviews*. Elsevier Ltd. Available at: https://doi.org/10.1016/j.rser.2020.109815.

Akinlabi, A.A.H. and Solyali, D. (2020b) “Configuration, design, and optimization of air-cooled battery thermal management system for electric vehicles: A review,” *Renewable and Sustainable Energy Reviews*. Elsevier Ltd. Available at: https://doi.org/10.1016/j.rser.2020.109815.

Al-Ahmed, A. *et al.* (2020) “Thermal energy storage and thermal conductivity properties of fatty acid/fatty acid-grafted-CNTs and fatty acid/CNTs as novel composite phase change materials,” *Scientific Reports*, 10(1). Available at: https://doi.org/10.1038/s41598-020-71891-1.

Alipanah, M. and Li, X. (2016) “Numerical studies of lithium-ion battery thermal management systems using phase change materials and metal foams,” *International Journal of Heat and Mass Transfer*, 102, pp. 1159–1168. Available at: https://doi.org/10.1016/j.ijheatmasstransfer.2016.07.010.

Anisha and Kumar, A. (2023a) “Identification and Mitigation of Shortcomings in Direct and Indirect Liquid Cooling-Based Battery Thermal Management System,” *Energies*. MDPI. Available at: https://doi.org/10.3390/en16093857.

Anisha and Kumar, A. (2023b) “Identification and Mitigation of Shortcomings in Direct and Indirect Liquid Cooling-Based Battery Thermal Management System,” *Energies*. MDPI. Available at: https://doi.org/10.3390/en16093857.

Ankathi, S. *et al.* (2024) “Well-to-wheels analysis of greenhouse gas emissions for passenger vehicles in Middle East and North Africa,” *Journal of Industrial Ecology*, 28(4), pp. 800–812. Available at: https://doi.org/10.1111/jiec.13500.

Árpád, I.W., Kiss, J.T. and Kocsis, D. (2024) "Role of the volume-specific surface area in heat transfer objects: A critical thinking-based investigation of Newton's law of cooling," *International Journal of Heat and Mass Transfer*, 227. Available at: https://doi.org/10.1016/j.ijheatmasstransfer.2024.125535.

Awan, U.S. *et al.* (2025) "Cell geometry influences on the vibration performance of lithium-ion batteries," *Journal of Energy Storage*, 109, p. 115227. Available at: https://doi.org/https://doi.org/10.1016/j.est.2024.115227.

Awasthi, A., Nirmalkar, N. and Tiwari, A.K. (2025) "A review of PCM based hybrid battery thermal management systems for the prismatic lithium-ion batteries of the electric vehicle," *Future Batteries*, 5, p. 100035. Available at: https://doi.org/https://doi.org/10.1016/j.fub.2025.100035.

Baazouzi, S. *et al.* (2023) "Design, Properties, and Manufacturing of Cylindrical Li-Ion Battery Cells—A Generic Overview," *Batteries*, 9(6). Available at: https://doi.org/10.3390/batteries9060309.

Bai, Q. *et al.* (2023) "Influence of Insulation Material Thickness on Spread of Thermal Runaway in Battery Packs," *Processes*, 11(5). Available at: https://doi.org/10.3390/pr11051321.

Behi, H. *et al.* (2020a) "Thermal management analysis using heat pipe in the high current discharging of lithium-ion battery in electric vehicles," *Journal of Energy Storage*, 32. Available at: https://doi.org/10.1016/j.est.2020.101893.

Behi, H. *et al.* (2020b) "Thermal management analysis using heat pipe in the high current discharging of lithium-ion battery in electric vehicles," *Journal of Energy Storage*, 32. Available at: https://doi.org/10.1016/j.est.2020.101893.

Behi, H. *et al.* (2021) "Heat pipe air-cooled thermal management system for lithium-ion batteries: High power applications," *Applied Thermal Engineering*, 183. Available at: https://doi.org/10.1016/j.applthermaleng.2020.116240.

Bernardi, D., Pawlikowski, E. and Newman, J. (1985) "A General Energy Balance for Battery Systems," *Journal of Electrochemical Society* , 132. Available at: https://doi.org/10.1149/1.2113792.

Blasius, H. (1913) "Das Aehnlichkeitsgesetz bei Reibungsvorgängen in Flüssigkeiten," *Mitteilungen über Forschungsarbeiten auf dem Gebiete des Ingenieurwesens: insbesondere aus den Laboratorien der technischen Hochschulen*. Berlin, Heidelberg: Springer Berlin Heidelberg, pp. 1–41. Available at: https://doi.org/10.1007/978-3-662-02239-9_1.

Blenkinsop, P. (2025) "EU drops 2035 combustion engine ban as global EV shift faces reset," *Reuters*.

Bobobee, E.D. *et al.* (2023) "State of charge estimation of ternary lithium-ion batteries at variable ambient temperatures," *International Journal of*

Electrochemical Science, 18(4). Available at: https://doi.org/10.1016/j.ijoes.2023.100062.

Boev, P. *et al.* (2023) "First Passenger Operation of a State-of-the-art Battery-Electric Multiple Unit (BEMU) in Germany," *Transportation Research Procedia*, 72, pp. 2510–2517. Available at: https://doi.org/https://doi.org/10.1016/j.trpro.2023.11.757.

Boyd (no date) *CP10/CP12/CP15 Tubed Cold Plates Lytron Datasheet*. Available at: https://shop.amstechnologies.com/CP10-CP12-CP15-Tubed-Cold-Plates/SW10851 (Accessed: November 17, 2025).

Bryden, T.S. *et al.* (2018) "Methodology to determine the heat capacity of lithium-ion cells," *Journal of Power Sources*, 395, pp. 369–378. Available at: https://doi.org/10.1016/j.jpowsour.2018.05.084.

Buberger, J. *et al.* (2022) "Total CO2-equivalent life-cycle emissions from commercially available passenger cars," *Renewable and Sustainable Energy Reviews*, 159. Available at: https://doi.org/10.1016/j.rser.2022.112158.

Cai, F. *et al.* (2022) "A rapid self-heating strategy of lithium-ion battery at low temperatures based on bidirectional pulse current without external power," *Journal of Power Sources*, 549, p. 232138. Available at: https://doi.org/https://doi.org/10.1016/j.jpowsour.2022.232138.

Cai, F. *et al.* (2024) "Experimental study on self-heating strategy of lithium-ion battery at low temperatures based on bidirectional pulse current," *Applied Energy*, 354, p. 122232. Available at: https://doi.org/https://doi.org/10.1016/j.apenergy.2023.122232.

Calvagna, C. *et al.* (2022) "Development of a novel probe for measuring emissivity and temperature during Raman spectroscopy," *Journal of Physics: Conference Series*. Institute of Physics. Available at: https://doi.org/10.1088/1742-6596/2204/1/012068.

Cataldi, M. *et al.* (2024) "Balancing cleaner energy and geopolitical interests in the complex transition of the European electricity mix: from Fukushima to the Ukraine war," *Discover Energy*, 4(1). Available at: https://doi.org/10.1007/s43937-024-00026-8.

Cen, J., Li, Z. and Jiang, F. (2018) "Experimental investigation on using the electric vehicle air conditioning system for lithium-ion battery thermal management," *Energy for Sustainable Development*, 45, pp. 88–95. Available at: https://doi.org/10.1016/j.esd.2018.05.005.

Cengel, Y.A. (2022) *Heat Transfer: a Pratical Approach*. 2nd Edition. New York: McGraw-Hill.

Chang, C. *et al.* (2021) "3D printed aluminum flat heat pipes with micro grooves for efficient thermal management of high power LEDs," *Scientific Reports*, 11(1). Available at: https://doi.org/10.1038/s41598-021-87798-4.

Chen, B.H. *et al.* (2023) "Establishment of second-order equivalent circuit model for bidirectional voltage regulator converter: 48 V-aluminum-ion battery pack," *Energy Reports*, 9, pp. 2629–2637. Available at: https://doi.org/10.1016/j.egyr.2023.01.086.

Chen, H.Y. and Chen, C. (2016) "Determining the emissivity and temperature of building materials by infrared thermometer," *Construction and Building Materials*, 126, pp. 130–137. Available at: https://doi.org/10.1016/j.conbuildmat.2016.09.027.
Chen, L. *et al.* (2025) "Mitigation of cylindrical lithium ion battery thermal runaway propagation with a flame retardant polypropylene thermal barrier," *Journal of Energy Storage*, 108. Available at: https://doi.org/10.1016/j.est.2024.115042.
Chen, W. *et al.* (2022) "Numerical Analysis of Novel Air-Based Li-Ion Battery Thermal Management," *Batteries*, 8(9). Available at: https://doi.org/10.3390/batteries8090128.
Chen, Z. *et al.* (2023) "Study on heat-exchange efficiency and energy efficiency ratio of a deeply buried pipe energy pile group considering seepage and circulating-medium flow rate," *Renewable Energy*, 216. Available at: https://doi.org/10.1016/j.renene.2023.119020.
Chliszcz, K. *et al.* (2025) "Assessment of the Feasibility of Using Additive Manufacturing from Metal Powder to Produce Compact Heat Exchangers," *Materials*, 18(13). Available at: https://doi.org/10.3390/ma18133035.
Choi, S.B., Barron, R.F. and Warrington, R.Q. (1991) "Fluid flow and heat transfer in microtubes, in micro-mechanical sensors," *Actuators Syst. ASME DSC*, 32, pp. 121–128.
Chudy-Laskowska, K. and Pisula, T. (2022) "An Analysis of the Use of Energy from Conventional Fossil Fuels and Green Renewable Energy in the Context of the European Union's Planned Energy Transformation," *Energies*, 15(19). Available at: https://doi.org/10.3390/en15197369.
Churchill, S.W. and Chu, H.H.S. (1975) *Correlating equations for laminar and turbulent free convection from a horizontal cylinder*, *ht. J. Heat Mass Transfer*.
Colbertaldo, P., Guandalini, G. and Campanari, S. (2018) "Modelling the integrated power and transport energy system: The role of power-to-gas and hydrogen in long-term scenarios for Italy," *Energy*, 154, pp. 592–601. Available at: https://doi.org/https://doi.org/10.1016/j.energy.2018.04.089.
Cui, S. and Zhao, N. (2024) "A Study on the Current Status and Future Prospects of EV Automotive Market," *Journal of Social Science and Cultural Development*, 1. Available at: https://doi.org/10.70767/jsscd.v1i2.296.
Dardiri, A.S.H. *et al.* (2024) "Indirect Liquid Cooling for Battery Thermal Management: A Review," *International Journal of Integrated Engineering*, 16(2), pp. 153–163. Available at: https://doi.org/10.30880/ijie.2024.16.02.016.
Daroń, M. and Wilk, M. (2021) "Management of energy sources and the development potential in the energy production sector—a comparison of eu countries," *Energies*, 14(3). Available at: https://doi.org/10.3390/en14030685.

Deng, D. *et al.* (2021) "An improved second-order electrical equivalent modeling method for the online high power Li-ion battery state of charge estimation," *Proceedings of the Energy Conversion Congress and Exposition - Asia, ECCE Asia 2021*. Institute of Electrical and Electronics Engineers Inc., pp. 1725–1729. Available at: https://doi.org/10.1109/ECCE-Asia49820.2021.9479017.

Deng, J. *et al.* (2024) "Research on the natural circulation characteristic of deep borehole heat exchanger and the influences on the water circulation resistance," *Building Simulation*, 17(12), pp. 2213–2232. Available at: https://doi.org/10.1007/s12273-024-1202-x.

Deng, Y. *et al.* (2018) "Effects of different coolants and cooling strategies on the cooling performance of the power lithium ion battery system: A review," *Applied Thermal Engineering*. Elsevier Ltd, pp. 10–29. Available at: https://doi.org/10.1016/j.applthermaleng.2018.06.043.

El Diasty, R., Faziot, P. and Budaiwlj, I. (1993) *Dynamic Modelling of Moisture Absorption and Desorption in Buildings*, *Building and Environment*.

Driving electric (2022) *Nissan Leaf replacement will be a crossover SUV*. Available at: https://www.drivingelectric.com/nissan/leaf/41411/nissan-leaf-replacement-will-be-a-crossover-suv (Accessed: July 2, 2023).

Du, S. *et al.* (2017) "An investigation of irreversible heat generation in lithium ion batteries based on a thermo-electrochemical coupling method," *Applied Thermal Engineering*, 121, pp. 501–510. Available at: https://doi.org/10.1016/j.applthermaleng.2017.04.077.

Edmondson, J. (2023) *Thermal Management for Electric Vehicles 2023-2033*. Available at: https://www.idtechex.com/en/research-report/thermal-management-for-electric-vehicles-2023-2033/909 (Accessed: October 12, 2023).

Erhan, K. and Özdemir, E. (2021) "Prototype production and comparative analysis of high-speed flywheel energy storage systems during regenerative braking in hybrid and electric vehicles," *Journal of Energy Storage*, 43. Available at: https://doi.org/10.1016/j.est.2021.103237.

European Parliament (2022) *EU ban on sale of new petrol and diesel cars from 2035 explained*. Available at: https://www.europarl.europa.eu/news/en/headlines/economy/20221019STO44572/eu-ban-on-sale-of-new-petrol-and-diesel-cars-from-2035-explained (Accessed: February 13, 2023).

Fan, Y. *et al.* (2024) "An optimal self-heating strategy for lithium-ion batteries with pulse-width modulated self-heater," *Journal of Energy Storage*, 76, p. 109650. Available at: https://doi.org/https://doi.org/10.1016/j.est.2023.109650.

Forsberg, C., Dale, B.E. and Ingersoll, E. (2024) "Replacing All Fossil Fuels With Nuclear-Enabled Hydrogen, Cellulosic Hydrocarbon Biofuels, and

Dispatchable Electricity," *ASME Open Journal of Engineering*, 3. Available at: https://doi.org/10.1115/1.4064592.
Forsberg, C.W. *et al.* (2021) "Replacing liquid fossil fuels and hydrocarbon chemical feedstocks with liquid biofuels from large-scale nuclear biorefineries," *Applied Energy*, 298, p. 117225. Available at: https://doi.org/https://doi.org/10.1016/j.apenergy.2021.117225.
Fragiacomo, P. *et al.* (2022) "Sizing and Performance Analysis of Hydrogen- and Battery-Based Powertrains, Integrated into a Passenger Train for a Regional Track, Located in Calabria (Italy)," *Energies*, 15(16). Available at: https://doi.org/10.3390/en15166004.
Gan, Y. *et al.* (2020) "Development of thermal equivalent circuit model of heat pipe-based thermal management system for a battery module with cylindrical cells," *Applied Thermal Engineering*, 164. Available at: https://doi.org/10.1016/j.applthermaleng.2019.114523.
Gao, F. *et al.* (2020) "A review on materials for flame retarding and improving the thermal stability of lithium ion batteries," *International Journal of Electrochemical Science*, 15(2), pp. 1391–1411. Available at: https://doi.org/10.20964/2020.02.24.
Gao, X. *et al.* (2025) "Simulation and understanding of degraded lithium-ion battery self-heating ignition," *Applied Energy*, 384, p. 125435. Available at: https://doi.org/https://doi.org/10.1016/j.apenergy.2025.125435.
Gnielinski, V. (1976) "New Equations for Heat and Mass Transfer in Turbulent Pipe and Channel Flow," *International Chemical Engineering*, 16(2), pp. 359–368.
Gómez Díaz, K.Y. *et al.* (2025) "Thermal Management Systems for Lithium-Ion Batteries for Electric Vehicles: A Review," *World Electric Vehicle Journal*. Multidisciplinary Digital Publishing Institute (MDPI). Available at: https://doi.org/10.3390/wevj16070346.
Guo, C.Y. *et al.* (2025) "A Critical Review of Advancements and Challenges in Thermal Management Systems for Lithium-Ion Batteries," *Journal of Advanced Research in Numerical Heat Transfer*, 35(1), pp. 117–161. Available at: https://doi.org/10.37934/arnht.35.1.117161.
Guo, J. *et al.* (2023) "The Polarization and Heat Generation Characteristics of Lithium-Ion Battery with Electric–Thermal Coupled Modeling," *Batteries*, 9(11). Available at: https://doi.org/10.3390/batteries9110529.
Guo, J. and Jiang, F. (2021a) "A novel electric vehicle thermal management system based on cooling and heating of batteries by refrigerant," *Energy Conversion and Management*, 237, p. 114145. Available at: https://doi.org/https://doi.org/10.1016/j.enconman.2021.114145.
Guo, J. and Jiang, F. (2021b) "A novel electric vehicle thermal management system based on cooling and heating of batteries by refrigerant," *Energy Conversion and Management*, 237. Available at: https://doi.org/10.1016/j.enconman.2021.114145.

Guo, R. *et al.* (2023) "An integrated thermal management strategy for cabin and battery heating in range-extended electric vehicles under low-temperature conditions," *Applied Thermal Engineering*, 228. Available at: https://doi.org/10.1016/j.applthermaleng.2023.120502.

Hamed, M.M. *et al.* (2022) "A review on recent key technologies of lithium-ion battery thermal management: External cooling systems," *Results in Engineering*. Elsevier B.V. Available at: https://doi.org/10.1016/j.rineng.2022.100703.

Han, J. *et al.* (2025) "Fast and Energy-Efficient Compound Self-Heating of Automotive Batteries Based on Electrochemical-Thermal-Stress Aging Model," *IEEE Transactions on Transportation Electrification*, 11(1), pp. 476–485. Available at: https://doi.org/10.1109/TTE.2024.3392371.

Han, J.W. *et al.* (2022) "Experimental Study on Dielectric Fluid Immersion Cooling for Thermal Management of Lithium-Ion Battery," *Symmetry*, 14(10). Available at: https://doi.org/10.3390/sym14102126.

Han, M. *et al.* (2024) "Safe bidirectional pulse heating method for the lithium-ion battery pack on a high-power electric motorcycle," *Journal of Energy Storage*, 92. Available at: https://doi.org/10.1016/j.est.2024.111866.

Han, S. *et al.* (2025) "An Improved PSO-Based DC Discharge Heating Strategy for Lithium-Ion Batteries at Low Temperatures," *Energies*, 18(9). Available at: https://doi.org/10.3390/en18092261.

Hawkins, T.R. *et al.* (2013) "Comparative Environmental Life Cycle Assessment of Conventional and Electric Vehicles," *Journal of Industrial Ecology*, 17(1), pp. 53–64. Available at: https://doi.org/10.1111/j.1530-9290.2012.00532.x.

He, C.X. *et al.* (2021) "A 3D electrochemical-thermal coupled model for electrochemical and thermal analysis of pouch-type lithium-ion batteries," *International Journal of Heat and Mass Transfer*, 181. Available at: https://doi.org/10.1016/j.ijheatmasstransfer.2021.121855.

He, L. *et al.* (2023) "Review of thermal management system for battery electric vehicle," *Journal of Energy Storage*. Elsevier Ltd. Available at: https://doi.org/10.1016/j.est.2022.106443.

He, L. *et al.* (2024) "Performance investigation of integrated thermal management system for electric vehicle with waste heat recovery of electric drive system," *Journal of Energy Storage*, 102. Available at: https://doi.org/10.1016/j.est.2024.114075.

He, P. *et al.* (2023) "Numerical investigation on a lithium-ion battery thermal management system utilizing a double-layered I-shaped channel liquid cooling plate exchanger," *International Journal of Thermal Sciences*, 187. Available at: https://doi.org/10.1016/j.ijthermalsci.2023.108200.

He, X. *et al.* (2020) "Experimental Study of Self-heating Ignition of Lithium-Ion Batteries During Storage: Effect of the Number of Cells," *Fire Technology*, 56(6), pp. 2649–2669. Available at: https://doi.org/10.1007/s10694-020-01011-y.

Helmers, E., Dietz, J. and Weiss, M. (2020) "Sensitivity analysis in the life-cycle assessment of electric vs. combustion engine cars under approximate real-world conditions," *Sustainability (Switzerland)*, 12(3). Available at: https://doi.org/10.3390/su12031241.

Heubner, C., Schneider, M. and Michaelis, A. (2016) "Detailed study of heat generation in porous LiCoO2 electrodes," *Journal of Power Sources*, 307, pp. 199–207. Available at: https://doi.org/10.1016/j.jpowsour.2015.12.096.

Hong, S.H. *et al.* (2020) "Thermal performance of direct two-phase refrigerant cooling for lithium-ion batteries in electric vehicles," *Applied Thermal Engineering*, 173, p. 115213. Available at: https://doi.org/https://doi.org/10.1016/j.applthermaleng.2020.115213.

Hu, D. *et al.* (2024) "A review on thermal runaway warning technology for lithium-ion batteries," *Renewable and Sustainable Energy Reviews*. Elsevier Ltd. Available at: https://doi.org/10.1016/j.rser.2024.114882.

Hu, X. *et al.* (2020a) "Battery warm-up methodologies at subzero temperatures for automotive applications: Recent advances and perspectives," *Progress in Energy and Combustion Science*. Elsevier Ltd. Available at: https://doi.org/10.1016/j.pecs.2019.100806.

Hu, X. *et al.* (2020b) "Battery warm-up methodologies at subzero temperatures for automotive applications: Recent advances and perspectives," *Progress in Energy and Combustion Science*. Elsevier Ltd. Available at: https://doi.org/10.1016/j.pecs.2019.100806.

Hu, Z. *et al.* (2022) "Thermal Characteristics Investigation of Lithium-Ion Battery Under High-Frequency AC Excitation in Lowerature Environment," *IEEE Transactions on Transportation Electrification*, 8(1), pp. 407–419. Available at: https://doi.org/10.1109/TTE.2021.3113945.

Huang, D., Chen, Z. and Zhou, S. (2022) "Self-powered heating strategy for lithium-ion battery pack applied in extremely cold climates," *Energy*, 239. Available at: https://doi.org/10.1016/j.energy.2021.122095.

Huang, Q. *et al.* (2021) "Thermal management of Lithium-ion battery pack through the application of flexible form-stable composite phase change materials," *Applied Thermal Engineering*, 183. Available at: https://doi.org/10.1016/j.applthermaleng.2020.116151.

Huang, R. *et al.* (2023) "Investigating the Effect of Different Bidirectional Pulsed Current Parameters on the Heat Generation of Lithium-Ion Battery at Low Temperatures," *Batteries*, 9(9). Available at: https://doi.org/10.3390/batteries9090457.

Huang, R. *et al.* (2024) "Targeting the low-temperature performance degradation of lithium-ion batteries: A non-destructive bidirectional pulse current heating framework," *Energy Storage Materials*, 65, p. 103173. Available at: https://doi.org/https://doi.org/10.1016/j.ensm.2024.103173.

Huang, X. *et al.* (2024) "Alternating current heating techniques for lithium-ion batteries in electric vehicles: Recent advances and perspectives," *Journal*

of Energy Chemistry, 96, pp. 679–697. Available at: https://doi.org/https://doi.org/10.1016/j.jechem.2024.05.027.
Huang, Y. *et al.* (2021) “Challenges and recent progress in thermal management with heat pipes for lithium-ion power batteries in electric vehicles,” *Science China Technological Sciences*, 64(5), pp. 919–956. Available at: https://doi.org/10.1007/s11431-020-1714-1.
Huang, Z. *et al.* (2020) “A Fast Energy-efficient Pulse Preheating Strategy For Li-ion Battery At Subzero Temperatures,” *2020 IEEE Energy Conversion Congress and Exposition (ECCE)*, pp. 4446–4451. Available at: https://doi.org/10.1109/ECCE44975.2020.9236077.
Huo, Z. *et al.* (2023) “Numerical study of paraffin and glass fiber composites for thermal management of lithium-ion battery packs.”
Hussain, M., Khan, M.K. and Pathak, M. (2024) “Thermal management of high-energy lithium titanate oxide batteries using an effective channeled dielectric fluid immersion cooling system,” *Energy Conversion and Management*, 313. Available at: https://doi.org/10.1016/j.enconman.2024.118644.
Hwang, F.S. *et al.* (2024) “Review of battery thermal management systems in electric vehicles,” *Renewable and Sustainable Energy Reviews*. Elsevier Ltd. Available at: https://doi.org/10.1016/j.rser.2023.114171.
Hyun, S.W., Kim, J.H. and Shin, D.H. (2025) “Hybrid PCM–Liquid Cooling System with Optimized Channel Design for Enhanced Thermal Management of Lithium–Ion Batteries,” *Energies*, 18(18). Available at: https://doi.org/10.3390/en18184996.
Jaguemont, J. and Van Mierlo, J. (2020) “A comprehensive review of future thermal management systems for battery-electrified vehicles,” *Journal of Energy Storage*. Elsevier Ltd. Available at: https://doi.org/10.1016/j.est.2020.101551.
Jahl, L.G. *et al.* (2025) “High Potential Harm, Questionable Fire-Safety Benefit: Why Are Flame Retardants in Lithium-Ion Battery Enclosures?,” *Environmental Science and Technology* [Preprint]. American Chemical Society. Available at: https://doi.org/10.1021/acs.est.4c10630.
Jamsawang, S. *et al.* (2024) “Investigation of the Performance of Battery Thermal Management Based on Direct Refrigerant Cooling: Simulation, Validation of Results, and Parametric Studies,” *Energies*, 17(2). Available at: https://doi.org/10.3390/en17020543.
Ji, Y. and Wang, C.Y. (2013) “Heating strategies for Li-ion batteries operated from subzero temperatures,” *Electrochimica Acta*, 107, pp. 664–674. Available at: https://doi.org/10.1016/j.electacta.2013.03.147.
Ji, Y., Zhang, Y. and Wang, C.-Y. (2013) “Li-Ion Cell Operation at Low Temperatures,” *Journal of The Electrochemical Society*, 160(4), pp. A636–A649. Available at: https://doi.org/10.1149/2.047304jes.
Jiang, J. *et al.* (2018) “A low-temperature internal heating strategy without lifetime reduction for large-size automotive lithium-ion battery pack,”

Applied Energy, 230, pp. 257–266. Available at: https://doi.org/https://doi.org/10.1016/j.apenergy.2018.08.070.
Jiang, K. *et al.* (2020) "Thermal management technology of power lithium-ion batteries based on the phase transition of materials: A review," *Journal of Energy Storage*. Elsevier Ltd. Available at: https://doi.org/10.1016/j.est.2020.101816.
Jithin, K. V. and Rajesh, P.K. (2022) "Numerical analysis of single-phase liquid immersion cooling for lithium-ion battery thermal management using different dielectric fluids," *International Journal of Heat and Mass Transfer*, 188. Available at: https://doi.org/10.1016/j.ijheatmasstransfer.2022.122608.
Jobby, A., Khatamifar, M. and Lin, W. (2025) "A Comprehensive Review on the Natural Convection Heat Transfer in Horizontal and Inclined Closed Rectangular Enclosures with Internal Objects at Various Heating Conditions," *Energies*. Multidisciplinary Digital Publishing Institute (MDPI). Available at: https://doi.org/10.3390/en18040950.
Jouhara, H. *et al.* (2021) "Heat pipe based battery thermal management: Evaluating the potential of two novel battery pack integrations," *International Journal of Thermofluids*, 12. Available at: https://doi.org/10.1016/j.ijft.2021.100115.
Kandlikar, S.G. and King, M.R. (2014) "Chapter 1 - Introduction," in S.G. Kandlikar et al. (eds.) *Heat Transfer and Fluid Flow in Minichannels and Microchannels (Second Edition)*. Second Edition. Oxford: Butterworth-Heinemann, pp. 1–9. Available at: https://doi.org/https://doi.org/10.1016/B978-0-08-098346-2.00001-6.
Kang, Y. *et al.* (2024) "Application of Refrigerant Cooling in a Battery Thermal Management System under High Temperature Conditions: A Review," *ACS Omega*. American Chemical Society, pp. 25591–25609. Available at: https://doi.org/10.1021/acsomega.4c02902.
Kaya, Y.Ç. and Kaya, H. (2025) "Global Energy Policy: A Legal Perspective on Renewable Energy Initiatives," *Sustainability (Switzerland)*, 17(9). Available at: https://doi.org/10.3390/su17093991.
Kim, H.-K., Choi, J.H. and Lee, K.-J. (2019) "A Numerical Study of the Effects of Cell Formats on the Cycle Life of Lithium Ion Batteries," *Journal of The Electrochemical Society*, 166(10), pp. A1769–A1778. Available at: https://doi.org/10.1149/2.0261910jes.
Kim, J., Oh, J. and Lee, H. (2019) "Review on battery thermal management system for electric vehicles," *Applied Thermal Engineering*. Elsevier Ltd, pp. 192–212. Available at: https://doi.org/10.1016/j.applthermaleng.2018.12.020.
Kocsis, D., T. Kiss, J. and Arpad, I.W. (2024) "Evaluating battery electric vehicle usage in the EU: A comparative study based on member state energy mixes," *Heliyon*, 10(9). Available at: https://doi.org/10.1016/j.heliyon.2024.e30655.

Kuehn, T.H. and Goldstein, R. 1 (1976) *Correlating equations for natural convection heat transfer between horizontal circular cylinders*. Pergamon Press.
Lai, Y. *et al.* (2019) "A compact and lightweight liquid-cooled thermal management solution for cylindrical lithium-ion power battery pack," *International Journal of Heat and Mass Transfer*, 144. Available at: https://doi.org/10.1016/j.ijheatmasstransfer.2019.118581.
Larrañaga-Ezeiza, M. *et al.* (2022) "A novel direct liquid cooling strategy for electric vehicles focused on pouch type battery cells," *Applied Thermal Engineering*, 216. Available at: https://doi.org/10.1016/j.applthermaleng.2022.118869.
Lee, M. *et al.* (2020) "Improvement of Grid Independence Test for Computational Fluid Dynamics Model of Building Based on Grid Resolution," *Advances in Civil Engineering*, 2020. Available at: https://doi.org/10.1155/2020/8827936.
Lee, S. *et al.* (2023) "Battery thermal management strategy utilizing a secondary heat pump in electric vehicle under cold-start conditions," *Energy*, 269. Available at: https://doi.org/10.1016/j.energy.2023.126827.
Li, D. *et al.* (2023) "Effects of pulsating flow on the performance of multi-channel cold plate for thermal management of lithium-ion battery pack," *Energy*, 273. Available at: https://doi.org/10.1016/j.energy.2023.127250.
Li, J. *et al.* (2019) "Sinusoidal alternating current heating strategy and optimization of lithium-ion batteries with a thermo-electric coupled model," *Energy*, 186, p. 115798. Available at: https://doi.org/https://doi.org/10.1016/j.energy.2019.07.128.
Li, J. and Yang, L. (2022) "Back side of the coin: How does non-fossil energy diffusion result in less efficient fossil-based technologies," *Environmental Impact Assessment Review*, 96, p. 106848. Available at: https://doi.org/https://doi.org/10.1016/j.eiar.2022.106848.
Li, K. *et al.* (2024) "A Study of the Thermal Management and Discharge Strategies of Lithium-Ion Batteries in a Wide Temperature Range," *Energies* , 17(10). Available at: https://doi.org/10.3390/en17102319.
Li, W. *et al.* (2023) "An Internal Heating Strategy for Lithium-Ion Batteries Without Lithium Plating Based on Self-Adaptive Alternating Current Pulse," *IEEE Transactions on Vehicular Technology*, 72(5), pp. 5809–5823. Available at: https://doi.org/10.1109/TVT.2022.3229187.
Li, W. *et al.* (2025) "Insights into lithium plating characteristics enable plating-free heating strategy for bidirectional pulse utilizing a refined physics-based model," *International Journal of Heat and Mass Transfer*, 238. Available at: https://doi.org/10.1016/j.ijheatmasstransfer.2024.126440.
Li, X. *et al.* (2019) "Experimental investigation of the thermal performance of silicon cold plate for battery thermal management system," *Applied Thermal Engineering*, 155, pp. 331–340. Available at: https://doi.org/10.1016/j.applthermaleng.2019.04.007.

Li, X. *et al.* (2024) “Investigation on the heat generation and heat sources of cylindrical NCM811 lithium-ion batteries,” *Applied Thermal Engineering*, 241. Available at: https://doi.org/10.1016/j.applthermaleng.2024.122403.
Li, Y., Zhou, Z. and Wu, W.T. (2019) “Three-dimensional thermal modeling of Li-ion battery cell and 50 V Li-ion battery pack cooled by mini-channel cold plate,” *Applied Thermal Engineering*, 147, pp. 829–840. Available at: https://doi.org/10.1016/j.applthermaleng.2018.11.009.
Lian, Y. *et al.* (2023) “Experimental investigation on a heating-and-cooling difunctional battery thermal management system based on refrigerant,” *Applied Thermal Engineering*, 225, p. 120138. Available at: https://doi.org/https://doi.org/10.1016/j.applthermaleng.2023.120138.
Lin, B., Cen, J. and Jiang, F. (2021) “Thermal performance of a cylindrical lithium-ion battery module cooled by two-phase refrigerant circulation,” *Energies*, 14(23). Available at: https://doi.org/10.3390/en14238094.
Lin, J. *et al.* (2021a) “A review on recent progress, challenges and perspective of battery thermal management system,” *International Journal of Heat and Mass Transfer*. Elsevier Ltd. Available at: https://doi.org/10.1016/j.ijheatmasstransfer.2020.120834.
Lin, J. *et al.* (2021b) “A review on recent progress, challenges and perspective of battery thermal management system,” *International Journal of Heat and Mass Transfer*, 167, p. 120834. Available at: https://doi.org/https://doi.org/10.1016/j.ijheatmasstransfer.2020.120834.
Lin, X. *et al.* (2021) “Lithium Plating Mechanism, Detection, and Mitigation in Lithium-Ion Batteries,” *Progress in Energy and Combustion Science*. Elsevier Ltd. Available at: https://doi.org/10.1016/j.pecs.2021.100953.
Lin, X.-W. *et al.* (2024) “Advances on two-phase heat transfer for lithium-ion battery thermal management,” *Renewable and Sustainable Energy Reviews*, 189, p. 114052. Available at: https://doi.org/https://doi.org/10.1016/j.rser.2023.114052.
Linden, David. and Reddy, T.B. (2002) *Handbook of batteries*. McGraw-Hill.
Ling, Z. *et al.* (2018) “Thermal management performance of phase change materials with different thermal conductivities for Li-ion battery packs operated at low temperatures,” *Energy*, 144, pp. 977–983. Available at: https://doi.org/10.1016/j.energy.2017.12.098.
Liu, C. *et al.* (2020a) “Phase change materials application in battery thermal management system: A review,” *Materials*. MDPI AG, pp. 1–37. Available at: https://doi.org/10.3390/ma13204622.
Liu, C. *et al.* (2020b) “Phase change materials application in battery thermal management system: A review,” *Materials*. MDPI AG, pp. 1–37. Available at: https://doi.org/10.3390/ma13204622.
Liu, J. *et al.* (2023) “Recent Progress and Prospects in Liquid Cooling Thermal Management System for Lithium-Ion Batteries,” *Batteries*.

Multidisciplinary Digital Publishing Institute (MDPI). Available at: https://doi.org/10.3390/batteries9080400.

Liu, Jie *et al.* (2024) “Review of thermal coupled battery models and parameter identification for lithium-ion battery heat generation in EV battery thermal management system,” *International Journal of Heat and Mass Transfer*. Elsevier Ltd. Available at: https://doi.org/10.1016/j.ijheatmasstransfer.2023.124748.

Liu, Jin *et al.* (2024) “Size effect on the thermal and mechanical performance of cylindrical lithium-ion batteries,” *Applied Energy*, 375. Available at: https://doi.org/10.1016/j.apenergy.2024.124056.

Liu, M.S. *et al.* (2006) “Enhancement of thermal conductivity with Cu for nanofluids using chemical reduction method,” *International Journal of Heat and Mass Transfer*, 49(17–18), pp. 3028–3033. Available at: https://doi.org/10.1016/j.ijheatmasstransfer.2006.02.012.

Liu, Shan, Yan, J., *et al.* (2024) “Joint operation of mobile battery, power system, and transportation system for improving the renewable energy penetration rate,” *Applied Energy*, 357, p. 122455. Available at: https://doi.org/https://doi.org/10.1016/j.apenergy.2023.122455.

Liu, Xiao Ang, Zhang, F., *et al.* (2024) “A three-heat source segmented heating control strategy based on waste heat recovery technology for electric vehicles,” *Energy Conversion and Management*, 300. Available at: https://doi.org/10.1016/j.enconman.2023.117932.

Liu, Yizhe, Li, X., *et al.* (2024) “Carbon-Enhanced Hydrated Salt Phase Change Materials for Thermal Management Applications,” *Nanomaterials*. Multidisciplinary Digital Publishing Institute (MDPI). Available at: https://doi.org/10.3390/nano14131077.

Liu, Z. *et al.* (2023) “Thermal management of lithium-ion battery pack under demanding conditions and long operating cycles using fin-enhanced PCMs/water hybrid cooling system,” *Applied Thermal Engineering*, 233, p. 121214. Available at: https://doi.org/https://doi.org/10.1016/j.applthermaleng.2023.121214.

Luo, J. *et al.* (2022) “Battery thermal management systems (BTMs) based on phase change material (PCM): A comprehensive review,” *Chemical Engineering Journal*, 430, p. 132741. Available at: https://doi.org/https://doi.org/10.1016/j.cej.2021.132741.

Luo, M. *et al.* (2023) “Fast self-preheating system and energy conversion model for lithium-ion batteries under low-temperature conditions,” *Journal of Power Sources*, 565. Available at: https://doi.org/10.1016/j.jpowsour.2023.232897.

Luo, P. *et al.* (2022) “Coupled Electrochemical-Thermal-Mechanical Modeling and Simulation of Lithium-Ion Batteries,” *Journal of The Electrochemical Society*, 169(10), p. 100535. Available at: https://doi.org/10.1149/1945-7111/ac9a04.

Lv, Ran *et al.* (2022) "Heating performance of heat pump air conditioning system for battery electric vehicle with different refrigerants," *Proceedings of the Institution of Mechanical Engineers, Part D: Journal of Automobile Engineering*, 238(4), pp. 702–718. Available at: https://doi.org/10.1177/09544070221135445.
Macgregor, R.K. and Emery, A.F. (1969) "Free Convection Through Vertical Plane Layers—Moderate and High Prandtl Number Fluids," *Journal of Heat Transfer-transactions of The Asme*, 91, pp. 391–401. Available at: https://api.semanticscholar.org/CorpusID:119434404.
Machedon-Pisu, M. and Borza, P.N. (2023) "Is the Transition to Electric Passenger Cars Sustainable? A Life Cycle Perspective," *Sustainability (Switzerland)*, 15(3). Available at: https://doi.org/10.3390/su15032614.
Madani, S.S., Ziebert, C. and Marzband, M. (2023) "Thermal Behavior Modeling of Lithium-Ion Batteries: A Comprehensive Review," *Symmetry*. Multidisciplinary Digital Publishing Institute (MDPI). Available at: https://doi.org/10.3390/sym15081597.
Mahian, O. *et al.* (2016) "Natural convection of silica nanofluids in square and triangular enclosures: Theoretical and experimental study," *International Journal of Heat and Mass Transfer*, 99, pp. 792–804. Available at: https://doi.org/10.1016/j.ijheatmasstransfer.2016.03.045.
Maiorino, A. *et al.* (2024) "A review on thermal management of battery packs for electric vehicles," *Applied Thermal Engineering*, 238, p. 122035. Available at: https://doi.org/10.1016/j.applthermaleng.2023.122035.
Mancini, N. *et al.* (2019) "OPTIMAL SOURCE ELECTRIC VEHICLE HEAT PUMP WITH EXTREME TEMPERATURE HEATING CAPABILITY AND EFFICIENT THERMAL PRECONDITIONING ." United States.
Mao, B. *et al.* (2020) "Self-heating reaction and thermal runaway criticality of the lithium ion battery," *International Journal of Heat and Mass Transfer*, 149, p. 119178. Available at: https://doi.org/https://doi.org/10.1016/j.ijheatmasstransfer.2019.119178.
Martins, F. *et al.* (2019) "Analysis of fossil fuel energy consumption and environmental impacts in european countries," *Energies*, 12(6). Available at: https://doi.org/10.3390/en12060964.
Martins, F., Felgueiras, C. and Smitková, M. (2018) "Fossil fuel energy consumption in European countries," *Energy Procedia*, 153, pp. 107–111. Available at: https://doi.org/https://doi.org/10.1016/j.egypro.2018.10.050.
Mehrabi-Kermani, M., Houshfar, E. and Ashjaee, M. (2019) "A novel hybrid thermal management for Li-ion batteries using phase change materials embedded in copper foams combined with forced-air convection," *International Journal of Thermal Sciences*, 141, pp. 47–61. Available at: https://doi.org/https://doi.org/10.1016/j.ijthermalsci.2019.03.026.
Mohamed, M.S., Bal, D.K. and Sahoo, B.B. (2025) "A technical review on controlling the Li-ion battery temperature through composite phase change

materials and hybrid cooling techniques," *Journal of Energy Storage*. Elsevier Ltd. Available at: https://doi.org/10.1016/j.est.2025.115584.
Morgan, V.T. (1975) "The Overall Convective Heat Transfer from Smooth Circular Cylinders," *Advances in Heat Transfer* [Preprint]. Available at: https://doi.org/10.1016/S0065-2717(08)70075-3.
Möring-Martínez, G., Senzeybek, M. and Jochem, P. (2024) "Clustering the European Union electric vehicle markets: A scenario analysis until 2035," *Transportation Research Part D: Transport and Environment*, 135, p. 104372. Available at: https://doi.org/https://doi.org/10.1016/j.trd.2024.104372.
Murugan, M. *et al.* (2022) "Thermal management system of lithium-ion battery packs for electric vehicles: An insight based on bibliometric study," *Journal of Energy Storage*, 52. Available at: https://doi.org/10.1016/j.est.2022.104723.
Mwambeleko, J.J. and Kulworawanichpong, T. (2017) "Battery electric multiple units to replace diesel commuter trains serving short and idle routes," *Journal of Energy Storage*, 11, pp. 7–15. Available at: https://doi.org/https://doi.org/10.1016/j.est.2017.01.004.
Nájera, J. *et al.* (2023) "Semi-empirical ageing model for LFP and NMC Li-ion battery chemistries," *Journal of Energy Storage*, 72, p. 108016. Available at: https://doi.org/https://doi.org/10.1016/j.est.2023.108016.
Naseem, H. and Seok, J.K. (2025) "Recent Advances in Bidirectional Converters and Regenerative Braking Systems in Electric Vehicles," *Actuators*. Multidisciplinary Digital Publishing Institute (MDPI). Available at: https://doi.org/10.3390/act14070347.
Nasiri, M. and Hadim, H. (2025) "Thermal management of Li-ion batteries using phase change materials: Recent advances and future challenges," *Journal of Energy Storage*. Elsevier Ltd. Available at: https://doi.org/10.1016/j.est.2025.115440.
Nazari, A. and Farhad, S. (2017) "Heat generation in lithium-ion batteries with different nominal capacities and chemistries," *Applied Thermal Engineering*, 125, pp. 1501–1517. Available at: https://doi.org/10.1016/j.applthermaleng.2017.07.126.
Nikolian, A. *et al.* (2016) "Lithium ion batteries-development of advanced electrical equivalent circuit models for nickel manganese cobalt lithium-ion," *Energies*, 9(5), p. 360. Available at: https://doi.org/10.3390/en9050360.
Ogura, K. and Kolhe, M.L. (2017) "Battery technologies for electric vehicles," *Electric Vehicles: Prospects and Challenges*. Elsevier Inc., pp. 139–167. Available at: https://doi.org/10.1016/B978-0-12-803021-9.00004-5.
Orangi, S. *et al.* (2024) "Historical and prospective lithium-ion battery cost trajectories from a bottom-up production modeling perspective," *Journal of*

Energy Storage, 76, p. 109800. Available at: https://doi.org/https://doi.org/10.1016/j.est.2023.109800.

Outlook, G.E. (2025) *Global EV Outlook 2025 Expanding sales in diverse markets*. Available at: www.iea.org.

Ouyang, D. *et al.* (2022) "Sensitivities of lithium-ion batteries with different capacities to overcharge/over-discharge," *Journal of Energy Storage*, 52, p. 104997. Available at: https://doi.org/https://doi.org/10.1016/j.est.2022.104997.

Ozguc, S. *et al.* (2025) "Experimental investigation of an additively manufactured cold plate for multi-chip module cooling generated using the homogenization approach to topology optimization," *Applied Thermal Engineering*, 258. Available at: https://doi.org/10.1016/j.applthermaleng.2024.124741.

Parlak, M. (2024) "Thermal management with double layered heat sink produced by direct metal laser sintering," *International Journal of Energy Studies*, 9(1), pp. 155–173. Available at: https://doi.org/10.58559/ijes.1439889.

Parveen (2025) *A Comprehensive Study of Battery Thermal Management Strategies for Lithium-Ion Batteries*, *International Journal of Enhanced Research in Science*.

Patel, Jay R. and Rathod, M.K. (2020) "Recent developments in the passive and hybrid thermal management techniques of lithium-ion batteries," *Journal of Power Sources*. Elsevier B.V. Available at: https://doi.org/10.1016/j.jpowsour.2020.228820.

Patel, Jay R and Rathod, M.K. (2020) "Recent developments in the passive and hybrid thermal management techniques of lithium-ion batteries," *Journal of Power Sources*, 480, p. 228820. Available at: https://doi.org/https://doi.org/10.1016/j.jpowsour.2020.228820.

Pei, G. *et al.* (2025) "Assessing the climate and health impacts of energy consumption in European Union countries," *Environmental Research Letters* , 20(6). Available at: https://doi.org/10.1088/1748-9326/add752.

Di Persio, F.. and Ruiz, V.. (2018) *Standards for the performance and durability assessment of electric vehicle batteries : possible performance criteria for an Ecodesign Regulation*. Publications Office of the European Union.

Pesaran, A., Santhanagopalan, S. and Kim, G.-H. (2013) *Addressing the Impact of Temperature Extremes on Large Format Li-Ion Batteries for Vehicle Applications (Presentation), NREL (National Renewable Energy Laboratory)*. Available at: https://www.nrel.gov/docs/fy13osti/58145.pdf (Accessed: October 13, 2023).

Pilali, E. *et al.* (2025) "Passive thermal management systems with phase change material-based methods for lithium-ion batteries: A state-of-the-art review," *Journal of Power Sources*. Elsevier B.V. Available at: https://doi.org/10.1016/j.jpowsour.2025.236345.

Popovich, N.D. *et al.* (2021) “Economic, environmental and grid-resilience benefits of converting diesel trains to battery-electric,” *Nature Energy*, 6(11), pp. 1017–1025. Available at: https://doi.org/10.1038/s41560-021-00915-5.

Pugi, Luca and di Carlo, Luca (2024) “Multi-modal battery-operated trains on partially electrified lines: A case study on some regional lines in Italy,” *Proceedings of the Institution of Mechanical Engineers, Part F: Journal of Rail and Rapid Transit*, 238(7), pp. 873–885. Available at: https://doi.org/10.1177/09544097241234959.

Putra, M.R.A. *et al.* (2025) “Enhancing Hybrid Train Battery Performance using Liquid-Based Battery Thermal Management with Mini Channels Cooling System,” *CFD Letters*, 17(12), pp. 234–246. Available at: https://doi.org/10.37934/cfdl.17.12.234246.

Qin, Y. *et al.* (2020) “A rapid lithium-ion battery heating method based on bidirectional pulsed current: Heating effect and impact on battery life,” *Applied Energy*, 280. Available at: https://doi.org/10.1016/j.apenergy.2020.115957.

Rastan, H. *et al.* (2020) “Heat transfer study of enhanced additively manufactured minichannel heat exchangers,” *International Journal of Heat and Mass Transfer*, 161. Available at: https://doi.org/10.1016/j.ijheatmasstransfer.2020.120271.

Regione Emilia-Romagna (2023) *Veicoli elettrici e ibridi: quarantena precauzionale di 15 giorni*. Available at: https://www.regione.emilia-romagna.it/alluvione/aggiornamenti/2023/maggio/veicoli-elettrici-e-ibridi-quarantena-precauzionale-di-15-giorni (Accessed: July 7, 2023).

Reynier, Y. *et al.* (2004a) “Entropy of Li intercalation in LixCoO2,” *Physical Review B - Condensed Matter and Materials Physics*, 70(17), pp. 1–7. Available at: https://doi.org/10.1103/PhysRevB.70.174304.

Reynier, Y. *et al.* (2004b) “Entropy of Li intercalation in LixCoO2,” *Physical Review B - Condensed Matter and Materials Physics*, 70(17), pp. 1–7. Available at: https://doi.org/10.1103/PhysRevB.70.174304.

Ria, A. and Dini, P. (2024) “A Compact Overview on Li-Ion Batteries Characteristics and Battery Management Systems Integration for Automotive Applications,” *Energies*. Multidisciplinary Digital Publishing Institute (MDPI). Available at: https://doi.org/10.3390/en17235992.

Rodriguez, S. (2019) *Applied Computational Fluid Dynamics and Turbulence Modeling*. Springer Cham. Available at: https://doi.org/https://doi.org/10.1007/978-3-030-28691-0.

Roe, C. *et al.* (2022a) “Immersion cooling for lithium-ion batteries – A review,” *Journal of Power Sources*. Elsevier B.V. Available at: https://doi.org/10.1016/j.jpowsour.2022.231094.

Roe, C. *et al.* (2022b) “Immersion cooling for lithium-ion batteries – A review,” *Journal of Power Sources*. Elsevier B.V. Available at: https://doi.org/10.1016/j.jpowsour.2022.231094.

Rohsenow, W.M.., Hartnett, J.P.. and Cho, Y.I.. (1998) *Handbook of Heat Transfer*. McGraw-Hill.
Ruan, H. *et al.* (2019) “An optimal internal-heating strategy for lithium-ion batteries at low temperature considering both heating time and lifetime reduction,” *Applied Energy*, 256, p. 113797. Available at: https://doi.org/https://doi.org/10.1016/j.apenergy.2019.113797.
Ruan, H. *et al.* (2021) “Compound self-heating strategies and multi-objective optimization for lithium-ion batteries at low temperature,” *Applied Thermal Engineering*, 186, p. 116158. Available at: https://doi.org/https://doi.org/10.1016/j.applthermaleng.2020.116158.
Ruan, H. *et al.* (2022) “Optimal external heating resistance enabling rapid compound self-heating for lithium-ion batteries at low temperatures,” *Applied Thermal Engineering*, 200, p. 117536. Available at: https://doi.org/https://doi.org/10.1016/j.applthermaleng.2021.117536.
Ruan, H. *et al.* (2023) “The heating triangle: A quantitative review of self-heating methods for lithium-ion batteries at low temperatures,” *Journal of Power Sources*, 581, p. 233484. Available at: https://doi.org/https://doi.org/10.1016/j.jpowsour.2023.233484.
Sahin, R.C., Gocmen, S. and Cetkin, E. (2022) “Thermal management system for air-cooled battery packs with flow-disturbing structures,” *Journal of Power Sources*, 551. Available at: https://doi.org/10.1016/j.jpowsour.2022.232214.
Salhein, K., Kobus, C.J. and Zohdy, M. (2022) “Control of Heat Transfer in a Vertical Ground Heat Exchanger for a Geothermal Heat Pump System,” *Energies*, 15(14). Available at: https://doi.org/10.3390/en15145300.
Selvnes, H. *et al.* (2021) “Review on cold thermal energy storage applied to refrigeration systems using phase change materials,” *Thermal Science and Engineering Progress*. Elsevier Ltd. Available at: https://doi.org/10.1016/j.tsep.2020.100807.
Sezai, I. and Mohamad, A.A. (no date) *Natural convection from a discrete heat source on the bottom of a horizontal enclosure*. Available at: www.elsevier.com/locate/ijhmt.
Shahid, S. and Agelin-Chaab, M. (2022) “A review of thermal runaway prevention and mitigation strategies for lithium-ion batteries,” *Energy Conversion and Management: X*. Elsevier Ltd. Available at: https://doi.org/10.1016/j.ecmx.2022.100310.
Shahjalal, M., Shams, T., Islam, M.E., *et al.* (2021) “A review of thermal management for Li-ion batteries: Prospects, challenges, and issues,” *Journal of Energy Storage*. Elsevier Ltd. Available at: https://doi.org/10.1016/j.est.2021.102518.
Shahjalal, M., Shams, T., Islam, Md.E., *et al.* (2021) “A review of thermal management for Li-ion batteries: Prospects, challenges, and issues,” *Journal of Energy Storage*, 39, p. 102518. Available at: https://doi.org/https://doi.org/10.1016/j.est.2021.102518.

Shakir, H.M.F. *et al.* (2022) “Fabrication of low emissivity paint for thermal/NIR radiation insulation for domestic applications,” *Energy Reports*, 8, pp. 7814–7824. Available at: https://doi.org/10.1016/j.egyr.2022.05.287.

Shang, Y. *et al.* (2020) “A Compact Resonant Switched-Capacitor Heater for Lithium-Ion Battery Self-Heating at Low Temperatures,” *IEEE Transactions on Power Electronics*, 35(7), pp. 7134–7144. Available at: https://doi.org/10.1109/TPEL.2019.2954703.

Shao, W. *et al.* (2023) “Study on the Reversible and Irreversible Heat Generation of the Lithium-Ion Battery with LiFePO4 Cathode,” *Fire Technology*, 59(2), pp. 289–303. Available at: https://doi.org/10.1007/s10694-022-01325-z.

Sharma, D. (1983) “Calculation of fully developed turbulent flows in ducts of arbitrary cross-section,” *Journal of Fluid Mechanics*, 128(HY3), pp. 199–217. Available at: https://doi.org/10.1017/S0022112083000440.

Shcherbakov, G.A. (2022) “The global shortage of semiconductor components as a source of the current crisis in the global automotive industry,” *MIR (Modernization. Innovation. Research)*, 13(2), pp. 270–287. Available at: https://doi.org/10.18184/2079-4665.2022.13.2.270-287.

Shen, H.X. *et al.* (2021) “Estimation of state of charge of lithium battery based on parameter identification of fractional order model,” *Journal of Physics: Conference Series*. IOP Publishing Ltd. Available at: https://doi.org/10.1088/1742-6596/1774/1/012049.

Shen, X. *et al.* (2023) “Thermal analysis of modified Z-shaped air-cooled battery thermal management system for electric vehicles,” *Journal of Energy Storage*, 58. Available at: https://doi.org/10.1016/j.est.2022.106356.

Sheng, L. *et al.* (2019) “An improved calorimetric method for characterizations of the specific heat and the heat generation rate in a prismatic lithium ion battery cell,” *Energy Conversion and Management*, 180, pp. 724–732. Available at: https://doi.org/10.1016/j.enconman.2018.11.030.

Sheng, L. *et al.* (2021) “Quasi steady state method to measure thermophysical parameters of cylindrical lithium ion batteries,” *Journal of Power Sources*, 485. Available at: https://doi.org/10.1016/j.jpowsour.2020.229342.

Sheng, L., Su, L. and Zhang, H. (2019) “Experimental determination on thermal parameters of prismatic lithium ion battery cells,” *International Journal of Heat and Mass Transfer*, 139, pp. 231–239. Available at: https://doi.org/10.1016/j.ijheatmasstransfer.2019.04.143.

Shi, H. *et al.* (2023) “Thermal Management Techniques for Lithium-Ion Batteries Based on Phase Change Materials: A Systematic Review and Prospective Recommendations,” *Energies*. MDPI. Available at: https://doi.org/10.3390/en16020876.

Singh, R. and Nguyen, T. (2022) “Loop Heat Pipes for Thermal Management of Electric Vehicles,” *Journal of Thermal Science and*

Engineering Applications, 14(6). Available at: https://doi.org/10.1115/1.4052348.
Smith, J. *et al.* (2018) "Battery thermal management system for electric vehicle using heat pipes," *International Journal of Thermal Sciences*, 134, pp. 517–529. Available at: https://doi.org/10.1016/j.ijthermalsci.2018.08.022.
Soldan Cattani, N. *et al.* (2024) "Comparative Cost Modeling of Battery Cell Formats and Chemistries on a Large Production Scale," *Batteries*, 10(7). Available at: https://doi.org/10.3390/batteries10070252.
Song, C. *et al.* (2024) "Innovative coupled cooling strategy for enhanced battery thermal management: Synergistic optimization of jet impingement and immersion cooling," *International Journal of Heat and Mass Transfer*, 232, p. 125963. Available at: https://doi.org/https://doi.org/10.1016/j.ijheatmasstransfer.2024.125963.
Song, P. *et al.* (2024) "Cooling performance and optimization of a thermal management system based on CO2 heat pump for electric vehicles," *Energy Conversion and Management*, 306. Available at: https://doi.org/10.1016/j.enconman.2024.118299.
Spitthoff, L. *et al.* (2023) "On the Relations between Lithium-Ion Battery Reaction Entropy, Surface Temperatures and Degradation," *Batteries*, 9(5). Available at: https://doi.org/10.3390/batteries9050249.
Srinivasan, R. *et al.* (2020) "Review—Thermal Safety Management in Li-Ion Batteries: Current Issues and Perspectives," *Journal of The Electrochemical Society*, 167(14), p. 140516. Available at: https://doi.org/10.1149/1945-7111/abc0a5.
Streuling, C. *et al.* (2021) "Techno-economic assessment of battery electric trains and recharging infrastructure alternatives integrating adjacent renewable energy sources," *Sustainability (Switzerland)*, 13(15). Available at: https://doi.org/10.3390/su13158234.
Sun, B. *et al.* (2023) "Review of Low-Temperature Performance, Modeling and Heating for Lithium-Ion Batteries," *Energies*. Multidisciplinary Digital Publishing Institute (MDPI). Available at: https://doi.org/10.3390/en16207142.
Sun, D. *et al.* (2023) "An investigation on the role of electric vehicles in alleviating environmental pollution: evidence from five leading economies," *Environmental Science and Pollution Research*, 30(7), pp. 18244–18259. Available at: https://doi.org/10.1007/s11356-022-23386-x.
Sun, P. *et al.* (2020) "A Review of Battery Fires in Electric Vehicles," *Fire Technology*. Springer, pp. 1361–1410. Available at: https://doi.org/10.1007/s10694-019-00944-3.
Sundin, D.W. and Sponholtz, S. (2020) "Thermal management of Li-ion batteries with single-phase liquid immersion cooling," *IEEE Open Journal of Vehicular Technology*, 1, pp. 82–92. Available at: https://doi.org/10.1109/OJVT.2020.2972541.

Szumska, E.M. (2025) “Regenerative Braking Systems in Electric Vehicles: A Comprehensive Review of Design, Control Strategies, and Efficiency Challenges,” *Energies*. Multidisciplinary Digital Publishing Institute (MDPI). Available at: https://doi.org/10.3390/en18102422.

Tang, B., Xu, Y. and Wang, M. (2022) “Life Cycle Assessment of Battery Electric and Internal Combustion Engine Vehicles Considering the Impact of Electricity Generation Mix: A Case Study in China,” *Atmosphere*, 13(2). Available at: https://doi.org/10.3390/atmos13020252.

Tao, Z. *et al.* (2024) “Rapid warm-up strategy for lithium-ion batteries based on temperature uniformity model of sandwich self-heating structure in multiple scenarios,” *Journal of Power Sources*, 598, p. 234139. Available at: https://doi.org/https://doi.org/10.1016/j.jpowsour.2024.234139.

TeamSpeed (2020) *McLaren Speedtail Has Highest Battery Power Among Road Cara*. Available at: https://teamspeed.com/articles/mclaren-speedtail-has-highest-battery-power-among-road-cara/ (Accessed: June 27, 2023).

Torregrosa, A.J. *et al.* (2024) “A semi-empirical model of the calendar ageing of lithium-ion batteries aimed at automotive and deep-space applications,” *Journal of Energy Storage*, 80, p. 110388. Available at: https://doi.org/https://doi.org/10.1016/j.est.2023.110388.

Toshiba (2026a) *Rechargeable Lithium-ion Battery SCiB*. Available at: https://www.global.toshiba/ww/products-solutions/battery/scib/product-next/product/cell.html (Accessed: November 7, 2025).

Toshiba (2026b) *SCiB Type3 Battery Module*. Available at: https://www.global.toshiba/ww/products-solutions/battery/scib/product-next/product/module/2p12s.html (Accessed: November 7, 2025).

Trinuruk, P. *et al.* (2023) “Experimental and Numerical Studies on the Effect of Lithium-Ion Batteries’ Shape and Chemistry on Heat Generation,” *Energies*, 16(1). Available at: https://doi.org/10.3390/en16010264.

Verma, A. and Rakshit, D. (2022) “Performance analysis of PCM-fin combination for heat abatement of Li-ion battery pack in electric vehicles at high ambient temperature,” *Thermal Science and Engineering Progress*, 32. Available at: https://doi.org/10.1016/j.tsep.2022.101314.

Viswanathan, V. V. *et al.* (2010) “Effect of entropy change of lithium intercalation in cathodes and anodes on Li-ion battery thermal management,” *Journal of Power Sources*, 195(11), pp. 3720–3729. Available at: https://doi.org/10.1016/j.jpowsour.2009.11.103.

Vu, H. and Shin, D. (2020) “Scheduled pre-heating of li-ion battery packs for balanced temperature and state-of-charge distribution,” *Energies*, 13(9). Available at: https://doi.org/10.3390/en13092212.

Wang, B. and Yan, M. (2025) “The heating effect analysis of electromagnetic induction heating system based on the multi objective optimization strategy,” *Journal of Energy Storage*, 105, p. 114705. Available at: https://doi.org/https://doi.org/10.1016/j.est.2024.114705.

Wang, C. *et al.* (2025) “Application of high frequency square wave pulsed current on lithium-ion batteries at subzero temperature,” *Journal of Power Sources*, 633, p. 236413. Available at: https://doi.org/https://doi.org/10.1016/j.jpowsour.2025.236413.
Wang, C.-Y. *et al.* (2016) “A Fast Rechargeable Lithium-Ion Battery at Subfreezing Temperatures,” *Journal of The Electrochemical Society*, 163(9), pp. A1944–A1950. Available at: https://doi.org/10.1149/2.0681609jes.
Wang, C.Y. *et al.* (2016) “Lithium-ion battery structure that self-heats at low temperatures,” *Nature*, 529(7587), pp. 515–518. Available at: https://doi.org/10.1038/nature16502.
Wang, Y. *et al.* (2025) “Low temperature heating methods for lithium-ion batteries: A state-of-art review based on knowledge graph,” *Renewable and Sustainable Energy Reviews*, 213, p. 115389. Available at: https://doi.org/https://doi.org/10.1016/j.rser.2025.115389.
Wang, Z.R., Huang, L.P. and He, F. (2022) “Design and analysis of electric vehicle thermal management system based on refrigerant-direct cooling and heating batteries,” *Journal of Energy Storage*, 51, p. 104318. Available at: https://doi.org/https://doi.org/10.1016/j.est.2022.104318.
Wei, L. *et al.* (2020) “A comprehensive study on thermal conductivity of the lithium-ion battery,” *International Journal of Energy Research*, 44(12), pp. 9466–9478. Available at: https://doi.org/10.1002/er.5016.
Wen, T. *et al.* (2025) “Advances and Challenges in the Battery Thermal Management Systems of Electric Vehicles,” *Materials*. Multidisciplinary Digital Publishing Institute (MDPI). Available at: https://doi.org/10.3390/ma18204718.
Weng, J. *et al.* (2022) “Safety issue on PCM-based battery thermal management: Material thermal stability and system hazard mitigation,” *Energy Storage Materials*. Elsevier B.V., pp. 580–612. Available at: https://doi.org/10.1016/j.ensm.2022.09.007.
Weragoda, D.M. *et al.* (2023) “A comprehensive review on heat pipe based battery thermal management systems,” *Applied Thermal Engineering*. Elsevier Ltd. Available at: https://doi.org/10.1016/j.applthermaleng.2023.120070.
Wieser, S. *et al.* (2025) “Modeling and simulation of thermal management in battery electric rail vehicles for the sizing of thermal storage systems,” *Energy Conversion and Management*, 346, p. 120489. Available at: https://doi.org/https://doi.org/10.1016/j.enconman.2025.120489.
Wray, A. and Ebrahimi, K. (2022) “Octovalve Thermal Management Control for Electric Vehicle,” *Energies*, 15(17). Available at: https://doi.org/10.3390/en15176118.
Wu, H. *et al.* (2021) “An investigation on electrical and thermal characteristics of cylindrical lithium-ion batteries at low temperatures,” *Energy*, 225. Available at: https://doi.org/10.1016/j.energy.2021.120223.

Wu, H. *et al.* (2024) “Investigations of Li-Ion Battery Thermal Management Systems Based on Heat Pipes: A Review,” *ACS Omega*. American Chemical Society, pp. 97–116. Available at: https://doi.org/10.1021/acsomega.3c08056.

Wu, J., Zhou, G. and Wang, M. (2020) “A comprehensive assessment of refrigerants for cabin heating and cooling on electric vehicles,” *Applied Thermal Engineering*, 174. Available at: https://doi.org/10.1016/j.applthermaleng.2020.115258.

Wu, P. and Little, W.A. (1984) “Measurement of the heat transfer characteristics of gas flow in fine channel heat exchangers used for microminiature refrigerators,” *Cryogenics*, 24(8), pp. 415–420. Available at: https://doi.org/https://doi.org/10.1016/0011-2275(84)90015-8.

Wu, S. *et al.* (2020a) “The state of the art on preheating lithium-ion batteries in cold weather,” *Journal of Energy Storage*. Elsevier Ltd. Available at: https://doi.org/10.1016/j.est.2019.101059.

Wu, S. *et al.* (2020b) “The state of the art on preheating lithium-ion batteries in cold weather,” *Journal of Energy Storage*. Elsevier Ltd. Available at: https://doi.org/10.1016/j.est.2019.101059.

Wu, S.C. *et al.* (2015) “Study of PTFE wick structure applied to loop heat pipe,” *Applied Thermal Engineering*, 81, pp. 51–57. Available at: https://doi.org/10.1016/j.applthermaleng.2015.01.048.

Xiang, X., Liu, W. and Fan, A. (2022) “Comparison between the cooling performances of micro-jet impingement systems using liquid metal and water as coolants for high power electronics,” *International Journal of Thermal Sciences*, 173, p. 107375. Available at: https://doi.org/https://doi.org/10.1016/j.ijthermalsci.2021.107375.

Xu, L. *et al.* (2024) “A Review of Thermal Management and Heat Transfer of Lithium-Ion Batteries,” *Energies*. Multidisciplinary Digital Publishing Institute (MDPI). Available at: https://doi.org/10.3390/en17163873.

Xu, N. *et al.* (2024) “Decoupling control of an integrated direct cooling thermal management system for electric vehicles,” *International Journal of Refrigeration*, 160, pp. 165–174. Available at: https://doi.org/10.1016/j.ijrefrig.2024.01.010.

Xu, X. *et al.* (2023) “Low cost energy-efficient preheating of battery module integrated with air cooling based on a heat spreader plate,” *Applied Thermal Engineering*, 232. Available at: https://doi.org/10.1016/j.applthermaleng.2023.121024.

Xu, Z. *et al.* (2022) “Cooling performance of battery pack as affected by inlet position and inlet air velocity in electric vehicle,” *Case Studies in Thermal Engineering*, 39. Available at: https://doi.org/10.1016/j.csite.2022.102382.

Yang, H. *et al.* (2023) “A compact and lightweight hybrid liquid cooling system coupling with Z-type cold plates and PCM composite for battery thermal management," *Energy*, 263. Available at: https://doi.org/10.1016/j.energy.2022.126026.

Yang, S. *et al.* (2019) "A review of lithium-ion battery thermal management system strategies and the evaluate criteria," *International Journal of Electrochemical Science*. Electrochemical Science Group, pp. 6077–6107. Available at: https://doi.org/10.20964/2019.07.06.

Yang, T., King, W.P. and Miljkovic, N. (2021) "Phase change material-based thermal energy storage," *Cell Reports Physical Science*, 2(8), p. 100540. Available at: https://doi.org/https://doi.org/10.1016/j.xcrp.2021.100540.

Yang, X. *et al.* (2020) "Effect of ambient dissipation condition on thermal behavior of a lithium-ion battery using a 3D multi-partition model," *Applied Thermal Engineering*, 178. Available at: https://doi.org/10.1016/j.applthermaleng.2020.115634.

Yang, X.-G., Liu, T. and Wang, C.-Y. (2017) "Innovative heating of large-size automotive Li-ion cells," *Journal of Power Sources*, 342, pp. 598–604. Available at: https://doi.org/https://doi.org/10.1016/j.jpowsour.2016.12.102.

Yang, X.-G., Zhang, G. and Wang, C.-Y. (2016) "Computational design and refinement of self-heating lithium ion batteries," *Journal of Power Sources*, 328, pp. 203–211. Available at: https://doi.org/https://doi.org/10.1016/j.jpowsour.2016.08.028.

Yang, Z., Yan, Y. and Pak, U. (2023a) "Thermal reliability assessment and sensitivity analysis of 18,650 cylindrical lithium-ion battery," *Journal of Energy Storage*, 59. Available at: https://doi.org/10.1016/j.est.2022.106504.

Yang, Z., Yan, Y. and Pak, U. (2023b) "Thermal reliability assessment and sensitivity analysis of 18,650 cylindrical lithium-ion battery," *Journal of Energy Storage*, 59. Available at: https://doi.org/10.1016/j.est.2022.106504.

Yesiloz, G. and Aydin, O. (2013) "Laminar natural convection in right-angled triangular enclosures heated and cooled on adjacent walls," *International Journal of Heat and Mass Transfer*, 60(1), pp. 365–374. Available at: https://doi.org/10.1016/j.ijheatmasstransfer.2013.01.009.

Yi, Z. *et al.* (2023) "Wide range temperature thermal performance of power battery module with double-sided thermoelectric device system with high energy efficiency," *Applied Thermal Engineering*, 227. Available at: https://doi.org/10.1016/j.applthermaleng.2023.120375.

Yin, L. *et al.* (2021) "Analyzing and mitigating battery ageing by self-heating through a coupled thermal-electrochemical model of cylindrical Li-ion cells," *Journal of Energy Storage*, 39, p. 102648. Available at: https://doi.org/https://doi.org/10.1016/j.est.2021.102648.

Youssef, R. *et al.* (2022) "Novel design optimization for passive cooling PCM assisted battery thermal management system in electric vehicles," *Case Studies in Thermal Engineering*, 32. Available at: https://doi.org/10.1016/j.csite.2022.101896.

Yu, H. *et al.* (2023) “Thermal parameters of cylindrical power batteries: Quasi-steady state heat guarding measurement and thermal management strategies,” *Applied Thermal Engineering*, 231. Available at: https://doi.org/10.1016/j.applthermaleng.2023.120959.

Zamanifard, A. *et al.* (2023) “A novel 3-D pulsating heat pipe module for high heat-flux applications,” *Applied Thermal Engineering*, 228. Available at: https://doi.org/10.1016/j.applthermaleng.2023.120549.

Zatta, N. *et al.* (2025) “Thermal study on a LTO cell module: Experiment, 3D numerical analysis and model order reduction,” *International Journal of Heat and Mass Transfer*, 237. Available at: https://doi.org/10.1016/j.ijheatmasstransfer.2024.126407.

Zhang, C., Jin, X. and Li, J. (2017) “PTC self-heating experiments and thermal modeling of lithium-ion battery pack in electric vehicles,” *Energies*, 10(4). Available at: https://doi.org/10.3390/en10040572.

Zhang, F. *et al.* (2021) “Optimization design for improving thermal performance of T-type air-cooled lithium-ion battery pack,” *Journal of Energy Storage*, 44. Available at: https://doi.org/10.1016/j.est.2021.103464.

Zhang, H. *et al.* (2025) “The Heat Exchange Coefficient of the Cooling Tube Under the Influence of the Tube Material and Cooling Water Parameters,” *Buildings*, 15(12). Available at: https://doi.org/10.3390/buildings15122014.

Zhang, L. *et al.* (2020) “Battery heating for lithium-ion batteries based on multi-stage alternative currents,” *Journal of Energy Storage*, 32. Available at: https://doi.org/10.1016/j.est.2020.101885.

Zhang, Q. *et al.* (2023a) “Research on the Reversible and Irreversible Heat Generation of LiNi1−x−yCoxMnyO2-Based Lithium-Ion Batteries,” *Fire Technology*, 59(3), pp. 1029–1049. Available at: https://doi.org/10.1007/s10694-022-01220-7.

Zhang, Q. *et al.* (2023b) “Research on the Reversible and Irreversible Heat Generation of LiNi1−x−yCoxMnyO2-Based Lithium-Ion Batteries,” *Fire Technology*, 59(3), pp. 1029–1049. Available at: https://doi.org/10.1007/s10694-022-01220-7.

Zhang, R. *et al.* (2018) “Study on the characteristics of a high capacity nickel manganese cobalt oxide (NMC) lithium-ion battery-an experimental investigation,” *Energies*, 11(9). Available at: https://doi.org/10.3390/en11092275.

Zhang, X. *et al.* (2022) “A review on thermal management of lithium-ion batteries for electric vehicles,” *Energy*, 238, p. 121652. Available at: https://doi.org/https://doi.org/10.1016/j.energy.2021.121652.

Zhang, Y. *et al.* (2022) “Performance comparison between straight channel cold plate and inclined channel cold plate for thermal management of a prismatic LiFePO4 battery,” *Energy*, 248. Available at: https://doi.org/10.1016/j.energy.2022.123637.

Zhang, Z., Liu, S. and Tian, L. (2011) “Thermodynamic analysis of air cycle refrigeration system for Chinese train air conditioning,” *Systems Engineering*

Procedia, 1, pp. 16–22. Available at: https://doi.org/10.1016/j.sepro.2011.08.004.

Zhang, Z. and Wei, K. (2020) “Experimental and numerical study of a passive thermal management system using flat heat pipes for lithium-ion batteries,” *Applied Thermal Engineering*, 166. Available at: https://doi.org/10.1016/j.applthermaleng.2019.114660.

Zhao, D. and Tan, G. (2014) “A review of thermoelectric cooling: Materials, modeling and applications,” *Applied Thermal Engineering*, pp. 15–24. Available at: https://doi.org/10.1016/j.applthermaleng.2014.01.074.

Zhao, G. *et al.* (2021) “A review of air-cooling battery thermal management systems for electric and hybrid electric vehicles,” *Journal of Power Sources*. Elsevier B.V. Available at: https://doi.org/10.1016/j.jpowsour.2021.230001.

Zhao, G. *et al.* (2023) “An up-to-date review on the design improvement and optimization of the liquid-cooling battery thermal management system for electric vehicles,” *Applied Thermal Engineering*. Elsevier Ltd. Available at: https://doi.org/10.1016/j.applthermaleng.2022.119626.

Zhao, Y., Wei, M. and Dan, D. (2024) “Modeling, Design, and Optimization of Loop Heat Pipes,” *Energies*. Multidisciplinary Digital Publishing Institute (MDPI). Available at: https://doi.org/10.3390/en17163971.

Zhou, T. *et al.* (2025) “A novel water-based direct contact cooling system for thermal management of lithium-ion batteries,” *Journal of Energy Storage*, 107. Available at: https://doi.org/10.1016/j.est.2024.114973.

Zhou, Y. *et al.* (2022) “Discussion on International Standards Related to Testing and Evaluation of Lithium Battery Energy Storage,” *Distributed Generation and Alternative Energy Journal*, 37(3), pp. 435–448. Available at: https://doi.org/10.13052/dgaej2156-3306.3732.

Zhou, Y. *et al.* (2024) “Optimized Design and Operation Control of Refrigerant Direct Cooling Thermal Management System for Power Battery,” *Energy Technology*, 12(8). Available at: https://doi.org/10.1002/ente.202400251.

Zhu, C. *et al.* (2020) “Core Temperature Estimation for Self-Heating Automotive Lithium-Ion Batteries in Cold Climates,” *IEEE Transactions on Industrial Informatics*, 16(5), pp. 3366–3375. Available at: https://doi.org/10.1109/TII.2019.2960833.

Zhu, J. *et al.* (2016) “An alternating current heating method for lithium-ion batteries from subzero temperatures,” *International Journal of Energy Research*, 40(13), pp. 1869–1883. Available at: https://doi.org/10.1002/er.3576.

Zhu, X. *et al.* (2025) “Flame-retardant polymer electrolytes enhancing the safety of lithium batteries,” *Journal of Energy Storage*. Elsevier Ltd. Available at: https://doi.org/10.1016/j.est.2024.115080.

Zhuang, S. *et al.* (2022) “Research on Estimation of State of Charge of Li-ion Battery based on Cubature Kalman Filter,” *Journal of The*

Electrochemical Society, 169(10), p. 100521. Available at: https://doi.org/10.1149/1945-7111/ac95cf.

Zolot, M.D. *et al.* (2001) “Thermal Evaluation of the Honda Insight Battery Pack.” U.S. Department of Energy Laboratory.

Zuo, W. *et al.* (2022) “Performance comparison between single S-channel and double S-channel cold plate for thermal management of a prismatic LiFePO4 battery,” *Renewable Energy*, 192, pp. 46–57. Available at: https://doi.org/10.1016/j.renene.2022.04.116.

Zuo, W. *et al.* (2023) “Effects of flow direction in mini U-channel cold plates on thermal performance of a prismatic LiMn2O4 battery,” *Journal of Thermal Analysis and Calorimetry*, 148(9), pp. 3689–3699. Available at: https://doi.org/10.1007/s10973-022-11935-y.

List of Symbols

Acronyms			
ABS	Acrylonitrile Butadiene Styrene	Li-ion	Lithium-ion
AM	Additive Manufacturing	LMO	Lithium Manganese Oxide
ASM	Algebraic Stress Model	LTO	Lithium Titanate Oxide
BEMU	Battery Electric Multiple Unit	NCA	Nickel Cobalt Aluminium Oxide
CAD	Computer-Aided Design	NMC	Nickel Manganese Cobalt Oxide
CFD	Computational Fluid-Dynamics	PCM	Phase Change Material
ECM	Equivalent Circuit Model	RANS	Raynolds-Averaged Navier-Stokes
EV	Electric Vehicle	RMSE	Root Mean Square Error
FEM	Finite Element Method	RTD	Resistance Temperature Detector
GHG	Greenhouse Gas	SCP	Serpentine Cold Plate
HMCP	Horizontal Minichannels Cold Plate	SHLB	Self-Heating Lithium-ion Battery
HPPC	Hybrid Power Pulse Characterisation	SOC	State of Charge
ICE	Internal Combustion Engine	SSE	Error Sum of Squares
LCA	Life Cycle Assessment	SST	Total Corrected Sum of Squares
LCO	Lithium Cobalt Oxide	TMS	Thermal Management System
LFP	Lithium Iron Phosphate	VCP	Vertical Cold Plate

Symbols			
A	Heat exchange surface [m^2]	N	Number of channels
A_{sec}	Channel cross-section [m^2]	N_d	N. of horizontal spaces between minichannels
a	Rectangular cross-section width [m]	Nu	Nusselt number
Bi	Biot number	n	Number of free electrons
b	Rectangular cross-section height [m]	P	Minichannel path length [m]
C_1	First loop capacitance	Pr	Prandtl number
C_2	Second loop capacitance	p	Pressure [Pa]
C_{rate}	C-rate	$\dot{Q}$	Heat rate [W]
c_p	Specific heat [J·kg^{-1}K^{-1}]	R	Radius of the LTO cell [m]
D	Diameter of the LTO cell [m]	R_0	Ohmic resistance of the cell
D_h	Hydraulic diameter [m]	R_1	First loop resistance
d	Horizontal spacing between minichannels [m]	R_2	Second loop resistance
E	Energy [J]	R^2	Coefficient of correlation
E_{OC}	Open circuit voltage [V]	Ra	Rayleigh number
$err_{\%}$	Percentage error	Re	Reynolds number
F	Faraday constant	r	Rectangular cross-section aspect ratio
f	Friction factor	S	Entropy of chemical species [J·mol^{-1}·K^{-1}]
g	Gravitational acceleration [m·s^{-2}]	s	Vertical spacing between U-minichannels [m]
H	Battery pack height [m]	T	Temperature [°C]
h	Heat transfer coefficient [W·m^{-2}K^{-1}]	T_{∞}	Free-stream temperature [°C]
I	Current intensity [A]	$\bar{T}$	Average temperature [°C]
L	Battery pack length [m]	t	Thickness of the battery pack enclosure [m]
L_{LTO}	LTO cell length [m]	th	Thickness of the electrode
$\dot{L}_p$	Pumping power [W]	u	Coolant velocity [m·s^{-1}]
l	Characteristic length for Biot evaluation [m]	u_{gen}	Heat generation rate per volume unit [W·m^{-3}]
$\dot{m}$	Mass flow rate [kg·s^{-1}]	V	Voltage [V]

Greek symbols			
β	Coefficient of volume expansion [K^{-1}]	η_{con}	Concentration losses voltage drop
γ_{alu}	Aluminium electric conductivity[$S \cdot m^{-1}$]	λ	Thermal conductivity [$W \cdot m^{-1} K^{-1}$]
ε	Emissivity	μ	Dynamic viscosity [Pa·s]
η_0	Ohmic voltage drop	ν	Kinematic viscosity [$m^2 \cdot s^{-1}$]
η_1	First loop voltage drop	ρ	Density [$kg \cdot m^{-3}$]
η_2	Second loop voltage drop	σ	Stefan-Blotzmann constant [$W \cdot m^{-2} \cdot K^{-4}$]
η_{act}	Activation losses voltage drop	σ_{alu}	Electrical conductivity of aluminium
Subscripts			
air	Air	irr	Irreversible
CFD	Computational Fluid-Dynamics	max	Maximum
$cell$	Cold plate	$mini$	Minichannel
$cond$	Cell	out	Outlet
$conv$	Conductive heat transfer	r	Property along radial direction
dis	Convective heat transfer	rad	Radiative heat transfer
el	Dissipated	rev	Reversible
el	Electrode	row	Single row of battery pack cells
enc	Enclosure	s	Copper serpentine
end	End of the simulation	set	Set point
exp	Experimental	sup	Superficial
$film$	Fluid film property	tot	Total
$fine$	Finest mesh	w	Water flow
gen	Internal generation	z	Property along z axis
in	Inlet	$\%$	Percentage